**Title**
Oscillatory Flame Response in Acoustically Coupled Fuel Droplet Combustion



**Author**
Sevilla Esparza, Cristhian Israel

**Publication Date**
2013

Peer reviewed|Thesis/dissertation

University of California
Los Angeles

# Oscillatory Flame Response in Acoustically Coupled Fuel Droplet Combustion

A thesis submitted in partial satisfaction
of the requirements for the degree
Master of Science in Aerospace Engineering

by

**Cristhian Israel Sevilla Esparza**

2013

Abstract of the Thesis

# Oscillatory Flame Response in Acoustically Coupled Fuel Droplet Combustion

by

**Cristhian Israel Sevilla Esparza**

Master of Science in Aerospace Engineering

University of California, Los Angeles, 2013

Professor Ann R. Karagozian, Chair

This experimental study focuses on combustion of liquid fuel droplets subject to external acoustic disturbances in the form of standing waves within an acoustic waveguide. Acoustic perturbations create a mean flame deflection dependent on the droplet location relative to the pressure node (PN) or pressure antinode (PAN) in the waveguide. This flame deflection is consistent with the sign of a theoretical acoustic acceleration acting on the burning system. Yet experimentally derived acoustic accelerations estimated from the degree of flame deflection differ quantitatively from that predicted by the acoustic radiation force theory. Phase locked OH* chemiluminescence imaging reveals a deflected flame which oscillates in position relative to the stationary droplet. Flame luminosity fluctuates with pressure throughout the forcing period, indicating the flame heat release rate is influenced by acoustic excitation. The thermoacoustic instability fostered by the in-phase oscillation of pressure and heat release rate is quantified via the Rayleigh index. Evaluation of the Rayleigh index over a range of acoustic forcing frequencies and droplet locations exposes the frequency sensitive character of the combustion mechanism stemming from dissimilar acoustic and chemical kinetic time scales. The present experimental configuration provides a useful test bed for evaluating the response of different alternative and conventional fuels to an acoustically resonant environment in the context of the well-known Rayleigh criterion.

The thesis of Cristhian Israel Sevilla Esparza is approved.

Jeffrey D. Eldredge

Owen I. Smith

Ann R. Karagozian, Committee Chair

University of California, Los Angeles

2013

*A Martha y Domingo*

# Table of Contents

# List of Figures

# List of Tables

# Nomenclature

**Symbols**

| | |
|---|---|
| $c$ | local speed of sound |
| $d$ | droplet diameter |
| $f_a$ | acoustic forcing frequency |
| $F_a$ | acoustic radiation force |
| $F_b$ | buoyancy force |
| $g_a$ | acoustic acceleration |
| $g_o$ | gravitational acceleration |
| $G$ | Rayleigh index |
| $I'$ | integrated image intensity perturbation |
| $K$ | burning rate constant |
| $l$ | axial acoustic cavity span |
| $L$ | effective acoustic length between loudspeakers |
| $L'$ | waveguide extension length |
| $p'$ | pressure perturbation |
| $q'$ | heat release rate perturbation |
| $Q_v$ | volumetric flowrate |
| $r_f$ | radial flame front distance from droplet center |
| $r_s$ | droplet radius |
| $t$ | time |
| $T_a$ | acoustic time period |
| $u'$ | velocity perturbation |
| $V$ | voltage |
| $x$ | displacement of droplet relative to PN location; axial waveguide location |
| $z_a$ | acoustic impedance |

**Greek and Script Characters**

| | |
|---|---|
| $\alpha$ | density correction factor |
| $\delta_f$ | flame standoff distance |
| $\theta$ | polar coordinate angle |
| $\Delta t_{gate}$ | camera gate activation time interval |
| $\Delta x$ | speaker assembly offset |
| $\kappa$ | voltage gain |
| $\lambda$ | acoustic wavelength |
| $\rho$ | density |
| $\phi$ | relative phase |
| $\phi_f$ | flame deflection angle |
| $\mathcal{I}$ | acoustic intensity |
| $\mathcal{V}$ | volume |

**Subscripts and Abbreviations**

| | |
|---|---|
| $a$ | acoustic |
| $eqvs$ | equivalent volume of a sphere |
| $exp$ | experimental |
| $f$ | flame |
| $p$ | combustion products |
| $PN$ | pressure node |
| $PAN$ | pressure antinode |
| $PT$ | pressure transducer |
| $th$ | theoretical |
| $thr$ | threshold intensity |
| $VN$ | velocity node |
| $VAN$ | velocity antinode |
| $WG$ | waveguide |

# Acknowledgments

The fulfillment of this research endeavor was made possible through the support, assistance, and patience of those I would like to recognize in these acknowledgments. Foremost I thank God for instilling fortitude and optimism in me and my efforts during the bleaker periods of the past years. I also thank Him for paving my path with goodness and hope personified in all those that have helped me become the man I am today.

My experience at UCLA was enhanced substantially through the influence of many, especially my advisor, Professor Ann Karagozian. Her invaluable insights and constant encouragement, both scholarly and financially, were instrumental in my formation as a student and researcher. For this and all of the exceptional contributions she provides to the university, her collaborators, and my peers, I thank Professor Karagozian sincerely. The counsel of Professor Jeff Eldredge in and out of the lecture hall added an illuminating dimension to my collegiate tenure which I owe much gratitude for as well. The practicality and candor of advice from Professor Owen Smith was most welcome in the evolution of our experiments. I'd also like to thank the entire UCLA MAE staff, with honorable mention to Miguel Lozano, Angie Castillo, and Lili Bulhoes, for streamlining many potentially stressful circumstances and attenuating the accumulation of my gray hair during the last six years.

It was a privilege to be part of the Energy and Propulsion Research Laboratory and to collaborate with the bright individuals there during the past three years. First I would like to recognize the introductory efforts exerted by Jeff Wegener, who prepared me for graduate-level experimental research and its peripherals during his time at UCLA. I would also like to convey my appreciation for the peers involved in my development and that of the droplet experiment, including Sophonias, Cory, Dan, Levon, Lord, Hai, Jennifer, Aaron, Kelvin, Ayaboe, Brett, Will, and Takeshi. For the assistance with laboratory tasks, for the insightful observations discussed, and for the intellectual (and not so intellectual!) conversations over lunch, I thank you all.

Academically I owe my achievements to many of the teachers that have impacted my

trajectory in the classroom and in life. I reserve great admiration for Terry Mendoza and Deloris Stokes, two gifted educators without whom I could not envision my growth as a student. Furthermore, I am indebted to a host of instructors for instilling within me the fundamentals of curiosity and diligence, including Pedro Reyes, Ernest Ruiz, Corinna Fiedler, Michael Denman, David Delaby, and Diana Maruna. While not teachers by profession, both Esperanza Lopez and Lourdes Castro Ramirez have served as my personal educators, consistently present as role models and catalysts for my progress.

The perpetual support of my family and friends was indispensable prior to and during my university career. The sacrifices of my mother, Martha, and my father, Domingo, were the stimuli and foundations for my accomplishments, and I wish to dedicate this thesis to them. My siblings, Cindy and Cristopher, contributed greatly to my day-to-day sanity, particularly while sharing late night laughs over nearly-memorized Seinfeld reruns. I would also like to thank Lupita Torres and Martin Sevilla, siblings of my parents that have always treated me as one of their own, for their financial and motivational sustenance. The memories and adventures I have shared with all of my friends (you know who you are!) truly enriched my life, and I feel blessed to have encountered such remarkable people.

Finally, words cannot express my appreciation for the support and encouragement of my companion and best friend, Magali Barba. Whether it was helping me wrestle obnoxious MATLAB™ minutiae into submission or joining me on a phone call during the moonlit commutes back home, the value of her presence through thick and thin is inestimable. Couldn't have done it without you, Chula!

# CHAPTER 1

# Introduction

The present experimental studies expand upon research analyzing the effects of coherent acoustic disturbances on condensed phase combustion processes. These experiments gain motivation from thermoacoustic phenomena pervasive in liquid rocket engines (LREs), air-breathing engines and turbines, and other devices relevant to power generation. Coupling of large acoustic fluctuations with multiphase combustion in the case of LREs, for instance, can lead to violent vibrations of the combustion chamber and catastrophic failure, features that are innately related to design architecture. While unique configurations for these diverse systems play a key role in quantifying acoustic and combustion disturbances, the absence of a fundamental understanding of the interaction between both has fostered innovative combustion instability research. Nevertheless, the focus of such investigations is largely centered on premixed combustion regimes. The experiments conducted at the UCLA Energy and Propulsion Research Laboratory contribute to the quantification of thermoacoustic instability in an acoustically excited non-premixed flame in the form of a burning liquid droplet. The response of salient flame characteristics to acoustic forcing is also assessed and compared to baseline values. The droplet combustion system analyzed employs a host of alternative fuels that have assumed increased roles in commercial and military applications.

## 1.1 Combustion Instabilities

Combustion instabilities are characterized by self-sustaining, spontaneously excited, large amplitude oscillations of one or more natural acoustic modes established within a combustor. Such instabilities develop when properties conducive to oscillation dampening, such as

viscous dissipation and heat transfer, are overcome by those fostering oscillation, especially the coupling of heat release and pressure perturbations [1, 2]. Continuous combustion devices predominant in contemporary propulsion and power generation systems are susceptible to these instabilities because of associated mechanical vibrations affecting combustion chamber peripherals, enhanced heat transfer rates to combustor walls, and potential for partial or total flame blowoff, among other factors [3, 4].

The occurrence of thermoacoustic combustion instabilities within LREs and gas turbine engines has a long history of study. Symptoms of combustion oscillations in liquid rockets were first documented during the late 1930s in the Soviet Union [5]. Systematic efforts to characterize instabilities in the United States were motivated by operational requisites of the Apollo program in the 1960s [6]. Though such research slowed through the following two decades, dedicated efforts to mitigate instabilities resurfaced in the 1980s after the catastrophic failure of an Ariane spacecraft due to a crack in the combustion chamber of its Viking rocket engine attributed to combustion oscillations. Presently there is well documented evidence of varied phenomena impacting LREs, such as the POGO instability generated through closed loop coupling of combustor pressure and incident fuel flowrate [7]. Ongoing investigations focus on attenuation of combustion instabilities through active system control and fuel injection design [5].

Instability in lean premixed (LP) gas turbines has also drawn significant attention since the amendment of stringent environmental regulations starting in the 1970s. Policy mandated a shift in the operational regimes of engines in aviation and industry with the ultimate goal of reducing nitrogen oxide and sulfur emissions while fulfilling performance requirements for increased efficiency [8]. This prompted a transition to LP devices implementing fuel lean combustion. While reducing maximum combustion temperature and fuel consumption, and thus undesirable emission output, early LP systems were especially vulnerable to small temporal oscillations in fuel-air ratio near lean blowout limits leading to global combustion instabilities [9, 10]. Current experimental and numerical analyses concentrate on fuel-oxidizer mixing strategies and combustor actuation to prevent the onset of instability,

whose symptoms include enhanced transient heat release, fuel injector deterioration, and intolerable structural vibration [11].

The previous two decades procured investigations extrapolating into nonpremixed combustion instabilities that correspond to elements in their premixed counterparts. Sohn *et al.* [12] studied the acoustic response of high pressure hydrogen-oxygen flame kinetics in a counterflow arrangement to simulate near-extinction features prevalent in rocket engines sensitive to combustion oscillations. Yu *et al.* [13] analyzed ethylene-air flames generated via concentric, acoustically forced coaxial flows whose vortical interactions held crucial implications for instability suppression in combustor mixing systems. Ultimately the extension of thermoacoustic instability research to canonical diffusion flame structures is attractive due to relative simplicity of experimental apparatus and relevance to fundamental phenomena. Furthermore, such studies allow for an efficient and inexpensive assessment of combustion properties in alternative fuels prolifically utilized in various practical settings.

## 1.2 Alternative Fuels

Contemporary development and implementation of alternative fuels are consequences of global demand of finite fossil fuel reserves and austere emission policies enacted during the latter half of the 20th century. Hydrocarbon fuels are feasible short-term petroleum fuel surrogates within present infrastructure. Biofuels and synthetic hydrocarbons, whose production and exploration have increased within the United States in the last decade, are especially attractive in transportation and aviation, respectively [14, 15].

Short-chain hydrocarbon fuels, namely alcohols, have become staple complements to gasoline and diesel fuel in modern internal combustion (IC) engines. Macroscale production of ethanol as a fuel was spurred through federal incentives outlined in the Energy Policy Act of 1978 [16]. Increased environmental consciousness contributed to amendment of the Clean Air Act in the 1970s and 1990s that fostered alcohol fuel implementation in IC engines. Fuels like methanol and ethanol exhibit higher octane ratings and thermal efficiencies with

lower combustion temperatures in comparison to gasoline [17]. These attributes contribute to diminished production of thermal nitrous oxides. Nonetheless, reduced energy densities per unit volume, along with extensive modifications necessary for alcohol-exclusive IC engine operation, limit the use of pure methanol and ethanol fuels conventionally [18]. Gasoline-alcohol blends, on the other hand, improve emissions and demand little, if any, engine refitting.

Impractical energy densities and volumetric heats of combustion in biofuels render them typically ill-suited for aircraft [19], although efforts for tailoring such fuels for aviation applications constitute an active area of research [14]. Military and academic institutions are exploring the viability of fuels derived through Fischer Tropsch (FT) synthesis, a family of gas-to-liquid chemical processes that use hydrogen and carbon monoxide to produce liquid hydrocarbons [20]. FT fuels may also be derived from coal, natural gas, biofuels, and a host of other sources. Air Force military aircraft, including the B-52H Stratofortress and C-17 Globemaster III, have been certified to operate using a 50%-50% volumetric blend of standard JP-8 fuel and FT synthetic fuel developed by the Syntroleum Corporation [21].

Assertion of combustion attributes inherent to the alternative fuels discussed here is paramount within engine and turbine systems. Fuel performance is of particular relevance in acoustically resonant conditions where detrimental combustion response is poorly understood. Pressure waves established within intake manifolds in IC engines, for example, can yield unacceptable cycle-to-cycle variations in fuel-air ratio, pressure, and temperature [22]. Interacting time scales associated with diffusion, convection, and acoustics influence combustion processes that are innately dependent on the reactive kinetics for different fuels. Hence, it is necessary to develop a fundamental concept of the coupling between acoustic disturbances and specific combustion regimes present in practical contexts.

## 1.3 Droplet Combustion

Flammable liquid droplets administered via spray fuel injection systems are typical constituents of condensed phase combustion present within IC engines and turbines [23, 24]. These systems introduce fuel either as a dilute spray of minuscule droplets or as a liquid stream that disperses into individual fuel ligaments and spherules. While the interaction between ignited droplets holds influence on the global evolution of combustion reactions, individual droplet burning remains a key aspect in the operation of these devices. The fundamental character of a single isolated burning fuel droplet represents a nonpremixed reactive process whose behavior has been explored over many years. The droplet evaporates and acts as a source of fuel vapor that reacts with an oxidizer, typically air, to form a flame front surrounding the droplet.

Classical studies have demonstrated that, for quasi-steady, essentially spherical burning droplets in quiescent, oxidizing surroundings, temporal variation in diameter $d$ is predicted by the $d^2$ law [25, 26]. While especially applicable to spherically symmetric burning droplets in a microgravity environment [27], the $d^2$ law is approximately valid for burning droplets in a gravitational environment, even under non-quiescent conditions, since an effective diameter of an equivalent spherical droplet may be used [28, 29]. The standard $d^2$ law is represented by

$$d^2(t) = d^2(t = 0) - Kt. \tag{1.1}$$

In Eq. (1.1), $K$ is the burning rate constant, typically expressed in units of $\mathrm{mm}^2/\mathrm{sec}$, and $t$ is time. In normal gravity conditions, a suspended burning droplet cannot maintain a spherical geometry due to gravitational and surface tension forces; the former effect is virtually eliminated, of course, in microgravity experiments. In order to determine $K$ via the $d^2$ law in gravitational environments, the effective diameter for the non-spherical droplet is often determined by equating the experimentally estimated volume of the actual droplet to the volume of an equivalent spherical droplet of diameter $d_{eqvs}$ [30].

Recent efforts strive to quantitatively relate unobtrusive optical diagnostics and bulk

flame properties like temperature and heat release in diffusion flame regimes, including burning droplets. Individual studies by Najm *et al.* [31] and Montenegro *et al.* [32] establish a correlation between reaction zone location, global heat release rate, and concentrations hydroxyl (OH) and formaldehyde ($CH_2O$) radicals present during the combustion of a hydrocarbon diffusion flames through laser-induced fluorescence (LIF) measurements. Chemiluminescence, the emission of light via radiative deexcitation caused by the decay of an electronically excited chemical species to a lower quantum state, has also been implemented in the quantification of combustion properties [33]. Microgravity experiments conducted by Marchese *et al.* [34, 35], validated numerical simulations indicating the applicability OH* chemiluminescence as a marker for flame location. Previous experiments in the UCLA Energy and Propulsion Research Laboratory by Dattarajan *et al.* [36] and Wegener [37] are the first to characterize OH* chemiluminescence for burning hydrocarbon droplets in acoustically resonant conditions.

## 1.4 Effects of Acoustics on Droplet Combustion

Recent studies have examined fuel droplets burning in an acoustically resonant environment within an acoustic waveguide. Several experimental studies have shown that there can be a moderate to significant increase in fundamental heat and mass transfer rates from burning droplets with the imposition of an external acoustical field [28, 38, 39], similar to augmentation of transport processes in other reactive environments such as gas turbine combustion chambers. The experiments of Saito *et al.* [38, 39], for example, examine the effects of acoustic waves on single evaporating and burning kerosene droplets, finding that when a standing acoustic wave is created and the fuel droplet is situated at a pressure node (PN), or velocity antinode (VAN), there can be a two to three-fold increase in evaporative or combustion rate constants. Conversely, if the droplet is located at a pressure antinode (PAN) or velocity node (VN), there is little appreciable change in the evaporation or combustion rates.

Experiments have also involved acoustical excitation of burning droplets in microgravity, where the absence of natural convection arising from gravitational forces allows a degree of isolation of the effects of acoustic excitation [40]. The microgravity experiments of Tanabe *et al.* [41–43] involving a burning *n*-decane droplet situated in the vicinity of a PN, or between the pressure node and antinode of a standing wave in a closed duct, show significant increases in the burning rate constant as the maximum velocity perturbation is increased, up to 85% higher than the unforced burning rate constant.

Earlier studies with methanol droplets in microgravity and normal gravity by this group, specifically Dattarajan *et al.* [36, 44], have focused on combustion characteristics during exposure to standing acoustic waves within a waveguide. For pressure perturbation amplitudes exceeding 135 dB, droplet burning rates are seen to increase by over 75% and 200% for droplets situated in the vicinity of PAN and PN locations, respectively. In contrast, in normal gravity and for similar pressure excitation, droplets situated near a pressure node produce only very moderate increases in burning rate about 11-15% higher than for non-acoustically excited, burning droplets. No significant change in burning rate is observed when the droplet is situated near the PAN.

In both microgravity and normal gravity experiments in Dattarajan *et al.* [36], orientation of the flame enveloping the droplet depends on the droplet's position within the waveguide. In the vicinity of a PN, the flame is oriented systematically away from the PN; for instance, when the droplet is shifted to the right of a PN, its flame appears deflected to the right. This type of bulk alteration in flame orientation with droplet position is also observed in droplet combustion experiments by Tanabe *et al.* via visualization of the sooting flame's wake [41–43]. Such flame deflections are interpreted by Tanabe *et al.* in terms of the magnitude and orientation of an acoustic radiation force $F_a$ acting on the "sphere" of hot gases nominally surrounding the burning droplet. This force is represented by

$$F_a = \alpha \left(\rho_p - \rho_o\right) \mathcal{V} \frac{\partial\left(\bar{u'^2}\right)}{\partial x} = \left(\rho_p - \rho_o\right) \mathcal{V} g_a. \tag{1.2}$$

Here, $\rho_p$ is the density of the hot, gaseous combustion products and other species within

the sphere, $\rho_o$ is the density of ambient air external to the flame, $\mathcal{V}$ is the volume of the region containing the hot gases, $x$ is the distance of the droplet measured from the location of the PN established within the waveguide. $\bar{u'^2}$ is the mean of the square of the amplitude of the local perturbation velocity, $u'$, within the waveguide at location $x$. The coefficient $\alpha$ is dependent on gas densities, and takes the form

$$\alpha \equiv \frac{3\rho_o}{2\left(2\rho_p + \rho_o\right)}. \tag{1.3}$$

The term $g_a$ in Eq. (1.2) represents an "acoustic acceleration", where $g_a \equiv \alpha \frac{\partial \bar{u'^2}}{\partial x}$. Hence the acoustic radiation force $F_a$ has the same form as a buoyancy force $F_b$ acting on a light object of density $\rho_s$ and volume $\mathcal{V}$, surrounded by a heavier fluid of density $\rho_o$ in a gravitational field with acceleration $g_o$; in other words, $F_b = \left(\rho_p - \rho_o\right)\mathcal{V} g_o$ . This leads Tanabe *et al.* [41–43] to suggest that the influence of the acoustic radiation force on droplet combustion and flame deformation is similar to that of a gravitational force.

As with the burning droplets observed in Dattarajan *et al.* [36], the burning droplets in microgravity in Tanabe *et al.* [41–43] have flames oriented away from the PN when situated on either side of the PN, with a bulk flow deflecting the flame away from the PN or toward the PAN. Tanabe *et al.* also studied premixed flames [43] as well as a single hot wire [43] in the vicinity of pressure nodes and antinodes. Asymmetries in the flame or heated flow region again appear to be qualitatively consistent with the notion of an acoustic radiation force acting on the hot gases and flame as expressed in Eq. (1.2), with increasing asymmetry arising with an increase in acoustic excitation amplitude. Yet there has been no quantitative validation of dependence of droplet position in the acoustic radiation force model, other than to correlate increases in transport properties such as the burning rate constant $K$ for a droplet with increases in the acoustic acceleration $g_a$ [41]. While Dattarajan *et al.* [36] observe the same qualitative confirmation of the acoustic radiation force theory in terms of flame orientation, there is no quantitative verification of the equation in that study, either. In fact, in contrast to the theoretical prediction in Eq. (1.2) and an image presented in Tanabe *et al.* of a more spherically shaped, unperturbed flame, when the droplet is situated precisely at a PN in Dattarajan and others' experiments, significant flame oscillation and

relative instability in the direction of deflection are observed.

Ongoing studies at the UCLA Energy and Propulsion Research Laboratory build on past droplet combustion experiments in microgravity and normal gravity conducted by Dattarajan [36, 44] in an attempt to examine the proposed acoustic radiation force theory from a quantitative perspective. Studies presented in the publications of Rodriguez [45, 46] and Teshome [47–49] explored droplet combustion response in acoustic environments inherent to both dual speaker and speaker-reflector configurations, with assessment of acoustically-resonant combustion characteristics like burning rate constant and acoustic acceleration. Wegener [37] performed OH* chemiluminescence imaging with speaker-speaker arrangements that revealed temporal combustion dynamics intimately coupled with acoustic forcing. The present experiments characterize acoustic excitation in the speaker-speaker assembly and extend the application of chemiluminescence imaging to ascertain thermoacoustic combustion instability inherent to the burning droplet system. A range of alternative fuels, including alcohols (ethanol and methanol), aviation fuel (JP-8), synthetic fuel derived from coal via the Fischer-Tropsch process, or "FT" fuel, were examined in the present investigation.

# CHAPTER 2

# Experimental Facility and Methods

The experimental apparatus utilized to complete the present studies is the same as that used by Wegener *et al.* [37], Teshome *et al.* [47–49], Rodriguez *et al.* [45], and Dattarajan *et al.* [36, 44], with modifications to systems pertaining to acoustic characterization and flame imaging, among others. In addition to relevant components of the apparatus, this chapter will discuss the overall experimental procedure and the evaluation of measured quantities.

## 2.1 Acoustic Waveguide

In present experiments, planar standing acoustic waves within a cylindrical waveguide were generated via two loudspeakers placed at each end of the waveguide. A schematic of the experimental apparatus, including the waveguide and associated diagnostics, is shown in Figure 2.1. The waveguide, made of aluminum tubing, had an inner diameter of 11.4 cm and a total length of 90 cm. A protruding copper shroud was situated centrally lengthwise on the surface of the waveguide. The shroud housed a removable borosilicate glass capillary that continuously fed a burning fuel droplet suspended at the center of the waveguide. Quartz windows were positioned on the surface of the waveguide along the line of sight of the burning droplet to provide optical access.

Ordinary loudspeakers were employed in the establishment of acoustic standing waves. These woofer type 8 Ω loudspeakers, rated at a maximum power output of 35 W, were placed at both ends of the waveguide. Three circumferentially distributed aluminum rods connected the speakers and allowed the pair to move left and right within the waveguide as an

assembly. The rods maintained a constant effective acoustic length, $L$, between the speakers in all experimental trials. The complete apparatus operated at atmospheric pressure and room temperature.

Sinusoidal forcing signals were applied to each loudspeaker via a data acquisition board (DAQ) controlled using LabVIEW$^{\text{TM}}$. A stereo amplifier, serving as an intermediary between the DAQ and the loudspeakers, administered a constant voltage gain to the forcing signals. The speakers were connected to the amplifier so as to impart a half period phase difference ($\Delta\phi = 180°$) between individual forcing signals; hence, the speaker pair functioned out-of-phase. Due to the constant $L$ separating the speakers, the acoustic frequency $f_a$ of the forcing signal could be strategically selected to generate a resonant standing waveform within the waveguide. In theory, $f_a$ is chosen such that $L$ is an integral multiple of half the acoustic wavelength, $\frac{1}{2}\lambda = \frac{1}{2}\frac{c}{f_a}$, where $c$ is the local speed of sound; that is,

$$L = \frac{n}{2}\lambda = \frac{n}{2}(\frac{c}{f_a}). \tag{2.1}$$

Speakers forced out-of-phase ($\Delta\phi = 180°$) will create a pressure node (PN) at the center of the waveguide regardless of the applied $f_a$ [50], as elaborated in Appendix A. However, forcing frequencies calculated through Eq. (2.1) correspond to acoustically resonant conditions and yield the largest pressure perturbation amplitudes at pressure antinode (PAN) locations within the waveguide. This implies that while any frequency can be used to produce a PN condition in the center of the waveguide, only few $f_a$ result in significant perturbation magnitudes at PAN regions. These observations are valid when acoustic perturbations from the loudspeakers are identical, as is maintained in present experiments.

Characterization of standing waves was achieved through point-like pressure measurements taken at centimeter intervals along the length of the waveguide. The flush mounted Kulite XCE-093-50D miniature pressure transducer utilized had a diameter of 2.4 mm, a length of 9.5 mm, and a sensitivity rating of 0.29 mV/kPa. The sinusoidal transducer voltage output was amplified before being used to calculate pressure perturbation $p'$ using an operational amplifier. As discussed, $f_a$ near frequencies resulting in resonance conditions

yield larger maximum $p'$ at PAN locations such as those in the immediate vicinity of the speaker. Thus, an optimum range of operating $f_a$ was compiled by measuring $p'$ at the speaker location while sweeping through $f_a$. Figure 2.2, from Wegener [37], shows the results of this frequency sweep method for out-of-phase speaker forcing. Pressure perturbations magnitudes at the center of the waveguide, minimized for those $f_a$ producing largest $p'$ at the speaker location, are also shown. Forcing frequencies selected per the abovementioned criteria and corresponding theoretical resonant frequencies calculated with Eq. (2.1) are listed in Table 2.1, along with complementary acoustic wavelengths for each.

Repositionable standing waves created through out-of-phase speaker operation permitted the investigation of spatially variable combustion profiles. Standing acoustic waves feature regions of maxima in velocity perturbations $u'$ at pressure nodes; conversely, weak or negligible velocity perturbations occur at PAN locations. Translating the speaker-rod assembly with respect to the stationary droplet effectively displaced the standing wave structure, as well as regions of high and low velocity and pressure perturbations, with respect to the droplet. Experiments enlisted this arrangement to explore the correlation between velocity and pressure perturbations at different locations within the waveguide and parameters relevant to the burning droplet, such as mean burning rate constant and heat release rate. The axial distribution of pressure nodes and antinodes at half-wavelength intervals within the waveguide was controlled with $f_a$. To compare spatial relationships across different $f_a$, results are presented with respect to displacement between the central PN and the droplet in fractions of acoustic wavelength, values which change with frequency, instead of explicit waveguide location $x$. Waveguide location $x$ is defined as the centimeter offset distance of the nearest PN relative to the droplet position at the center of the waveguide.

Pressure perturbation amplitude measurements collected during out-of-phase speaker-speaker operation for the forcing frequencies 332 Hz, 898 Hz, and 1500 Hz are given in Figure 2.3 and Figure 2.4. All experiments were conducted using standing waves with a maximum $p'$, or $p'_{max}$, magnitude of 150 Pa. Pressure measurements at PAN locations closest to the center of the waveguide for each specific forcing frequency verified $p'_{max}$ before

every experimental trial. The PAN locations closest to the centrally situated PN in the vicinity of the suspended droplet correspond to a quarter-wavelength displacement from the center of the waveguide. The acoustic wavelength and the quarter wavelength location of $p'_{max}$ measurements are tabulated in Table 2.1 for each forcing frequency.

Experiments by Dattarajan [44] and Rodriguez [45] operated using a speaker-reflector (S&R) configuration. Teshome [47], however, enhanced both symmetry in $p'$ measurements about the center of the waveguide and maximum $p'$ achievable at PAN locations by employing a speaker-speaker (S&S) configuration instead. Wegener [37] further investigated the difference in the S&R and S&S arrangements, as well as the acoustic characterization of S&S arrangements where speakers were forced in-phase ($\Delta\phi = 0°$) and out-of-phase ($\Delta\phi = 180°$). Ultimately both concluded that the improved symmetry of a two speaker apparatus made it a more desirable configuration.

### 2.1.1 Pressure Perturbation Amplitude Feedback Control

Experiment trials were categorized by their respective acoustic standing waves, namely through the forcing frequency $f_a$ and the maximum pressure perturbation amplitude $p'_{max}$ of each waveform. Operating frequencies were programmed into the LabVIEW$^{TM}$ virtual instrument responsible for generating the acoustic forcing signal fed to the speakers. Prescription of $p'_{max}$ before experiments was achieved using a proportional feedback loop controlling the command voltage amplitude of the aforementioned forcing signal, $V_{comm}$, output through a National Instruments USB-6251 DAQ. A stereo amplifier serving as an intermediary between the DAQ and the loudspeakers provided a constant, dial-set amplifier gain, $\kappa_{amp}$, that augmented the input voltage applied to the speaker assembly, $V_{speaker}$.

The proportional control scheme modeled the entire acoustic assembly, composed of the speaker pair, waveguide, and pressure transducer, as a plant with inputs $V_{speaker}$ alongside ambient noise and output $V_{PT,raw}$, the untreated output of the transducer. An operational amplifier circuit with measured gain $\kappa_{op}$ was constructed to boost output pressure signals

to magnitudes easily discernible through diagnostic equipment. The final transducer voltage, $V_{PT}$, was calculated from $V_{PT,raw}$ with $\kappa_{op}$ and fed back to alter the initial $V_{comm}$. A known voltage corresponding to the desired pressure perturbation amplitudes to be set in Pascals, nominally 150 Pa, was compared with $V_{PT}$ to produce an error voltage $\Delta V_{PT}$. This error voltage is scaled proportionately and added to the original $V_{comm}$ to yield an updated transducer output closer to the desired $p'_{max}$. The feedback loop was implemented upon the activation of the acoustics and iterated until $V_{comm}$ matched the specified $p'_{max}$ within a five percent margin. The block diagram outlining the operation of the pressure amplitude feedback control loop is presented in Figure 2.5.

The feedback control loop was designed to converge on a user-defined $p'_{max}$ across a range of operating conditions. $V_{comm}$ necessary to achieve the desired $p'_{max}$ varied between flow conditions on account of the frequency response of the loudspeaker assembly. In addition, the amplifier circuit utilized to magnify the initial transducer output also displayed nonuniform response with respect to $f_a$. The spectral profiles of the PT amplifier circuit gain $\kappa_{op}$ and of an individual speaker within the assembly are shown in Figure 2.6.

## 2.2 Droplet Maintenance and Ignition

A liquid fuel droplet was formed in the center of the waveguide via a borosilicate glass capillary. The suspended droplet was maintained at the tip of the capillary by matching fuel consumed through combustion with fuel administered through the capillary. The capillary had an approximate inner diameter of 0.39 mm, and volumetric fuel flow rate, $Q_v$, was set using a KDS Model 100 syringe pump. Flow rates ranging from 3.4 to 3.9 milliliters per hour, depending on the burning rate in each experiment, were held constant throughout individual trials. The borosilicate capillary was placed inside a protective copper shroud to prevent incoming fuel vaporization caused by heating from the suspended flame. Prior studies by Dattarajan [44] established an ideal separation of the shroud from the capillary tip ranging from 3 to 3.2 millimeters. This offset minimized interference introduced by the

shroud, adequately prevented boiling of fuel within the capillary, and maintained a burning rate independent of capillary-shroud separation. The exposed shroud on the surface of the waveguide was cooled with compressed air to promote conduction of heat from the capillary to the shroud. The droplet was ignited with a nickel cadmium resistive heating wire removed for the duration of each experiment to avert interaction with the acoustic waveform. This ignition procedure was identical for all fuels utilized, whose properties are summarized in Table 2.2. Once lit, the burning droplet was susceptible to extinction by strong convective flow, expulsion of vaporized fuel within the capillary, or complete consumption of oxidizer in the vicinity of the droplet. In the case of the latter, purging of the waveguide with air between experiments eliminated the potential for such extinguishment.

## 2.3 Image and Pressure Diagnostics

Combustion footage capturing features of the flame and droplet was recorded through an intensified camera system. The optical arrangement was optimized to visualize hydroxyl radical chemiluminescence, a global spectropic measurement validated as a quantification of heat release rate [51], primarily situated in the flame reaction zone at the flame front [34, 35]. Image acquisition through a LaVision Nanostar intensified CCD camera hardware was synchronized with the speaker forcing signal to determine the relative temporal location of each exposure with respect to the relative phase of the acoustic cycle. Time resolved $p'$ measurements correspondent to each frame of the combustion footage were also collected through triggered acquirement managed by a National Instruments USB-6251 DAQ board, ultimately enabling the correlation between relative periodic phase of heat release rate and pressure perturbation. A description of the equipment arrangement and synchronization is discussed in detail below.

### 2.3.1 Optical Assembly

The combustion reactions of various hydrocarbon fuels have been characterized by the presence of chain carrier species with a variety of spectroscopic properties. A prevalent intermediate reaction involves methylidyne (CH), formed through decomposition of hydrocarbon chains, interacting with diatomic oxygen to generate an electronically excited hydroxyl radical (OH*) and carbon monoxide [33]; in other words,

$$CH(^2\Pi_u) + O_2(^3\Sigma_g) \rightarrow CO(^1\Sigma^+) + OH^*(^2\Sigma^+). \tag{2.2}$$

Produced OH* decays through two mechanisms: collisional quenching and radiative deexcitation, a process also known as chemiluminescence. Spatial luminosity profiles established through chemiluminescence of excited radicals are capable of discriminating global properties of distinct fuel chemistries [33, 52]. In particular, OH* chemiluminescence has been categorized as a proven marker of heat release rate in a variety of premixed systems [53–57]. Experimental and numerical studies have also demonstrated that OH* chemiluminescence generally demarcates flame position and primary reaction zones, as well as maximum temperature regions, in burning droplets within microgravity environments [34, 35]. Computational validation of experiments by De Leo *et al.* [51] positively correlates hydroxyl radical luminosity and heat release within nonpremixed regimes as well. Several others, like Sliphorst *et al.* [58] and Gopalakrishnan *et al.* [59], conducted experiments that demanded unobtrusive quantification of heat release through optical OH* diagnostics for diffusion flames. Hence, the optical components employed in conjunction with the intensified camera system in this study were designed to transmit and capture photons emitted through the hydroxyl radical relaxation reaction given as

$$OH^*(^2\Sigma^+) \rightarrow OH(^2\Pi) + h\nu. \tag{2.3}$$

Based on the findings of others [51, 58, 59], the measured OH* chemiluminescence intensity was assumed to correlate directly with heat release rate.

Luminescent emission of deexcited hydroxy radicals occurs predominantly in the ultraviolet (UV) spectrum, specifically within a narrow wavelength band centered about 308

nanometers [55, 60]. As such, constituents of the optical train were optimized for transmission of UV light with minor absorption properties. The viewing windows installed to provide optical access to the burning droplet and the camera lens attachment (UV-Nikkor 105mm f/4.5) were made of quartz, an efficient UV transmitter. An optical bandpass filter attached to the lens isolated UV emissions and mitigated incident ambient luminosity. The light-sensitive photocathode component in the Nanostar camera operated at the greatest efficiencies for wavelengths between 200 and 450 nanometers. Individual transmittance profiles over a range of incident light wavelength for each element in the optical assembly are given in Figure 2.7, while the combined transmittance of the assembly is given in Figure 2.8. Chemiluminescent profiles for different radicals, including OH*, observed in the combustion of methane at typical emission wavelengths derived by Kojima *et al.* [60] are also presented in Figure 2.8 for comparison.

### 2.3.2 Diagnostic Equipment

#### 2.3.2.1 Nanostar Camera and DaVis Software

Droplet combustion footage was recorded and organized by use of LaVision imaging products, namely the Nanostar intensified charge-coupled device (ICCD) camera and the DaVis 8 software package. The Nanostar ICCD camera architecture enabled the acquisition of images with luminous intensities extending through the UV spectrum associated to every pixel at photon-level sensitivities [61]. Incident light filters through the optical train and focuses onto the first intensifier component, a photocathode. The photocathode receives impinging photons and emits electrons whose flow is governed by the polarity of an administered voltage, essentially forming an electronic shutter capable of nanosecond exposure times as mandated by the user through the DaVis software. Upon application of a positive voltage, the photocathode conducts electrons through the next intensifier element: the multi-channel plate (MCP). The MCP generates a quantity of electrons proportional that of arriving electrons. The factor of proportionality through which the MCP amplifies electron flow is controlled

by an input voltage calibrated as an intensifier gain and prescribed by the user via DaVis. The final intensifier constituent is a phosphor screen that collects electrons from the MCP and ejects photons correspondingly. These output photons are relayed through a final set of optics to a CCD array arranged in a grid analogous to pixels in the final image. The CCD array converts collected photons to electric charge used to compose an exposure that is eventually translated to the computer via fiber optics. A schematic of the Nanostar intensifier arrangement is presented in Figure 2.9, while nominal camera specifications are listed in Table 2.3.

The user interfaced with the Nanostar camera through input and output voltage signals, essential in diagnostic synchronization, and with DaVis 8. Customizable settings within DaVis 8 allowed for specification of the trigger frequency for image acquisition, the gate time associated with activation of the photocathode correspondent to the image exposure, the gain of the MCP electron multiplication contributing to image brightness, and the time delays set to forestall recording of images in sequence, among a host of other parameters. Typically, total light input proved a dominant factor in the degree of image quality. Isolating the flame dynamics for a particular relative acoustic phase necessitated that recording occur within a small fraction of the acoustic period. Therefore, to avoid blurring of the flame characteristics across large portions of the acoustic cycle, a gate activation time interval $\Delta t_{gate}$ equal to one seventy-second of the acoustic time period for the given forcing frequency, or $T_a/72 = 1/72 f_a$, was held constant while image exposures were recorded. This resulted in much higher light input in images corresponding to conditions of large $T_a$ and, thus, small $f_a$. To circumvent the lighting discrepancy between images at distinct $f_a$, the MCP gain was adjusted to maintain acceptable lighting in all exposures. A software feature allowing multiple exposures to be collected for the composition of a single image, a setting referred to as "burst mode", was also employed to normalize image quality. In the trials exploring the more luminous hydrocarbon fuels like JP-8 and FT, limiting the number of exposures within a single image, referred to as the "burst count", and lowering the MCP gain protected the intensifier elements and CCD array from over-exposure.

#### 2.3.2.2 National Instruments Data Acquisition Board and LabVIEW™

The signals relayed to and from the camera, pressure transducer, and computer software were managed through a National Instruments USB-6251 DAQ board. The user and DAQ interfaced through a LabVIEW™ virtual instrument (VI) developed for the purpose of generating sinusoidal speaker forcing signals, establishing $p'_{max}$ at the PAN location of a specific flow condition through proportional feedback control, providing a recording signal as an input to the Nanostar camera, and logging dynamic PT data upon detection of a trigger signal present during image acquisition. The continuous input sampling rate of the PT signal was preset at 750 kHz throughout all experiments to maintain a quasi-continuum of pressure data regardless of forcing frequency. Through similar rationale, the loudspeaker output signal was supplied at a sampling rate of 850 kHz in all experiments. Signal amplitudes affiliated with the loudspeaker and camera systems were typically measured in volts; conversely, the maximum PT signal amplitudes rarely exceeded 30 millivolts. The USB-6251 DAQ model offered a broad output voltage range while maintaining high sensitivity to low magnitude inputs. Extended specifications for the USB-6251 DAQ model are listed in Table 2.4 [62].

### 2.3.3 Hardware Synchronization

Control of the signals distributed by the DAQ and the Nanostar camera was an integral focus in the design of the LabVIEW™ VI tasked with synchronizing dynamic PT readout and image acquisition. As alluded to in the above, the Nanostar operation is characterized by input and output voltage signals. The input 0-5 V TTL signal imparts information regarding the trigger frequency designed to match that of the acoustics and the initiation of an exposure to the Nanostar. Traditional LaVision systems generate this TTL signal given the user-defined timing scheme with an included programmable timing unit (PTU) that interacts automatically with DaVis. The PTU hardware functionality while in burst mode, though, was limited to a trigger frequency of 200 Hz, an inadequately low value given the operational $f_a$ explored in the experiment. In consequence, the same parameters fed to the

DaVis software were used to generate the input camera signal via LabVIEW$^{TM}$ through the DAQ. The board also received the Nanostar camera output signal: another 0-5 V TTL signal pulsed by the electronic gating of the photocathode during exposures. Since the Nanostar gating signal was activated by the intensifier operation during the formation of an image, this output signal maintained its "high" 5 V setting for the duration $\Delta t_{gate}$. This provided an appropriate triggering signal that directed the DAQ to collect pressure data only while an exposure was recorded.

Pressure and image logging phase-locked to different temporal locations within the acoustic cycle was enabled through delays imparted between the signals input to the speaker assembly and camera. The input signal to the camera controlled the initiation of image acquisition and was, by the default protocol in LabVIEW$^{TM}$, in-phase with the speaker forcing signal also generated through the VI. Hence, by applying an acoustic phase delay $\Delta\phi_a$ in the form of a time offset between the two signals, recording of image and pressure data could be synchronized at various instances within the acoustic forcing period. The recording scheme implemented in this experiment gathered fifteen sets of triggered pressure perturbation and optically assessed combustion data per individual acoustic cycle over four total acoustic cycles by adjusting $\Delta\phi_a$ after subsequent image acquisitions in order to achieve a near-continuous temporal profile.

The quality of phase-locking achieved through this strategy hinged on adjustment of component time delays, such as those inherent to the DAQ, the stereo amplifier, the speaker assembly, the waveguide air motion, the PT, the PT op amp circuit, and the cable wiring. In addition, a hardware time delay of 20 ns between the triggering of an image and the initiation of an exposure via the photocathode innate to the Nanostar operation also required consideration. Ultimately the calibration of these delays ensured reproducible synchronization between the recording of dynamic $p'$ values and combustion footage at a range of $\phi_a$ relative to the acoustic period.

## 2.4 Measurement Methods

### 2.4.1 Burning Rate Constant

From continuity for a spherical droplet of diameter $d$, the instantaneous burning rate constant $K$ may be evaluated via

$$K = \frac{4Q_v}{\pi d(t)} - 2d\dot{d}. \tag{2.4}$$

A fixed volumetric flowrate $Q_v$ was administered with the syringe pump so as to regulate the droplet size throughout individual experiments. Investigations by Teshome *et al.* [47–49] and Wegener [37] underline that the transient term presented in this formulation of $K$ provides a negligible contribution to the final calculated burning rate constant. Note also that the limiting condition where $Q_v = 0$ reverts Eq. (2.4) to the traditional $d^2$ law [25, 26]. The continuously-fed expression of $K$ is incompatible with oblong droplet geometries derivative of the gravitational environment. Thus, use of Eq. (2.4) was made possible through the estimation of an equivalent spherical droplet diameter $d_{eqvs}$ based on volume matching with a recorded droplet modeled with a prolate spheroid, as done by Struk *et al.* [30]. The recorded droplet boundary of each frame in the combustion footage was digitized and processed using a custom MATLAB$^{\text{TM}}$ edge-detection subroutine. The MATLAB$^{\text{TM}}$ algorithm was capable of discerning ambient pixels from those of the droplet via heightened contrast provided by a single LED back-light. Values of $d_{eqvs}$ calculated from recorded droplet volumes were used to compute time-averaged $K$ for each trial.

### 2.4.2 Acoustic Acceleration

In the absence of acoustic excitation, the sole net force acting on the burning system of hot combustion products with density $\rho_p$ and volume $\mathcal{V}$ is buoyancy. In an environment with established ambient density $\rho_o$ and gravitational acceleration $g_o$, the presence of the buoyancy force, given by $F_b = (\rho_p - \rho_o)\mathcal{V}g_o$, results in a vertically oriented, symmetric flame. While under acoustic forcing, the simple model for a burning droplet provided by the theory

of Tanabe *et al.* [41–43] suggests that the flame aligns itself with the resultant force due to buoyancy and a homologous acoustic radiation force, $F_a = (\rho_p - \rho_o)\mathcal{V}g_a$, where $g_a$ represents the acoustic acceleration as defined in Eq. (1.2). Figure 2.10 depicts the influence of the acoustics on the burning droplet.

According to the theory suggested by Tanabe *et al.* [42] formulated through the work of Nyborg [63], the magnitude and sign of $g_a$ depend on the position of the burning system relative to neighboring PN and PAN. An experimental acoustic acceleration, $g_{a,exp}$, can be estimated through the degree of flame deflection $\phi_f$ through

$$g_{a,exp} = g_o \tan \phi_f. \tag{2.5}$$

The deflection angle $\phi_f$ is measured as the average change in orientation between the tangent lines to the unforced and forced flame axes, as shown in Figure 2.10. This formulation of $g_{a,exp}$ is subject to increased uncertainty for conditions conducive to severe flame deflections because the plume region turns upward in the far wake of the flame.

### 2.4.3 Flame Standoff Distance

In contrast to the spherical structure of flames surrounding fuel droplets burning in microgravity conditions, quasi-elliptical flames envelop burning droplets in gravitational environments. The flame standoff distance $\delta_f$ measured in both forced and unforced regimes is a function of the polar coordinate angle $\theta$ measured from the positive $x$ axis of the $x-y$ plane whose origin coincides with the droplet center, as detailed in Figure 2.10. Standoff distance is geometrically defined as $\delta_f = r_f - r_s$, where the flame radius $r_f$ and the droplet radius $r_s$ are both measured relative to the center of the droplet using the MATLAB$^{\text{TM}}$ edge-detection subroutine as functions of $\theta$ . While relative contrast between the ambient and droplet pixels is essential to the computation of $r_s$, ascertaining the flame boundary responsible for calculating $r_f$ is achieved using the location of maximum OH* chemiluminescence intensity for a given value of $\theta$. This topological definition for the flame front is a prevalent feature in a variety of studies pertaining to diffusion and premixed combustion [31, 34, 35, 60]. The

analysis of $\delta_f$ within the context of this study will focus on the stagnation region of the flame, as determined by the acoustic flow conditions. The flame stagnation region, as opposed to the flame wake region, is consistently counter-oriented with respect to the direction of flame alignment. The stagnation region, then, may fluctuate between trials as the direction of flame deflection changes depending on the droplet position relative to the PN. In general, only the measurements $\delta_f(\theta = 0^o)$ and $\delta_f(\theta = 180^o)$ are considered, depending on which corresponds to the flame stagnation region.

Select limitations are involved in the treatment of $\delta_f$ presented here. First, an azimuthally uniform assessment of the flame standoff distance with respect to the out-of-plane angle $\psi$ is not completely physical. While this is not directly relevant in the two-dimensional geometries assumed here, the method by which the maximum OH* chemiluminescence is taken to represent the flame boundary could introduce bias uncertainty as a particular recorded pixel luminosity actually represents that of all superimposed portions of the flame within the optical line-of-sight. More fundamentally, hydroxyl chemiluminescence measurements fail to detect ongoing combustion reactions that a host of other carbon-based radical species appropriately expose, particularly in flames near the extinction strain limit. Furthermore, several other spectroscopic mechanisms, like maximum C* and CH* luminosities, have been validated to correlate with extents of flame topologies, especially in turbulent premixed reactions. Hence the applicability of maximum OH* chemiluminescence as a marker for the diffusion flame boundary, while imperfect, is quite reasonable in this body of work. This assumption is particularly valid here as extinction and turbulence conditions are avoided for all applied oscillating flows regardless acoustic excitation amplitudes.

### 2.4.4 Rayleigh Index

Combustion instability inherent in a reactive system can be interpreted using the Rayleigh criterion. The classical formulation of the Rayleigh criterion [2] asserts that amplification of instabilities occurs in systems where perturbations in pressure, $p'$, oscillate in-phase with perturbations in heat release rate, $q'$, while attenuation of such instabilities is encountered

when the fluctuating $p'$ and $q'$ are out-of-phase. The resultant stability dictated through the Rayleigh criterion over an interrogation period $T$ can be quantified using the Rayleigh index $G$, given by

$$G(x) = \frac{1}{T}\int_T p'(x,t)q'(x,t)\mathrm{d}t. \tag{2.6}$$

Positive values of $G$ coincide with in-phase pressure and heat release oscillations and portend enhanced instability; conversely, out-of-phase $p'$ and $q'$ resulting in the subsidence of instability yield negative $G$. The Rayleigh index for burning droplets in the present experiments was computed assuming a direct correlation between oscillatory heat release and OH* chemiluminescence intensity, discussed below. $G$ was determined at various droplet positions $x$ relative to the PN location after the discretization of the integration time $t$. Discretized evaluation of $G$ was prompted by the discontinuous profile of $p'$ and $q'$, which was inferred from OH* chemiluminescent intensity fluctuations in each frame of the combustion footage. An average Rayleigh index determined for each experimental trial incorporated sixty total sets of $p'$ and $q'$ data spanning over four consecutive acoustic cycles.

Refinement of the integrated OH* chemiluminescence analogous to heat release [51] was required prior to its use in the evaluation of the Rayleigh index. Preliminary measurements of $I$, the total image intensity integrated over every constituent pixel, for an unforced burning droplet revealed the onset of a rapid intensity deterioration, illustrated over three consecutive trials in Figure 2.11. While initially severe, the decay rate of $I$ appeared to stabilize after approximately fifteen to thirty seconds of unforced combustion. Interestingly, introducing the burning droplet to acoustic excitation at any instance following ignition immediately procured constant amplitude oscillations in the integrated intensity, $I'$, and a linear decay rate of the mean intensity $\overline{I}$, as demonstrated in Figure 2.12.

The precise mechanism resulting in the temporal degradation in OH* radiative deexcitation is unknown, although $O_2$ consumption over tens of seconds was one likely culprit. In this context, it was observed that sequential purging or venting of the gaseous waveguide contents between trials restored the initial mean luminous intensities to repeatably consistent levels for a particular fuel; on the other hand, experiments conducted without prior flushing

of the waveguide exhibited reduced initial $I$ and $\overline{I}$. The reproducibility of these observations for each fuel and the accompanying intensity decay observed in all trials suggest that oxidizer mass fraction in the vicinity of the droplet, vital to the formation of hydroxyl radicals via Eq. (2.2), dissipates over time through reactive consumption and combustion product accumulation within the waveguide. This dual oxidizer dissipation and product accretion appears to reach a steady-state condition resulting in constant luminescent decay following sufficiently large time spans after ignition or through the application of acoustic forcing. The stable decay reached in the unforced system may indicate an equilibrium interaction of natural convection and ambient diffusion of species achieved over time, while near-instantaneous mean intensity decay imparted through acoustic forcing implies an accelerated version of the same equilibrium mechanism fostered by forced convection. To circumvent the effects of transient deterioration in OH* chemiluminescence on the evaluation of $G$, all image acquisition was performed upon entering a linear intensity decay regime.

## 2.5 Experimental Procedure

Experiments were preceded by inspection and adjustment of initial apparatus components. The syringe pump was first cleaned and loaded with the desired test fuel, which was followed by the attachment of the borosilicate glass capillary through a rubber tube. The volumetric flowrate $Q_v$ on the syringe pump was programmed to maintain an approximately constant droplet size. For all fuels in this investigation, the value of $Q_v$ was determined to be $1.025 \pm 0.05$ mm$^2$/sec. After purging of the waveguide to expel accumulated combustion products, the speaker assembly was translated to the desired relative location with respect to the fuel droplet. The pressure transducer was also relocated to the corresponding PAN location. Waveguide extensions employed in averting quarter-wave reflection at the ends of the waveguide, to be discussed in Chapter 3, were installed for the appropriate forcing frequencies and waveguide locations. Finally, the fuel flow was supplied, the droplet was ignited with the resistive heating wire, and the waveguide was resealed.

Introduction of acoustic forcing came ten to thirty seconds after droplet ignition, depending on the fuel. This time delay ensured the establishment of a constant decay regime in flame luminosity. The pressure amplitude calibrating control loop was implemented through LabVIEW$^{TM}$ to establish the input speaker voltage necessary to reach the desired $p'_{max}$ at the PAN location. Recording through the Nanostar camera upon completion of the acoustic calibration lasted between 80 and 120 seconds, depending on the frame rate calculated by DaVis for each flow condition. In total, four sets of fifteen phase-locked images taken at evenly spaced acoustic phase delays, $\phi_a = 24^o : 24^o : 360^o$, were recorded within this burning period. Triggered pressure data was exported through LabVIEW$^{TM}$ into .txt documents, while phase-locked images were digitized in .im7 format. An additional sixty background images taken without the capillary and shroud in the field of view were used to remove LED back-light intensity contributions during post-processing.

Data reduction of the pressure and image files was completed using MATLAB$^{TM}$ and DaVis software. Through DaVis, the average of the sixty background images was subtracted from each flame image. The processed background subtracted images were then analyzed through a MATLAB$^{TM}$ algorithm. The script fit ellipses to the droplet and flame structures within each frame of the combustion footage to compute experimental burning rate constant $K$ and flame deflection angle $\phi_f$. It then transformed the extant Cartesian coordinates of each image to polar coordinates, placing the origin at the fitted droplet center, for the analysis of flame standoff distance $\delta_f$ and integrated OH* chemiluminescence intensity oscillations $I'$. Individual intensity values for pixels below a specific threshold luminosity associated with image noise were excluded from the final integrated intensity. Between twenty and fifty $p'$ readings logged for each image were averaged and statistically segregated to remove noise and spurious outliers through a separate MATLAB$^{TM}$ subroutine.

## 2.6 Measurement Uncertainty

### 2.6.1 Precision Uncertainty

Precision uncertainty in the measured variables used to calculate the burning rate constant $K$ in Eq. (2.4) result from uncertainties in the volumetric flow rate $Q_v$ and computed equivalent sphere diameter $d_{eqvs}$ for the fuel droplet. The technique for calculating the uncertainty in $d_{eqvs}$ is similar to the method used by Dattarajan *et al.* [36] which utilizes the principles of uncertainty propagation in Mills and Chang [64], but with improved fidelity due to increased pixel resolution. The equivalent sphere diameter is derived using the major and minor axes of the ellipse fit to the droplet, modeled as an azimuthally symmetric prolate spheroid, via $d_{eqvs} = 2a^{\frac{2}{3}}b^{\frac{1}{3}}$. Assuming the uncertainties in the axes lengths, $a$ and $b$, are equal, equating the uncertainty in $d_{eqvs}$ is demonstrated here.

$$\begin{aligned}
\Delta d_{eqs} &= \sqrt{\left(\frac{\partial d_{eqs}}{\partial a}\Delta a\right)^2 + \left(\frac{\partial d_{eqs}}{\partial b}\Delta b\right)^2} \\
&= \sqrt{\left(\frac{2}{3}\frac{2b^{\frac{1}{3}}}{a^{\frac{1}{3}}}\Delta a\right)^2 + \left(\frac{1}{3}\frac{2a^{\frac{2}{3}}}{b^{\frac{2}{3}}}\Delta b\right)^2} \\
&= \sqrt{\left(\frac{4}{3}\Delta a\left[\frac{b}{a}\right]^{\frac{1}{3}}\right)^2 + \left(\frac{2}{3}\Delta b\left[\frac{a}{b}\right]^{\frac{2}{3}}\right)^2} \\
&= \Delta ab\sqrt{\frac{16}{9}\left[\frac{b}{a}\right]^{\frac{2}{3}} + \frac{4}{9}\left[\frac{b}{a}\right]^{-\frac{4}{3}}}
\end{aligned} \tag{2.7}$$

Again, it is assumed that $\Delta a = \Delta b = \Delta ab$. The numerical uncertainty in $d_{eqvs}$ is then calculated using $d_{eqvs} \approx 1.5$ mm, $\Delta ab \approx 0.05$ mm, and $\frac{b}{a} \approx 1.5$, giving an uncertainty of $\frac{\Delta d_{eqvs}}{d_{eqvs}} \approx 5.36\%$. Uncertainty in $Q_v$ is purely based on the precision uncertainty of the syringe pump. Therefore, the manufacturer's rating of 0.1% is used for $\frac{\Delta Q_v}{Q_v}$.

The uncertainties in $d_{eqvs}$ and $Q_v$ are compounded in $K$ follow as

$$\begin{aligned}\Delta K &= \sqrt{\left(\frac{\partial K}{\partial Q_v}\Delta Q_v\right)^2 + \left(\frac{\partial K}{\partial d_{eqs}}\Delta d_{eqs}\right)^2} \\ &= \sqrt{\left(\frac{4\Delta Q_v}{\pi d_{eqs}}\right)^2 + \left(-\frac{4Q_v}{\pi d_{eqs}^2}\Delta d_{eqs}\right)^2} \\ &= \sqrt{\left(K\frac{\Delta Q_v}{Q_v}\right)^2 + \left(-K\frac{\Delta d_{eqs}}{d_{eqs}}\right)^2} \\ &= K\sqrt{\left(\frac{\Delta Q_v}{Q_v}\right)^2 + \left(\frac{\Delta d_{eqs}}{d_{eqs}}\right)^2}\end{aligned} \tag{2.8}$$

The uncertainty in $K$ is $\frac{\Delta K}{K} = 5.4\%$ when $\frac{\Delta d_{eqvs}}{d_{eqvs}} \approx 5.36\%$ and $\frac{\Delta Q_v}{Q_v} = 0.1\%$, showing that fuel flow uncertainty has a negligible affect on total uncertainty in $K$. Note the transient term in Eq. (2.4) was omitted from this uncertainty analysis due to the minimal contribution it provides to the value of $K$. The precision uncertainty of time-averaged $K$ values can be found by accounting for the minimum number of experimental points used to encompass the burning rate constant for one flow condition, fifteen. The resulting precision uncertainty in average $K$ values is estimated to be $5.36\%/\sqrt{15} \approx 1.38\%$.

A similar procedure is employed for the calculation of precision uncertainty in the Rayleigh index. The discretized form of Eq. (2.6) used to compute $G$ by dividing the integration period $T$ into $m$ uniform intervals must be utilized, formulated as

$$G(x) \approx \sum_{i=1}^{m} p_i'(x)q_i'(x) = \sum_{i=1}^{m} p_i'(x)I_i'(x). \tag{2.9}$$

Contributions from both pressure and intensity perturbations must be considered in this analysis. The source of uncertainty for pressure perturbation measurements relies only in the accuracy rating of the pressure transducer on account of insignificant quantization error. The XCE-093-50D has an output signal reproducibility of 0.5% of the full scale output, $\Delta V = (0.005)(\text{FSO}) = (0.005)(100\text{ mV}) = 0.5\text{ mV}$. With a transducer sensitivity rating of

0.29 mV/kPa and a baseline operational amplifier gain $\kappa_{op}$ of 495, the calculation follows as

$$\begin{aligned}\Delta p' &= \sqrt{\left(\frac{\partial p'}{\partial V}\Delta V\right)^2} \\ &= \frac{\partial p'}{\partial V}\Delta V \\ &= \frac{\partial}{\partial V}\left(\frac{V}{\delta\kappa_{op}}\right)\Delta V \\ &= \frac{0.5 \text{ mV}}{\left(0.292\frac{\text{mV}}{\text{kPa}}\right)(495)} = 3.5 \text{ Pa}\end{aligned} \tag{2.10}$$

For the maximum pressure amplitude primarily used in this study, $p'_{max} = 150$ Pa, the precision uncertainty is $\frac{\Delta p'}{p'} \approx 2.31\%$. Uncertainty in $I'$, evaluated as a sum of pixel intensities with luminosities above a predefined threshold intensity, hinges on the intensity uncertainty in individual pixel intensity $\Delta I'$ and on the fraction of total image pixels $P$ selected for the computation. Typically about 30% of the constituent pixels within the active image area (1280x1024 pixels) were used, each with an uncertainty of a single "count" unit of chemiluminescence. Thus, the absolute uncertainty follows as

$$\begin{aligned}\Delta I' &= \sum_{i=1}^{P} \Delta I'_i \\ &= P\Delta I'_i \\ &= (0.3)(1280)(1024)\Delta I'_i = 3.93 \cdot 10^5 \text{ counts}\end{aligned} \tag{2.11}$$

Nominal magnitudes of $I'$ scaled with $10^7$ counts, yielding a precision uncertainty of $\frac{\Delta I'}{I'} \approx 3.93\%$.

With knowledge of the precision uncertainties in both $p'$ and $I'$, we formulate the uncertainty in $G$ as the sum of uncertainties in the product of pressure and intensity oscillations. Evaluating the absolute error $\Delta(p'I')$ for a general $i^{\text{th}}$ term in the sum and substituting into

the expression for $\Delta G$ gives

$$\Delta G = \Delta(p_1' I_1') + \Delta(p_2' I_2') + \ldots + \Delta(p_m' I_m') \tag{2.12}$$

$$\Delta(p_i' I_i') = p_i' I_i' \sqrt{\left(\frac{\Delta p_i'}{p_i'}\right)^2 + \left(\frac{\Delta I_i'}{I_i'}\right)^2}$$

$$\Delta G = \sum_{i=1}^{m} p_i' I_i' \sqrt{\left(\frac{\Delta p_i'}{p_i'}\right)^2 + \left(\frac{\Delta I_i'}{I_i'}\right)^2}$$

Recognizing that relative errors in $p'$ and $I'$ are independent of each $i^{\text{th}}$ term prompts factoring of the square root term outside of the sum, which, after simplification, reveals the precision uncertainty of $G$ as follows

$$\begin{aligned} \Delta G &= \sum_{i=1}^{m} p_i' I_i' \sqrt{\left(\frac{\Delta p_i'}{p_i'}\right)^2 + \left(\frac{\Delta I_i'}{I_i'}\right)^2} \\ &= \left(\sum_{i=1}^{m} p_i' I_i'\right) \sqrt{\left(\frac{\Delta p'}{p'}\right)^2 + \left(\frac{\Delta I'}{I'}\right)^2} \\ &= G \sqrt{\left(\frac{\Delta p'}{p'}\right)^2 + \left(\frac{\Delta I'}{I'}\right)^2} \end{aligned} \tag{2.13}$$

The uncertainty in $G$ is $\frac{\Delta G}{G} = 4.56\%$ when $\frac{\Delta p'}{p'} \approx 2.31\%$ and $\frac{\Delta I'}{I'} \approx 3.93\%$. As with the burning rate constant $K$, the precision uncertainty for time-averaged $G$ relies on the minimum number of Rayleigh indices averaged to attain the final value, three. Thus, the precision uncertainty for the average $G$ is approximately $4.56\%/\sqrt{3} \approx 2.63\%$.

### 2.6.2 Bias Uncertainty

Sources of bias uncertainty in $K$ include a 1% accuracy rating for $Q_v$ and bias due to pixelation of the droplet boundary. The latter form is present in all experiments where the MATLAB$^{\text{TM}}$ algorithm carries out edge detection. For these studies, the Nanostar's high spatial resolution results in pixel dimmensions of 7.3 $\mu$m, implying that droplet edge detection bias is negligibly small relative to precision uncertainties and error from the droplet ellipse fit process. This ellipse fit technique, the third source of bias uncertainty discussed here, is largely connected to errors from equating the diameter of the droplet ellipse with the

diameter of a sphere of equivalent diameter $d_{eqvs}$. A detailed analysis in which alternatives to this technique for choosing an appropriate droplet diameter $d$ are quantitatively compared by Dattarajan *et al* [36]. Nevertheless, deviations in the accuracy of the ellipse fit itself must be considered. Surface tension and gravitational forces distort the droplet into a teardrop-like shape, where an ellipse fit consistently matches the lower edge of the droplet but over estimates the volume in the upper portion of the droplet. This asymmetric tracking of the droplet boundary produces burning rate constant $K$ that are under estimated by enlarged droplet volumes. Flame standoff distance measurements are unperturbed by this effect because this study is interested in standoff distance for the lower hemisphere of the droplet, which comprises the principal reaction zone.

As alluded to beforehand, bias uncertainties in the chemiluminescent intensity and flame standoff distance measurement are engendered by the recording procedure. A burning droplet image is the untreated projection a three-dimensional reaction zone onto a two-dimensional footage frame, which misrepresents flame curvature. Well-studied deconvolution methods like the Abel transform [65] are capable of transforming an axisymmetric image of a three-dimensional field into an image representing a 2-D plane view. But the deflection imparted through the bulk acoustic force yield non-axisymmetric flames in acoustic environments. All combustion footage analyzed under acoustic forcing, then, is subject to line-of-sight error. Defining the flame as the locus of points coincident with peak OH* chemiluminescence, as described in Section 2.4.3, provides additional bias error on account of this line-of-sight discrepancy because the measured flame standoff distance is less than the true distance.

Table 2.1: Theoretical and Experimental Resonant Frequencies and Wavelengths

| Speaker-Speaker, $\Delta\phi = 180^o$ (PN at $x = 0$ cm) | | | | | | | |
|---|---|---|---|---|---|---|---|
| Theoretical | | | | Experimental | | | |
| $n$ | $f_{th}$ [Hz] | $\lambda_{th}$ [cm] | $\frac{1}{4}\lambda_{th}$ [cm] | $n$ | $f_{exp}$ [Hz] | $\lambda_{exp}$ [cm] | $\frac{1}{4}\lambda_{exp}$ [cm] |
| 1 | 281.2 | 122.0 | 30.5 | 1 | 332 | 103.3 | 25.8 |
| 3 | 843.4 | 40.7 | 10.2 | 3 | 898 | 38.2 | 9.5 |
| 5 | 1405.7 | 24.4 | 6.1 | 5 | 1500 | 22.9 | 5.7 |

Table 2.2: Fuel Properties (Alcohol fuels [26]; Hydrocarbon fuels [66–71])

| Fuel Property | Methanol | Ethanol | Pure JP-8 | Pure FT |
|---|---|---|---|---|
| Chemical Formula | $CH_3OH$ | $C_2H_5OH$ | $C_{11}H_{21}^{\dagger}$ | $C_{12}H_{25}^{\dagger}$ |
| Molecular Weight [kg/kmol] | 32.04 | 46.17 | 147.83† | 164.79† |
| Stoichiometric Air-Fuel Ratio | 6.433 | 8.948 | 15.105† | 15.218† |
| Specific Heat Capacity* [kJ/kg·K] | 2.47 | 2.42 | 1.92 | 2.73 |
| Thermal Conductivity* [W/m·K] | 0.204 | 0.179 | 0.115 | 0.00935 |
| Kinematic Viscosity* [$mm^2/s$] | 0.715 | 1.452 | 1.646 | 1.536 |
| Liquid Density* [$kg/m^3$] | 789.8 | 798.9 | 776.0 | 754.0 |
| Freezing Temperature [K] | 1753.3 | 158 | 222.7 | 218.7 |
| Heat of Vaporization [kJ/kg] | 1104 | 841 | 441 | 339 |
| Heat of Combustion [kJ/kg] | 19930 | 26952 | 43421 | 44136 |

†Estimated from reference carbon-hydrogen ratios and percent hydrogen mass content

*Calculated for $T \approx 295$ K and $p \approx 1$ atm

Table 2.3: Nanostar Camera Specifications [61]

| | |
|---|---|
| Maximum Frame Rate | 8 Hz |
| Dynamic Range | 4096 |
| Active Image Area | 1280 x 1024 pixels |
| Pixel Size | 6.7 $\mu$m x 6.7 $\mu$m |
| Field of View | 9.3 mm x 7.4 mm |
| Pixel View | 7.3 $\mu$m x 7.3 $\mu$m |
| Depth of Field | 2 mm |
| CCD Readout Noise | $<$ 2 counts (RMS) |

Table 2.4: NI USB-6251 DAQ Specifications [62]

| Analog Input | |
|---|---|
| Channels | 8 |
| Maximum Sample Rate | 1.25 MS/s |
| Resolution | 16 bits |
| Maximum Voltage Range | -10 V to 10 V |
| Maximum Voltage Range Accuracy | 1.92 mV |
| Minimum Voltage Range | -100 mV to 100 mV |
| Minimum Voltage Range Accuracy | 52 $\mu$V |
| Onboard Memory | 4095 samples |
| **Analog Output** | |
| Channels | 2 |
| Maximum Update Rate | 2.86 MS/s |
| Resolution | 16 bits |
| Maximum Voltage Range | -10 V to 10 V |
| Maximum Voltage Range Accuracy | 2.08 mV |
| Minimum Voltage Range | -5 V to 5 V |
| Minimum Voltage Range Accuracy | 1.045 mV |

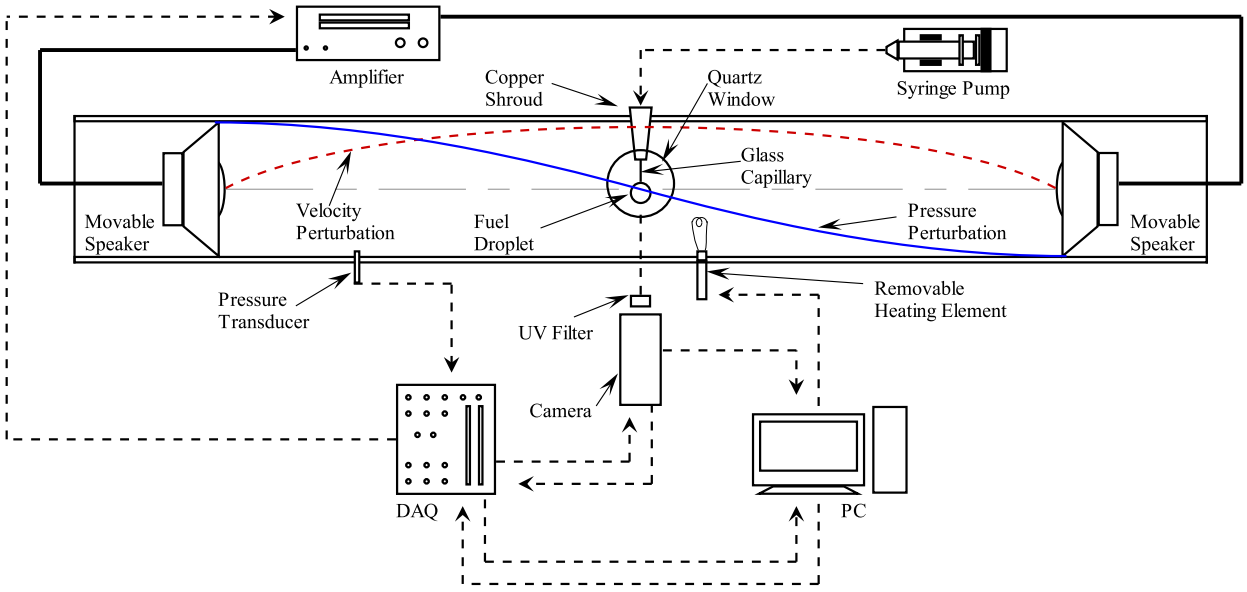


Figure 2.1: Experimental apparatus, with fuel delivery, imaging, and pressure logging subsystems.

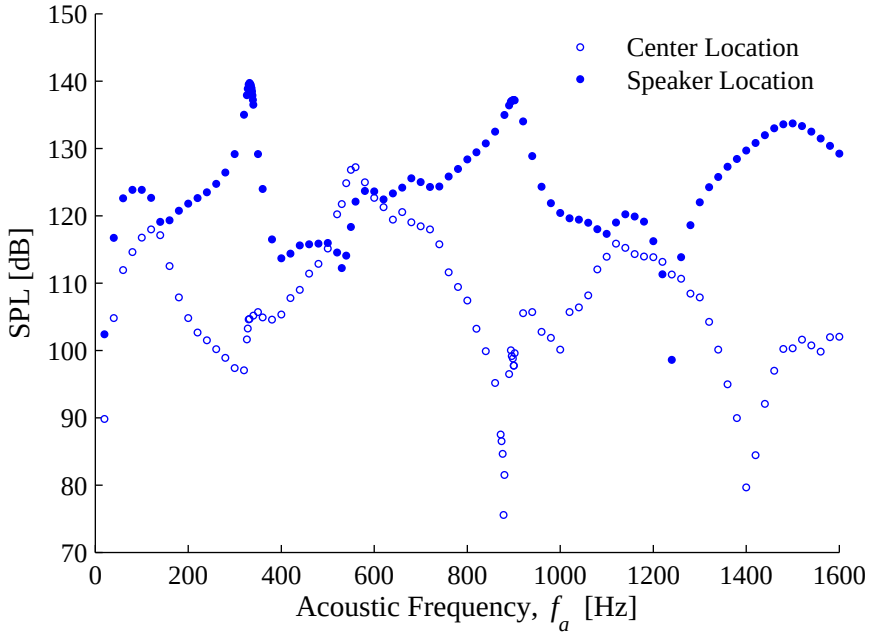


Figure 2.2: Frequency sweep for the speaker-speaker (SS) configuration with 180 degrees relative phase difference between speakers ($\Delta\phi = 180^o$), which situated the PN at the center of the waveguide. The resonant frequencies are shown to occur at 332 Hz, 898 Hz, and 1500 Hz. [37].

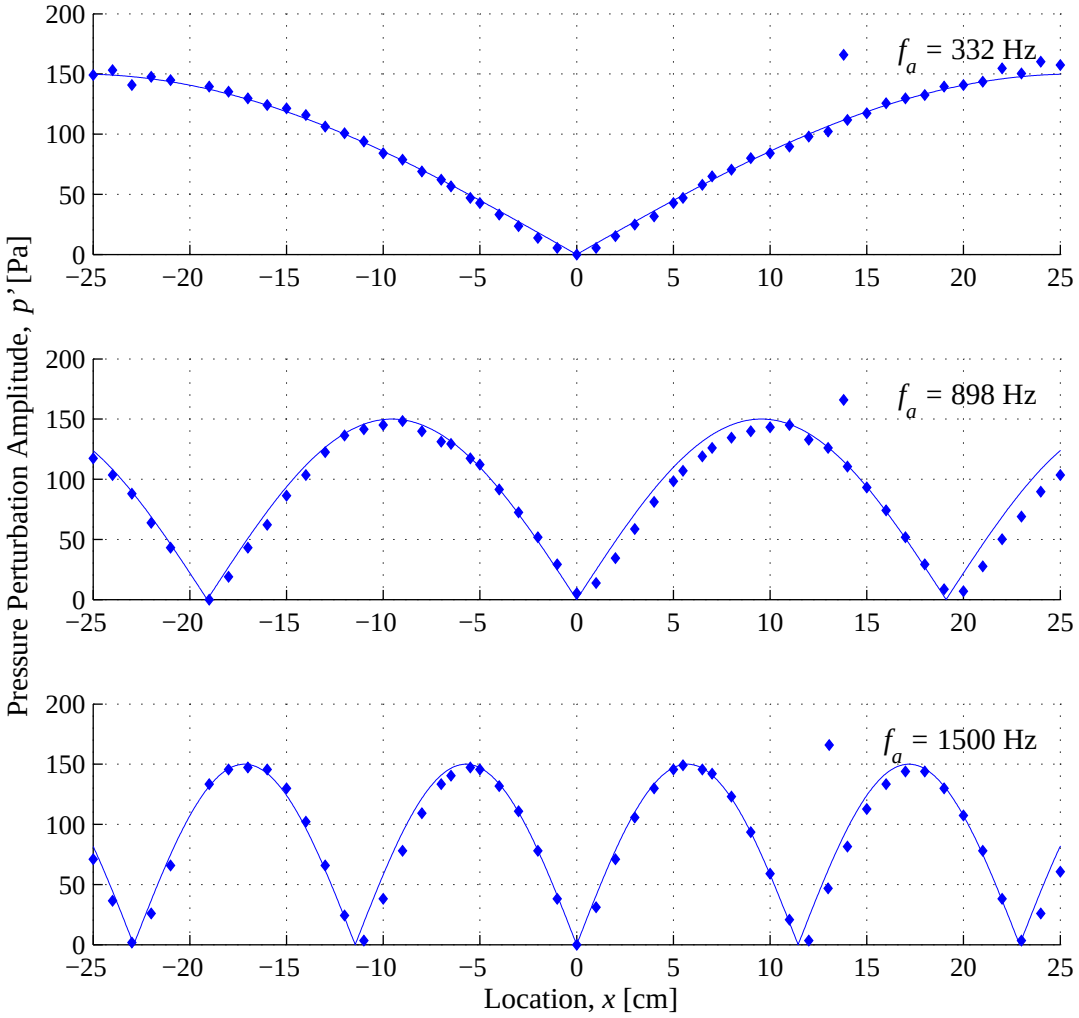


Figure 2.3: Experimental and theoretical pressure perturbation amplitude profiles for speaker-speaker (SS) configurations ($\Delta\phi = 180^o$) at resonant frequencies 332 Hz, 898 Hz, and 1500 Hz. The effective acoustic length between speakers $L$ is approximately 61 cm, while the maximum pressure perturbation amplitude $p'_{max}$ at PAN locations is approximately 150 Pa.

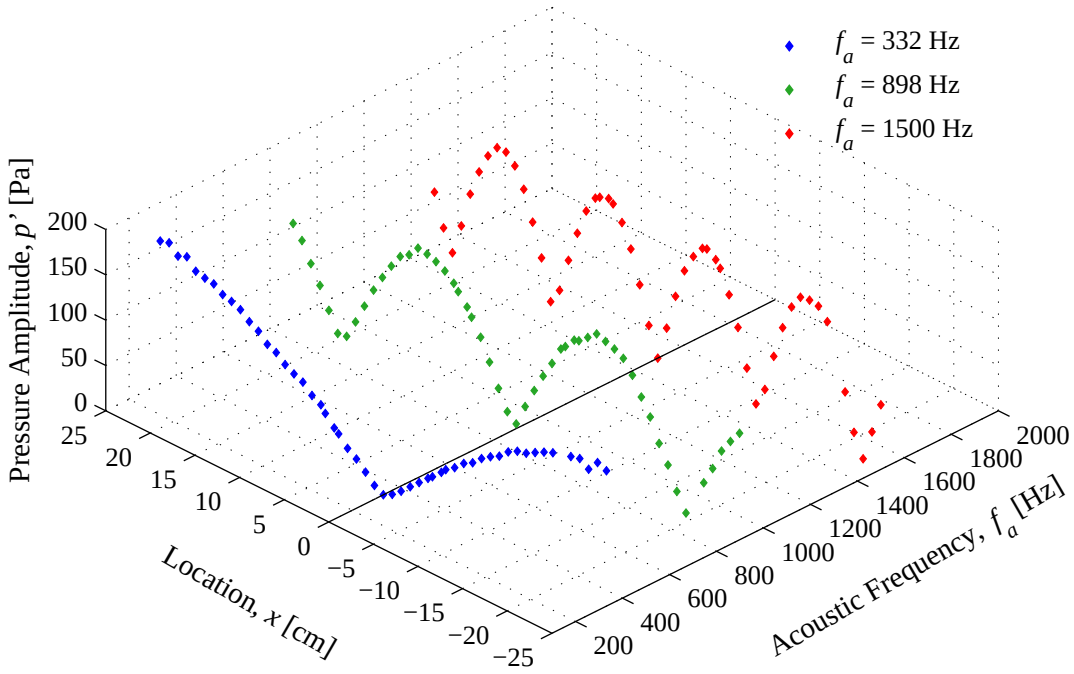


Figure 2.4: Pressure perturbation amplitude profiles for speaker-speaker (SS) configurations ($\Delta\phi = 180^o$) at resonant frequencies 332 Hz, 898 Hz, and 1500 Hz in $p' - x - f_a$ space.

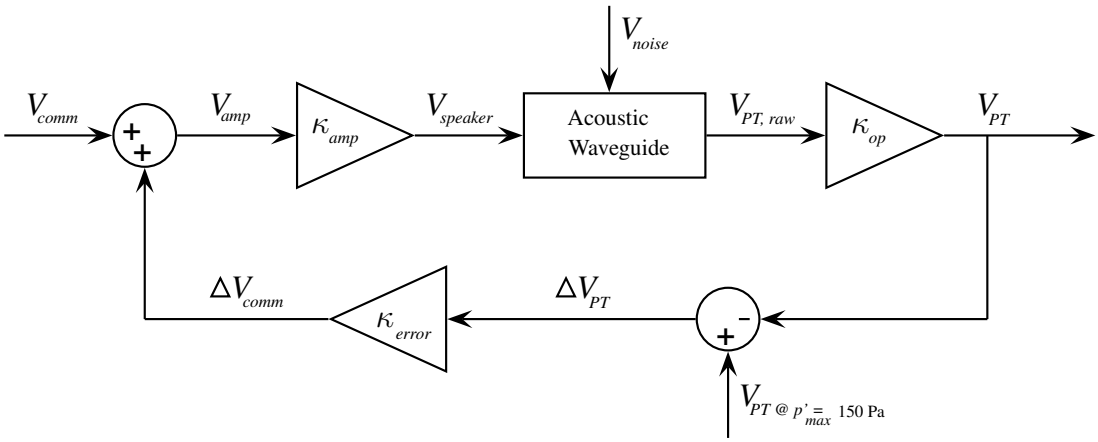


Figure 2.5: Feedback control loop implemented in setting of maximum pressure perturbation amplitude $p'_{max}$.

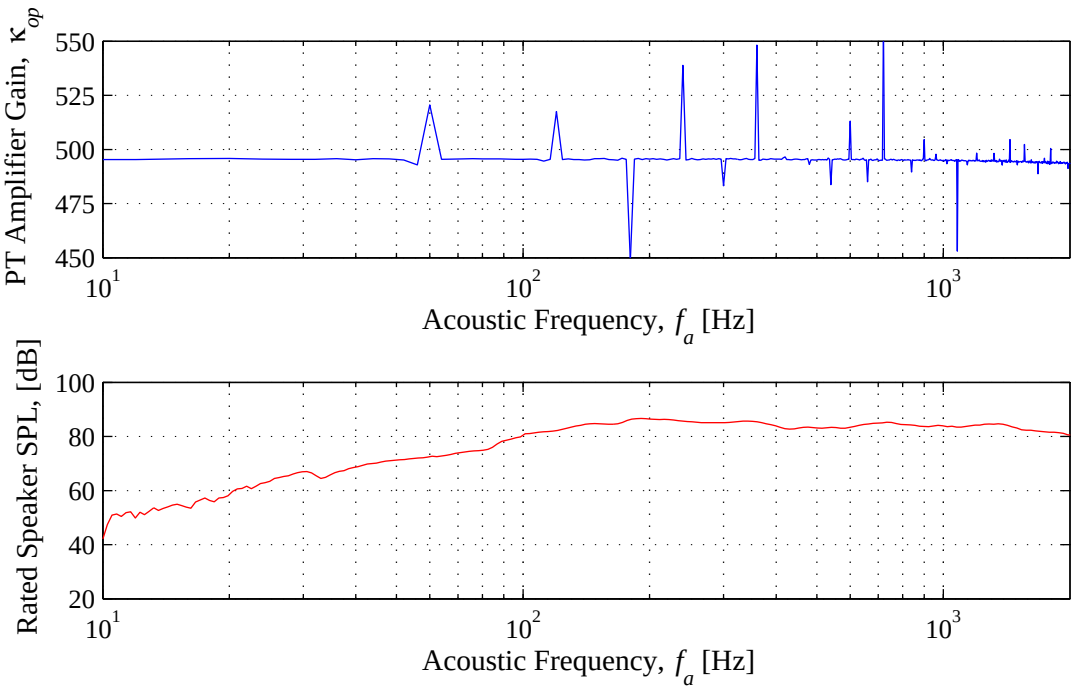


Figure 2.6: Characteristic frequency response for pressure transducer amplifier gain $\kappa_{op}$ and individual speaker acoustic output. The rated speaker SPL profile was collected for $V_{speaker} = 2.83$ V at a sensor distance of 1 m.

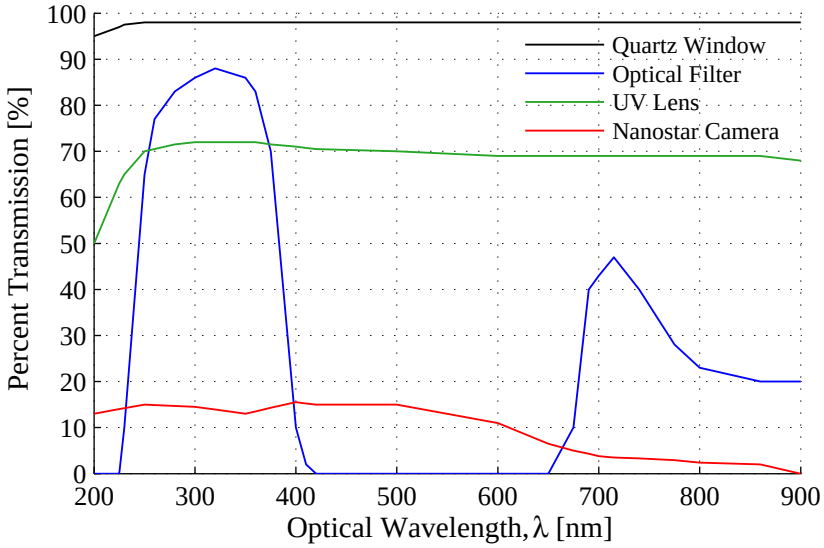


Figure 2.7: Wavelength-dependent percent transmittance of individual constituents to the optical arrangement.

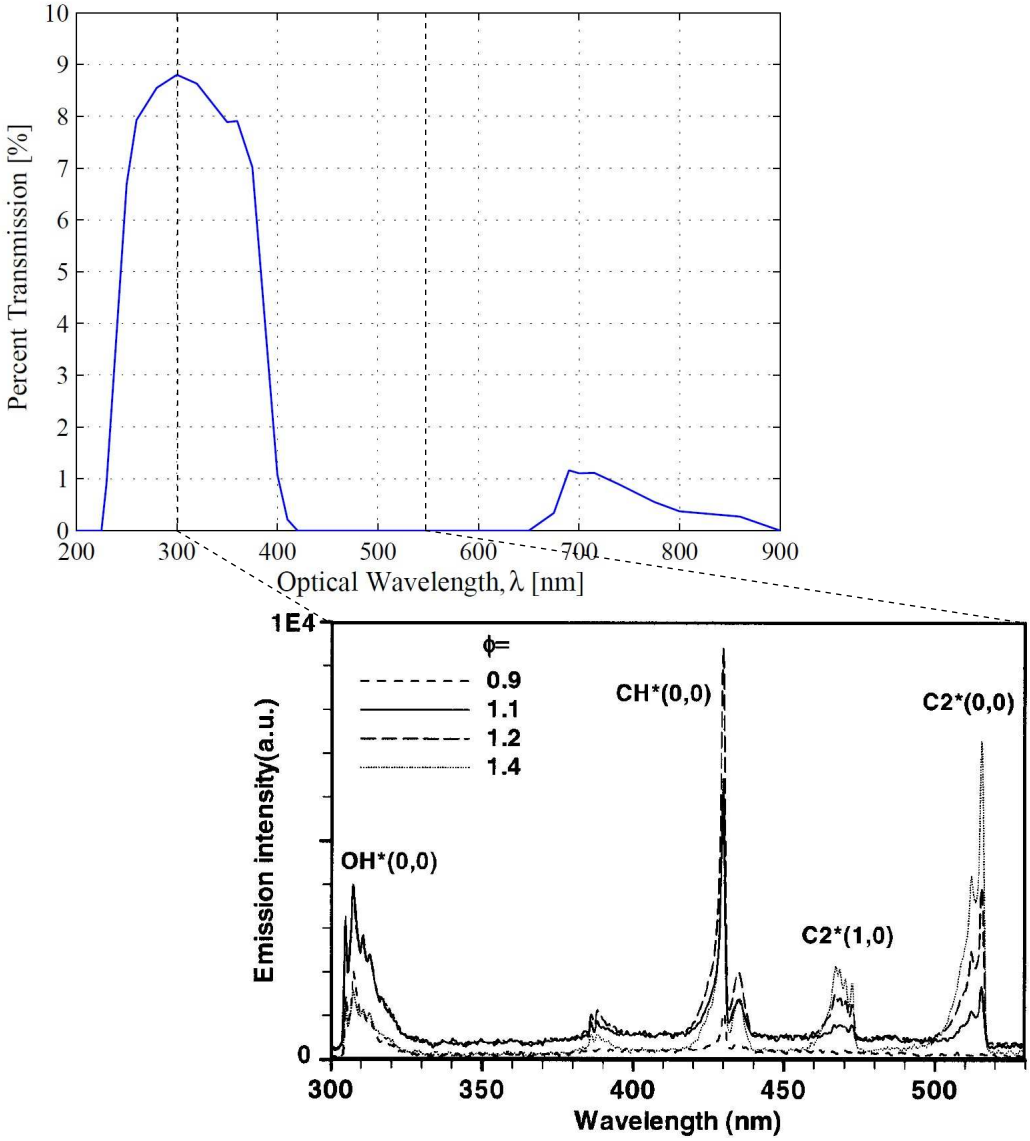


Figure 2.8: Wavelength-dependent percent transmittance of the complete optical arrangement, as compared with experimentally derived wavelengths for radiative deexcitation of the hydroxyl radical (OH*) in methane combustion from Kojima *et al.* [60].

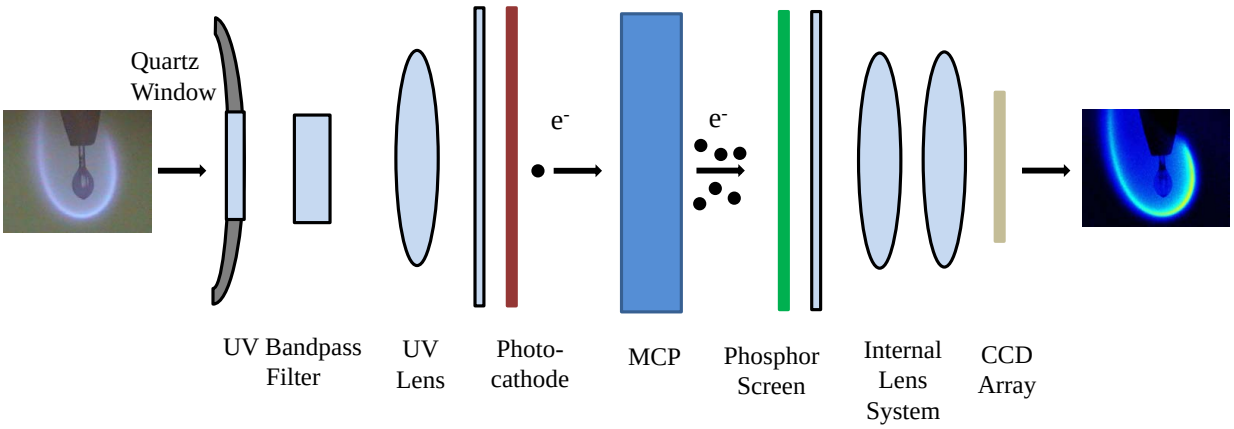


Figure 2.9: OH* chemiluminescence optics and internal components of the Nanostar camera system showing path of light transmission from the burning droplet to the CCD array for image digitization.

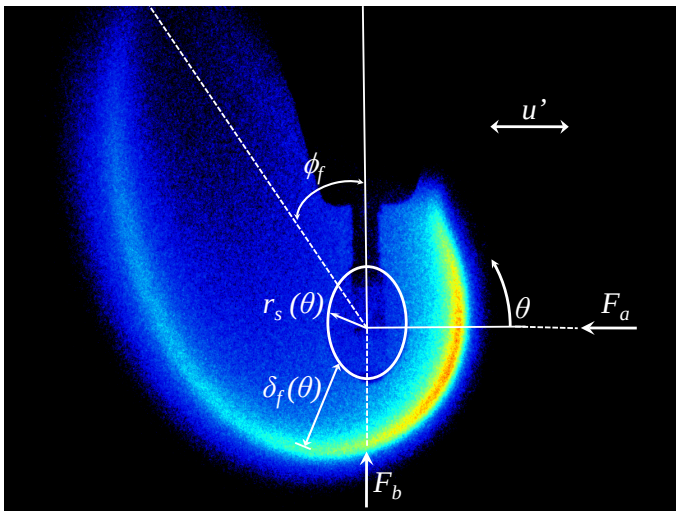


Figure 2.10: Digitized OH* chemiluminescence image of an ethanol flame subject to acoustic forcing. The droplet radius $r_s$ and the flame radius $r_f$ are functions of the angle $\theta$ in the imposed polar coordinate system, whose origin coincides with the center of the droplet. The flame axis aligns itself with the resultant from the interacting acoustic radiation force $F_a$ and buoyancy force $F_b$. Accoustic acceleration $g_a$ may be estimated through the flame deflection angle $\phi_f$.

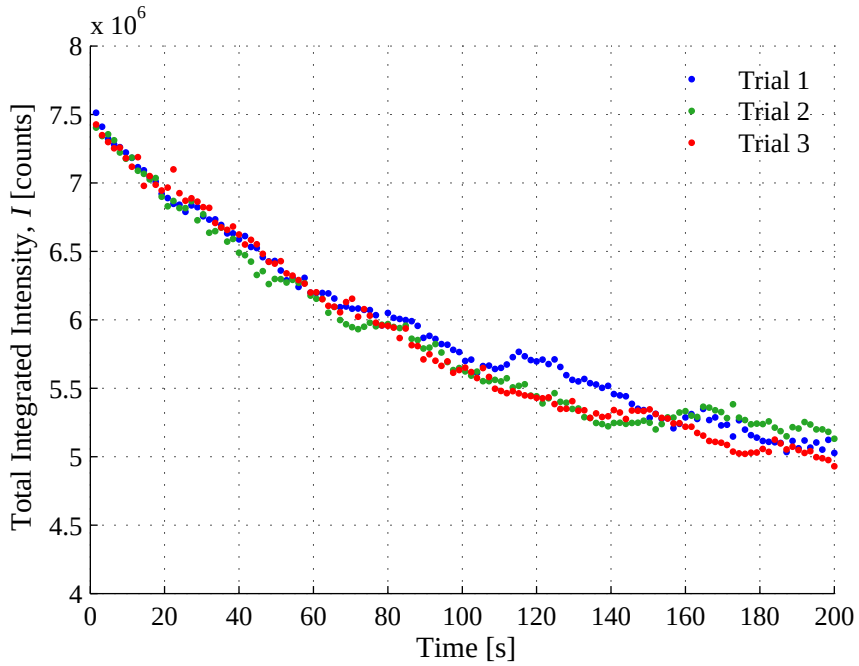


Figure 2.11: Total integrated OH* intensity in ethanol flames over several seconds demonstrating the nonlinear degradation in luminosity over relatively large time periods following ignition.

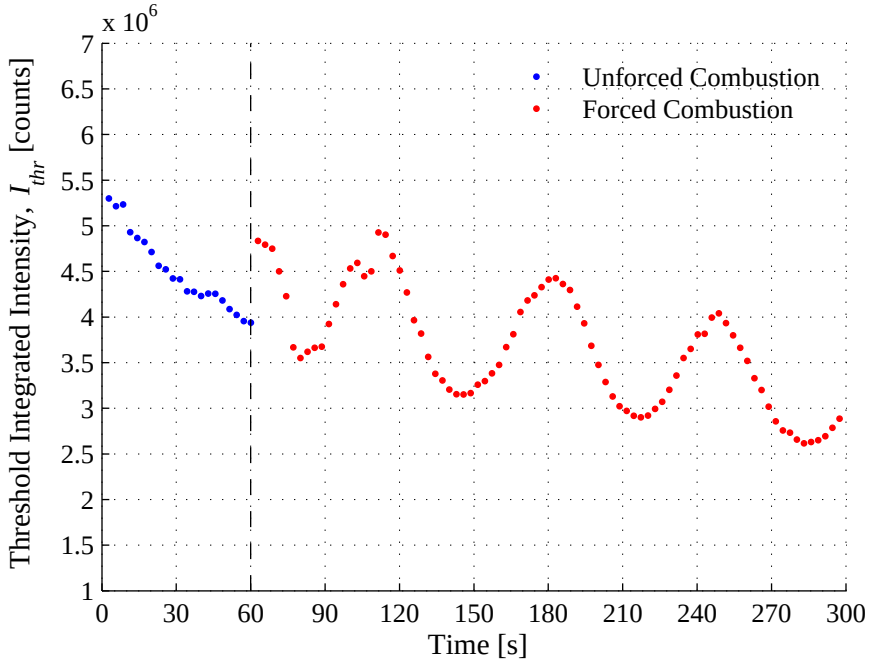


Figure 2.12: Threshold integrated OH* intensity for pixels above a preset luminosity in ethanol flames prior to and following acoustic excitation.

# CHAPTER 3

# Results – Acoustic Waveform Characterization

An investigation into the quality of generated standing wave structures within the acoustic waveguide was conducted prior to the exploration of acoustically coupled droplet combustion. Results of this investigation indicate a complex, frequency-sensitive acoustic interaction between reflected waves at the open boundaries of the waveguide and the standing waves within the loudspeaker assembly. This acoustic behavior manifested itself for some conditions in the improper relative translation of the pressure node (PN) with respect to the stationary fuel droplet in comparison to the translation of the speaker assembly. In addition, the maximum pressure perturbation amplitudes, $p'_{max}$, at pressure antinode (PAN) locations within the waveguide were affected by these boundary interactions. The results in this chapter outline the anomalous observations and their resolution through consideration of inadvertently established quarter-wave tube conditions.

## 3.1 Pressure Node Offset and Pressure Amplitude Degradation

The acoustic behavior intended within the waveguide apparatus initially assumed an isolated acoustic system created by the speaker assembly. Preliminary experiments operated on the premise that waveforms generated within the waveguide were practically independent of alterations in the surrounding environment. Accordingly, the translation of waveforms within the waveguide was thought to occur with direct correspondence to the translation of the speaker assembly itself, as described in Chapter 2. This implied, in other words, that the position of the central PN location relative to the static droplet at the center of the waveguide, given as the waveguide PN location $x$, should always be equal to the physical

displacement between the center of the speaker assembly and the center of the waveguide, or the speaker offset $\Delta x$. This incremental $\Delta x$ could also be ascertained by normalizing the distance between the speaker assembly and the end of the waveguide for which the PN exactly coincides with the waveguide center and then offsetting the assembly from the normalized position.

Irregularities in the PN motion for standing waveforms at lower frequencies and moderate speaker offsets, however, indicated a more complex acoustic interaction between the internal waveform and ambient characteristics. Pressure transducer (PT) diagnostics logged during acoustic excitation in the absence of combustion initially revealed nominal profiles for trials where $\Delta x < 1$ cm. Results of these spatial $p'$ distributions were similar to those presented in Figure 2.3 recorded for $\Delta x = 0$ cm. As $\Delta x$ increased for forcing frequencies of 332 Hz and 898 Hz, displacement of the speaker assembly relative to the droplet position did not coincide with the displacement of the pressure node associated with the standing wave within the waveguide. The translation of the PN location for 1500 Hz, however, remained consistent with the movement of the loudspeakers. The observed discrepancy between the pressure node translation $x$ and the speaker assembly offset $\Delta x$, both relative to the droplet position at the center of the waveguide, are presented for the various forcing frequencies in Figure 3.1.

Furthermore, a decrement in $p'_{max}$ was recorded at the PAN location upon translation of the speaker assembly. This alteration to pressure perturbation amplitudes, which occurred while a constant-amplitude input voltage was administered to each speaker, was particularly sensitive to changes in both $f_a$ and $\Delta x$. In general, acoustic waveforms produced when forcing at all three operational $f_a$ featured augmenting decay in the achievable $p'_{max}$ with increasing absolute magnitudes of $\Delta x$. The observed degree of decay was largely dependent on forcing frequency. The reduction in pressure perturbation amplitude was minor at 332 Hz and 1500 Hz, but $p'_{max}$ relative to $p'_{max}$ at $\Delta x = 0$ cm was halved for $\Delta x > 3$ cm in the 898 Hz flow conditions. A comparison of the spatial $p'$ profiles for different $f_a$ and $\Delta x$ conditions is provided in Figures 3.2, 3.3, and 3.4.

Anomalous PN translocation and degradation of $p'_{max}$ in the experimental configuration limited the forthcoming acoustically coupled combustion experiments. While the erroneous movement of the PN could be remedied through the calibration of correspondent physical speaker placements as shown in Figure 3.1, the deterioration of $p'_{max}$ proved to be more problematic on account of loudspeaker input power restrictions. Flow conditions that demonstrated a severe decay in $p'_{max}$ required input voltages that exceeded the maximum permissible speaker wattage in order to reach acceptable pressure amplitudes. It, thus, became necessary to investigate the mechanisms through which aberrant waveform attributes were propagated and to diagnose an adjustment to the experimental facility in order to alleviate these attributes.

### 3.1.1 Individual Speaker Waveform Measurements

Detailed observations regarding both the misalignment of the PN with respect to the speaker displacement and the attenuation of $p'$ were initially conducted for the most afflicted forcing frequency, 898 Hz. Pressure measurements were collected along the length of the waveguide for a variety of $\Delta x$, including the nominal $\Delta x = 0$ cm location. These trials operated using a single active loudspeaker forced with a fixed input voltage amplitude to isolate the acoustic phenomenon from superposition behavior present in a dual-speaker configuration. The second speaker in the assembly was not removed so as to accurately mimic its impact on the acoustic forcing during typical experimentation, and the effective acoustic length $L =$ 61 cm between the pair was maintained as in all other studies.

First a comparison between the acoustic standing wave structures generated by a single speaker in different locations within the waveguide was performed. To further explore the perceived phenomena, the span between the waveguide and assembly boundaries was manipulated with waveguide extensions. Initial measurements were collected without extensions, as given in Figures 3.5a, 3.6a, and 3.7a. Subsequent $p'$ measurements were recorded with detachable waveguide extensions, whose length $L'$ was initially 30 cm, installed on the ends of the main waveguide for similar $\Delta x$, as given in Figures 3.5, 3.6, and 3.7. These results

suggested the assumption of an isolated acoustic domain within the speaker assembly was invalid. The proximity of the assembly to the waveguide boundaries clearly affected the established $p'_{max}$ for the various $\Delta x$. In fact, the extension configurations at $\Delta x = 5$ cm that featured the most pronounced enclosed air cavity between the back of the active speaker and the respective waveguide boundary, as seen in Figure 3.6a, exhibited dramatic uniform degradation in $p'$ at all locations within the assembly. This implied that planar longitudinal sound waves emitted behind a given speaker also contributed to the final distribution of pressure within the entire waveguide.

Qualitatively, $p'$ diagnostics revealed an important dependence of standing waveform attributes on the relative separation between the speakers and the waveguide boundaries. Pressure amplitude distributions for $\Delta x = 0$ cm with distinct extension arrangements underlined that, though $p'_{max}$ was only slightly afflicted, PN translocation was achieved by simply adjusting the axial location of waveguide boundaries. Moreover, the extension-assembly configurations for $\Delta x$ = -5 cm and $\Delta x = 5$ cm for which the more voluminous of the two enclosed air cavities behind the speaker assembly was asymmetrically lengthened produced degenerate waveforms with no PN structures, illustrated in Figures 3.6b and 3.7c. The remaining flow conditions at $\Delta x$ = -5 cm in Figure 3.7b, in which the extension is placed so as to regularize the two assembly-boundary air cavities, established relevant restoration of $p'$ and accurate translation of the PN relative to its unextended counterpart shown in Figure 3.7a. A similar pressure profile was present in the $\Delta x = 5$ cm arrangement in Figure 3.6c, where the waveguide extension is also oriented so as to equalize the enclosures. Nevertheless, both configurations in Figures 3.7b and 3.6c suffer from impractically low $p'$.

Ultimately the pressure measurements performed allude to a fundamental relationship between the acoustic environment enclosed within the speakers and the geometry of the speaker assembly inside the waveguide. This is likely due to the interaction of omnidirectional sound radiation from each speaker with spurious wave structures reflected by the solid speakers and by the open waveguide boundaries. Any reflection effects present solely between both speakers in the data collected should remain uniform across various operating

conditions on account of the constant effective length $L$ maintained. Such reflections, located exclusively within the cavity between both speakers, should also be independent of the juxtaposition of the waveguide boundary. This contrasts the observations made upon installation of waveguide extensions. But, on the other hand, destructive interference engendered through reflected sound waves from the ends of the waveguide would be notably sensitive to the axial location of the open-air boundary. The half wavelength phase difference ($180^o$) imparted to the reflected longitudinal sound wave at the open boundary renders the location of reflection paramount in determining interference qualities. These considerations, coupled with the $p'$ profiles, insinuate that effects from end-reflected pressure waves likely dominate any other disturbances innate to the waveguide apparatus. This is true when the reflection boundary and the source of incident waves, the loudspeaker, are separated in a manner conducive to quarter-wave tube behavior. Therefore, ascertaining the presence of quarter-wave tube conditions in the experimental facility could explain the anomalous aspects of the acoustic waveform and aid in their reconciliation.

## 3.2 Quarter-Wave Tube Behavior

Quarter-wave tubes employed in combustion and acoustic systems temper noise at undesired frequencies and at the corresponding resonant modes [72, 73]. An open ended quarter-wave tube, whose longitudinal axis coincides with direction of wave propagation and whose length is an integer multiple of one fourth of a characteristic acoustic wavelength $\lambda$, placed at a source of acoustic oscillations with frequency $f_a = c/\lambda$ promotes destructive interference between the original and reflected longitudinal waves. The length of the quarter-wave tube in a given acoustic system is a function of acoustic frequency, speed of sound, and harmonic mode [74], as elaborated in Appendix B. Quarter-wave tube length $l_{\frac{\lambda}{4}}$, outlined for each harmonic mode at each $f_a$ in Table 3.1, is given by

$$l_{\frac{\lambda}{4}} = \frac{\lambda}{4}(2n+1) = \frac{c}{4f_a}(2n+1). \tag{3.1}$$

Calculation of $l_{\frac{\lambda}{4}}$ with Eq. (3.1) by Karagozian [74] at all $f_a$, along with comparison to pertinent geometries of the waveguide and speaker assembly, underlined that anomalies present in the standing waves structures were consequences of unintended quarter-wave tube behavior in the ends of the acoustic apparatus. All experiments employed a constant acoustic length separating the speakers, $L$, equal to 61 cm, while the total waveguide length $L_{WG}$, without extensions, was 90 cm. Thus, the speaker assembly formed air cavities between the back of each speaker and the free air boundaries at the ends of the waveguide. Aligning the assembly with the droplet at the center of the waveguide, as done in the $\Delta x = 0$ cm arrangements, formed symmetric air cavities behind each speaker. When the assembly was shifted with respect to the droplet to conduct a trial at a nonzero waveguide PN location $x$ for a given assembly translation $\Delta x$, the cavities became asymmetric as distances from the ends of each speaker to each end of the waveguide were made incongruous. Each axial cavity span $l$, dictated by the distance from the end of the speaker where sound emanates to the end of the waveguide through the geometric expression $l = \frac{1}{2}(L_{WG} - L) \pm \Delta x$, was a governing parameter of the phenomena observed as either approached the quarter-wave tube length $l_{\frac{\lambda}{4}}$.

Pressure measurements over a range of frequencies and speaker positions revealed that as $l$ approached $l_{\frac{\lambda}{4}}$ associated with the applied $f_a$ on either end of the waveguide, the observed degradation in $p'_{max}$ was exacerbated. This was exceptionally conspicuous in Figure 3.6a, where the almost nonexistent pressure profile generated coincides with measured $l$ of 9.5 cm relative to the active speaker and calculated $l_{\frac{\lambda}{4}}$ of 9.6 cm for the fundamental harmonic mode, $n = 0$. Moreover, acoustic forcing for arrangements with dissimilar $l$ on both ends of the waveguide facility contributed to disagreement between observed and expected PN displacements. Both aberrations in the acoustic field may be interpreted through incident and reflected sound wave interaction. In general, reflection at an open boundary imparts a half wavelength (180°) relative phase difference to any reflected longitudinal sound wave. Superposition of the reflected waves with those produced at the source of acoustic forcing, the speaker in this experiment, yield beneficial or detrimental interference. The nature

of this interference is a function of the magnitude difference in the original and reflected pressure perturbation amplitudes and the relative phase between the interacting waves. Any destructive interference, fostered when the acoustic and reflection sources are separated by $l_{\frac{\lambda}{4}}$, manifests itself through a loss in maximum achievable pressure amplitude in resultant standing waves. Configurations with inherently asymmetric $l$ promote interactions between disproportionate reflected acoustic waves from both ends of the waveguide in the vicinity of the droplet within the loudspeaker assembly, resulting in a disparity between the motion of the assembly and that of the PN and PAN.

The evident role of quarter-wave tube behavior led to an updated operating procedure accounting for the observed phenomena interdependently through use of fitted waveguide extensions of various lengths $L'$. Translation of the PN was regularized by addition of fitted extensions that equalized $l$ on both ends of the apparatus and avoided $l_{\frac{\lambda}{4}}$ geometries. Each extension length $L'$ depended on the speaker assembly displacement $\Delta x$ implemented. Any inevitable attenuation remaining after acoustic extensions were installed was resolved by application of increased input voltage to each speaker within the rated wattage limitations. Tables 3.2, 3.3, and 3.4 outline the change in observed pressure data and translation of $x$ relative to prescribed $\Delta x$ before and after the attachment of waveguide extensions (but without voltage modification), along with a rectified schematic of the apparatus.

Table 3.1: Quarter-Wave Tube Lengths for Resonant Forcing Frequencies

| $f_a = 332$ Hz | | $f_a = 898$ Hz | | $f_a = 1500$ Hz | |
|---|---|---|---|---|---|
| $n$ | $l_{\frac{\lambda}{4}}$ [cm] | $n$ | $l_{\frac{\lambda}{4}}$ [cm] | $n$ | $l_{\frac{\lambda}{4}}$ [cm] |
| 0 | 26 | 0 | 9.6 | 0 | 5.7 |
| 1 | 77 | 1 | 29 | 1 | 17 |
| - | - | 2 | 48 | 2 | 28 |

Table 3.2: Speaker Assembly and PN Translation without and with Fitted Extensions, $f_a = 332$ Hz

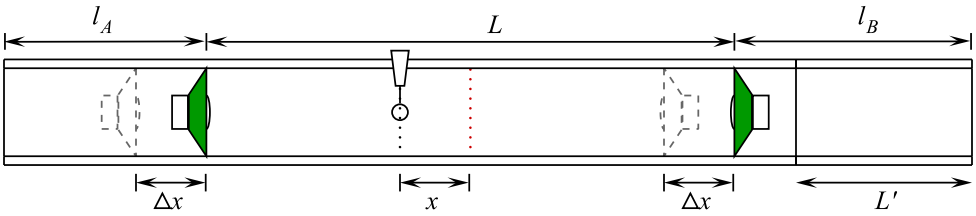


| Without Fitted Extensions | | | | | |
|---|---|---|---|---|---|
| $x$ [cm] | $\Delta x$ [cm] | $L'$ [cm] | $l_A$ [cm] | $l_B$ [cm] | $p'_{max}/p'_{max\|\Delta x=0\text{cm}}$ |
| 0 | 0 | 0 | 14.5 | 14.5 | 1 |
| 1 | 1.4 | 0 | 13.1 | 15.9 | 0.99 |
| 2 | 3.1 | 0 | 11.4 | 17.6 | 0.98 |
| 3 | 4.6 | 0 | 9.9 | 19.1 | 0.89 |
| 4 | 6.6 | 0 | 7.9 | 21.1 | 0.68 |
| With Fitted Extensions | | | | | |
| $x$ [cm] | $\Delta x$ [cm] | $L'$ [cm] | $l_A$ [cm] | $l_B$ [cm] | $p'_{max}/p'_{max\|\Delta x=0\text{cm}}$ |
| 0 | 0 | 0 | 14.5 | 14.5 | 1 |
| 1 | 1 | 2 | 15.5 | 15.5 | 0.98 |
| 2 | 1.9 | 4 | 16.4 | 16.6 | 0.79 |
| 3 | 3 | 6 | 17.5 | 17.5 | 0.58 |
| 4 | 4.1 | 8 | 18.6 | 18.4 | 0.42 |
| 5 | 5.1 | 10 | 19.6 | 19.4 | 0.36 |

Table 3.3: Speaker Assembly and PN Translation without and with Fitted Extensions, $f_a$ = 898 Hz

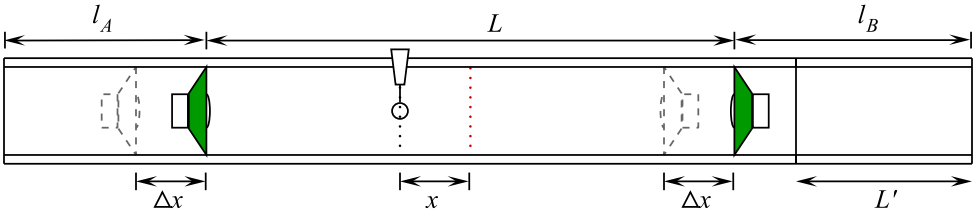


| Without Fitted Extensions | | | | | |
|---|---|---|---|---|---|
| $x$ [cm] | $\Delta x$ [cm] | $L'$ [cm] | $l_A$ [cm] | $l_B$ [cm] | $p'_{max}/p'_{max\|\Delta x=0\text{cm}}$ |
| 0 | 0 | 0 | 14.5 | 14.5 | 1 |
| 1 | 1.7 | 0 | 12.8 | 16.2 | 0.84 |
| 2 | 3.1 | 0 | 11.4 | 17.6 | 0.64 |
| 3 | 4.3 | 0 | 10.2 | 18.8 | 0.51 |
| 4 | 5.4 | 0 | 9.1 | 19.9 | 0.42 |
| 5 | 6.2 | 0 | 8.3 | 20.7 | 0.36 |
| With Fitted Extensions | | | | | |
| $x$ [cm] | $\Delta x$ [cm] | $L'$ [cm] | $l_A$ [cm] | $l_B$ [cm] | $p'_{max}/p'_{max\|\Delta x=0\text{cm}}$ |
| 0 | 0 | 0 | 14.5 | 14.5 | 1 |
| 1 | 0.9 | 2 | 15.4 | 15.6 | 1.13 |
| 2 | 2.1 | 4 | 16.6 | 16.4 | 1.11 |
| 3 | 3.1 | 6 | 17.6 | 17.4 | 0.79 |
| 4 | 4 | 8 | 18.5 | 18.5 | 0.49 |
| 5 | 5 | 10 | 19.5 | 19.5 | 0.34 |

Table 3.4: Speaker Assembly and PN Translation without and with Fitted Extensions, $f_a = 1500$ Hz

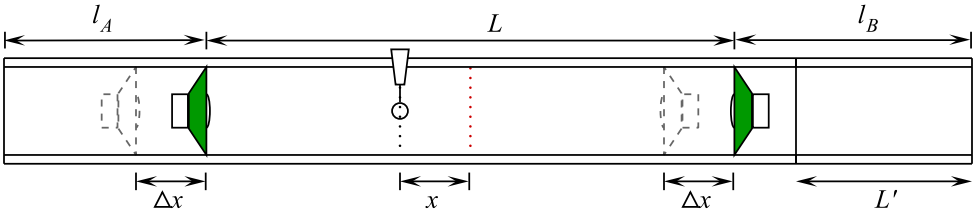


| Without Fitted Extensions | | | | | |
|---|---|---|---|---|---|
| $x$ [cm] | $\Delta x$ [cm] | $L'$ [cm] | $l_A$ [cm] | $l_B$ [cm] | $p'_{max}/p'_{max\|\Delta x=0\text{cm}}$ |
| 0 | 0 | 0 | 14.5 | 14.5 | 1 |
| 1 | 1 | 0 | 13.5 | 15.5 | 1 |
| 2 | 2 | 0 | 12.5 | 16.5 | 1 |
| 3 | 3 | 0 | 11.5 | 17.5 | 0.98 |
| 4 | 4 | 0 | 10.5 | 18.5 | 0.96 |
| 5 | 5 | 0 | 9.5 | 19.5 | 0.95 |
| With Fitted Extensions | | | | | |
| $x$ [cm] | $\Delta x$ [cm] | $L'$ [cm] | $l_A$ [cm] | $l_B$ [cm] | $p'_{max}/p'_{max\|\Delta x=0\text{cm}}$ |
| 0 | 0 | 0 | 14.5 | 14.5 | 1 |
| 1 | 1 | 2 | 15.5 | 15.5 | 1.02 |
| 2 | 2 | 4 | 16.5 | 16.5 | 1.02 |
| 3 | 3 | 6 | 17.5 | 17.5 | 1.02 |
| 4 | 4 | 8 | 18.5 | 18.5 | 1.04 |
| 5 | 5 | 10 | 19.5 | 19.5 | 1.04 |

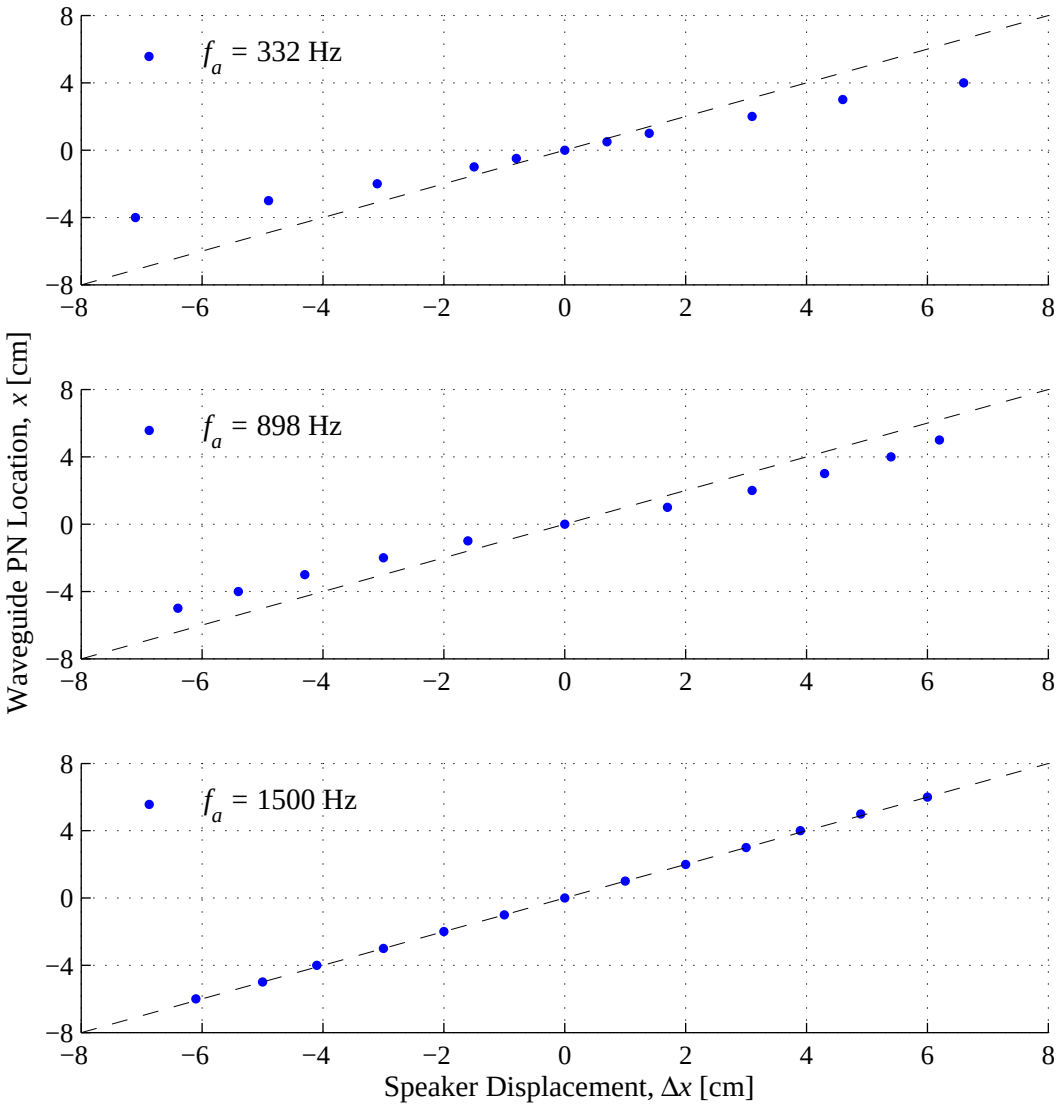


Figure 3.1: Translation of the PN location $x$ with respect to movement of speaker assembly $\Delta x$ for 332 Hz, 898 Hz, and 1500 Hz. The disagreement between $x$ and $\Delta x$ is progressively improved with increasing $f_a$.

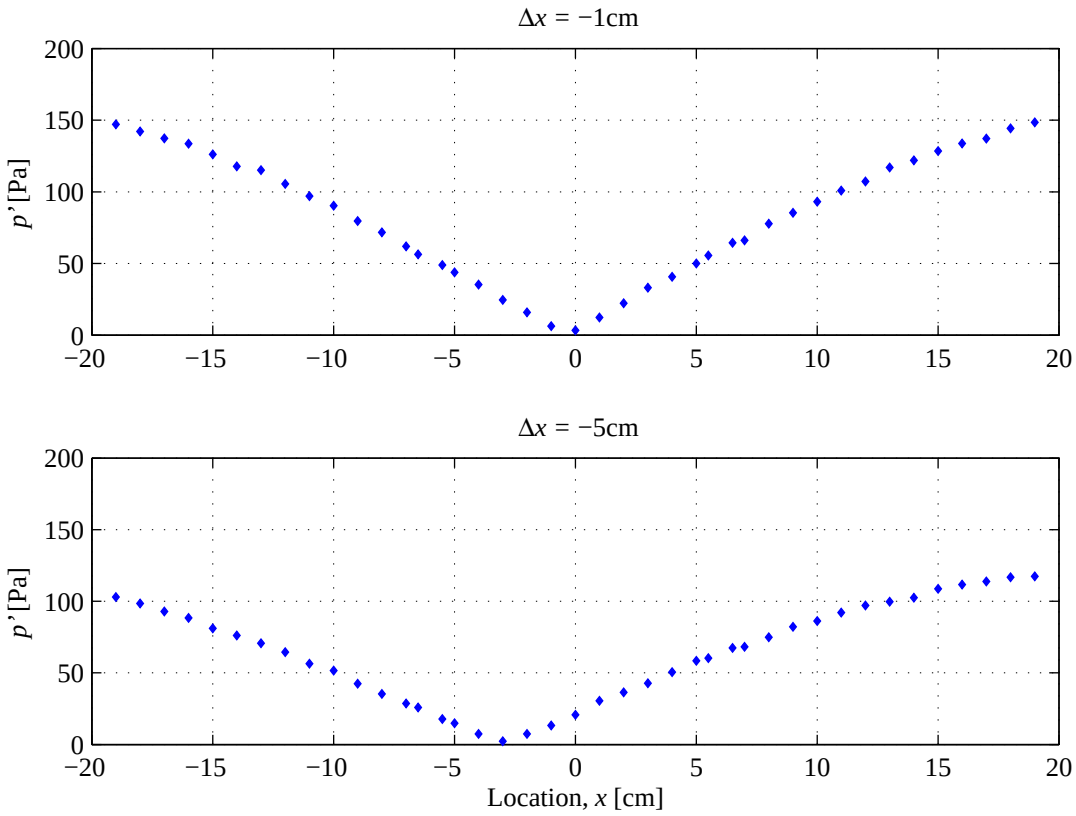


Figure 3.2: Pressure perturbation amplitude profile for distinct speaker assembly displacements at $f_a = 332$ Hz. Significant degradation in $p'$ and inconsistent translation of the PN location are evident.

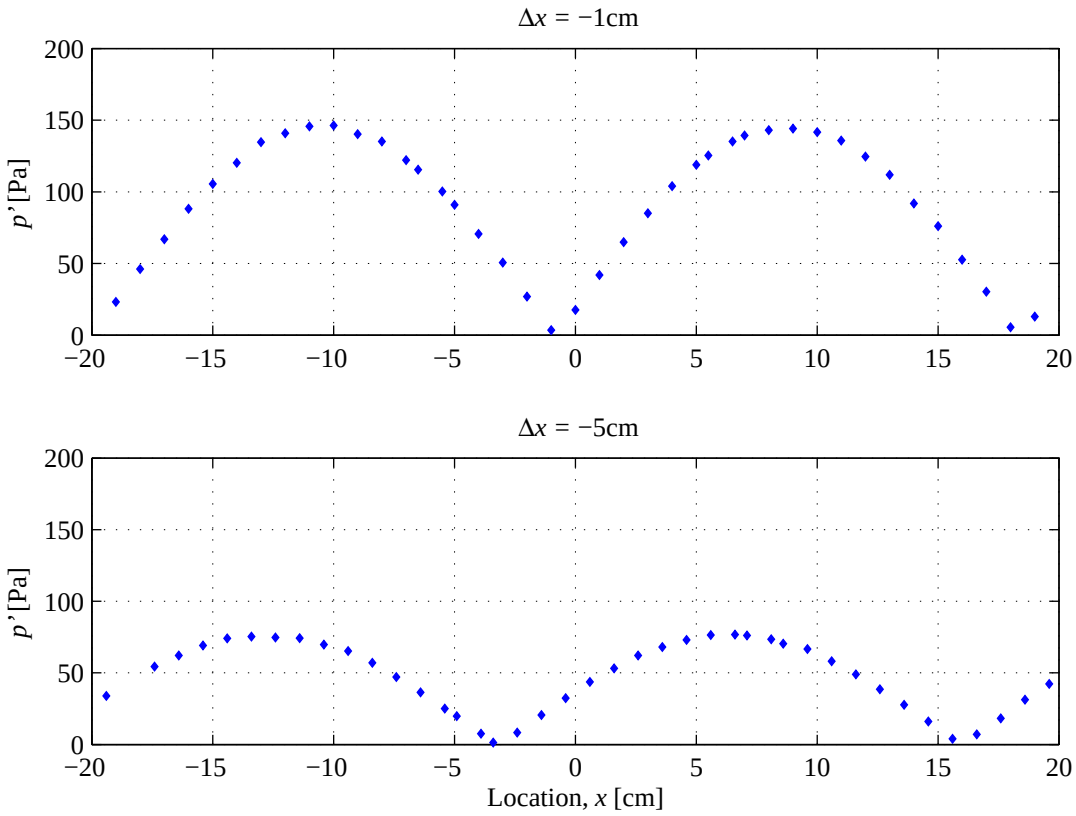


Figure 3.3: Pressure perturbation amplitude profile for distinct speaker assembly displacements at $f_a = 898$ Hz. Significant degradation in $p'$ and inconsistent translation of the PN location are evident.

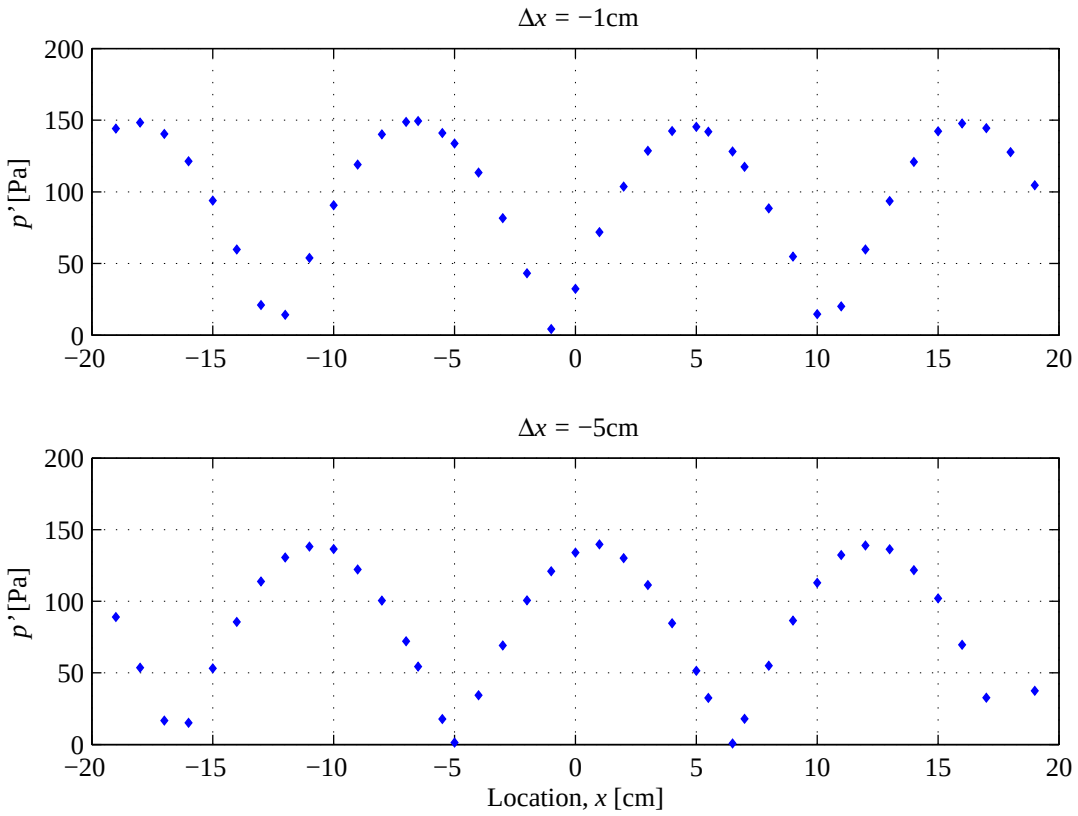


Figure 3.4: Pressure perturbation amplitude profile for distinct speaker assembly displacements at $f_a = 1500$ Hz. Insignificant degradation in $p'$ and consistent translation of the PN location are evident.

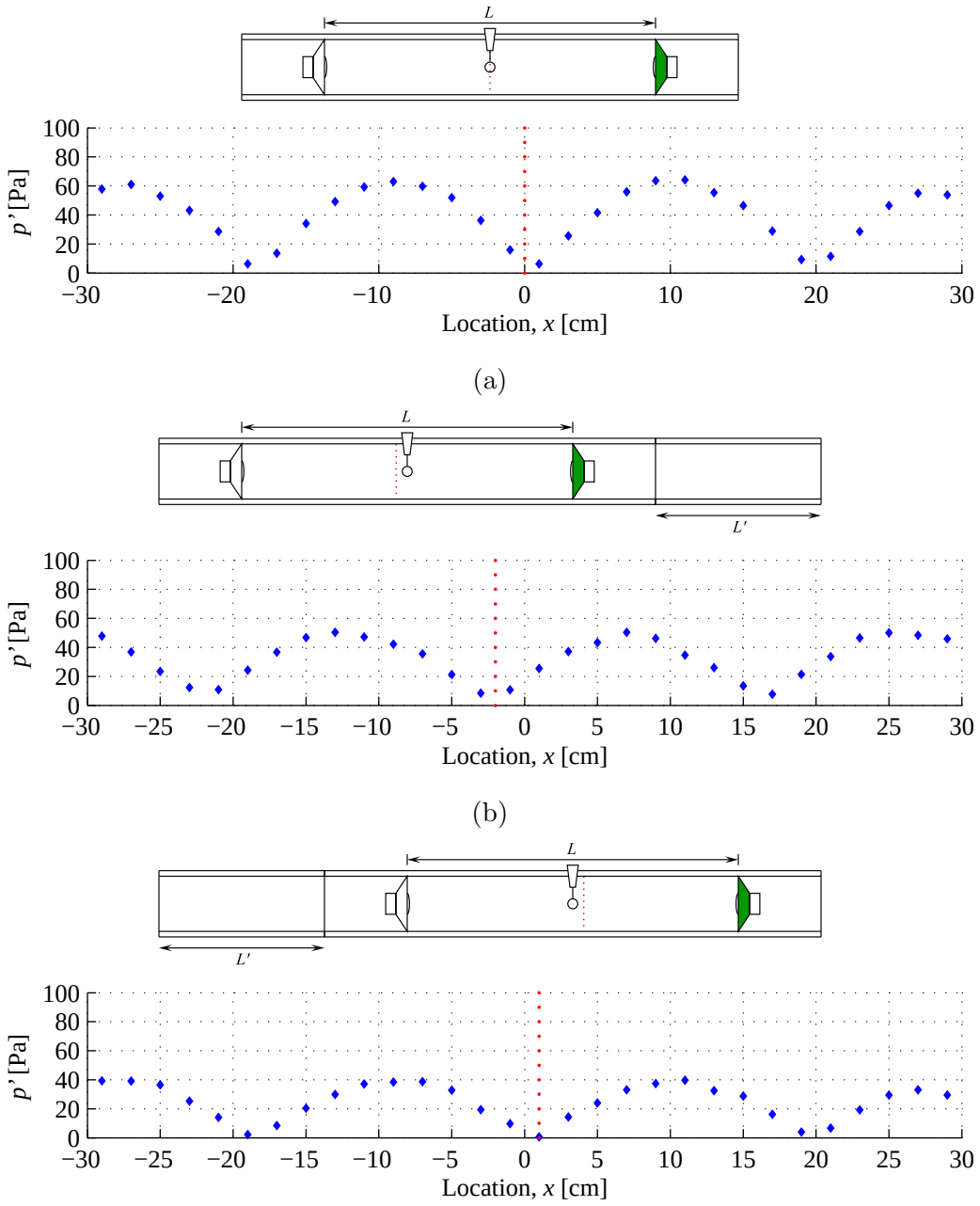


Figure 3.5: Influence of waveguide extension juxtaposition on translation of the PN location for a constant speaker assembly offset $\Delta x = 0$ cm at $f_a = 898$ Hz.

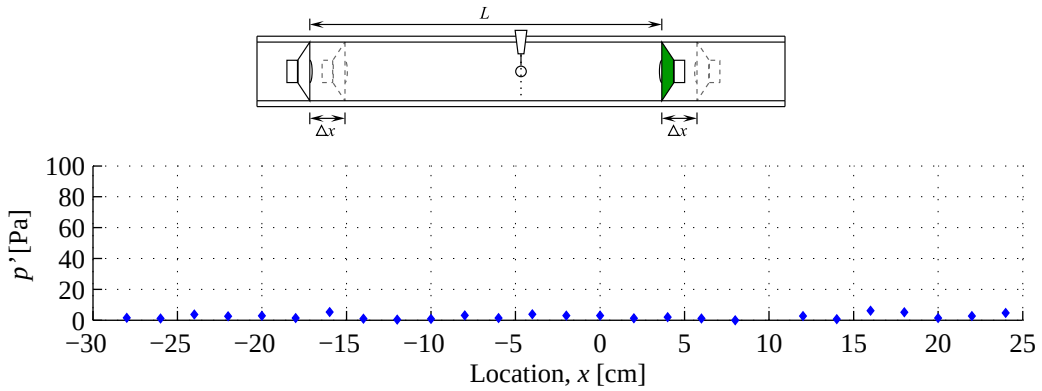


(a)

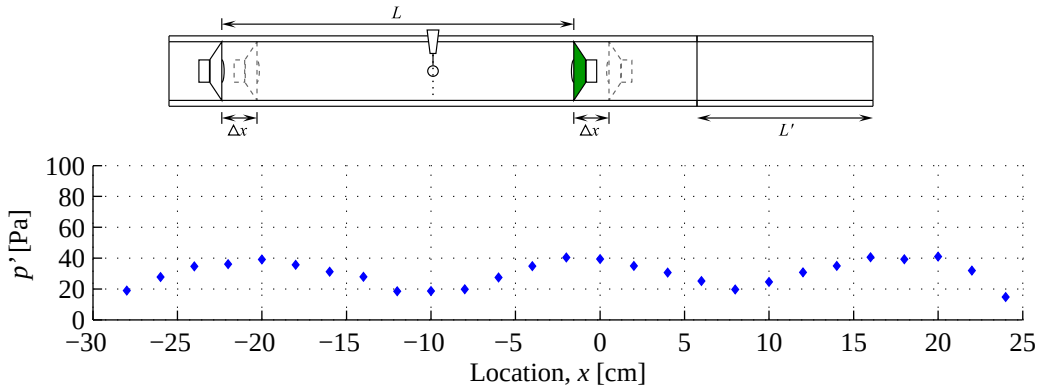


(b)

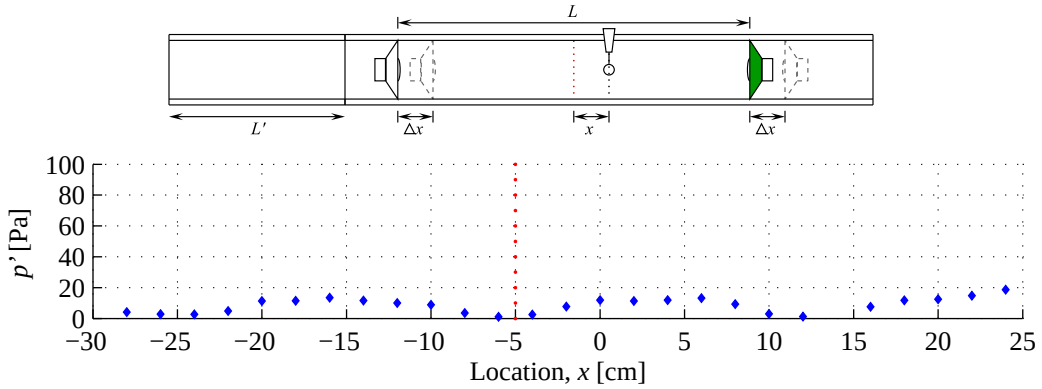


(c)

Figure 3.6: Influence of waveguide extension juxtaposition on translation of the PN location for a constant speaker assembly offset $\Delta x = 5$ cm at $f_a = 898$ Hz.

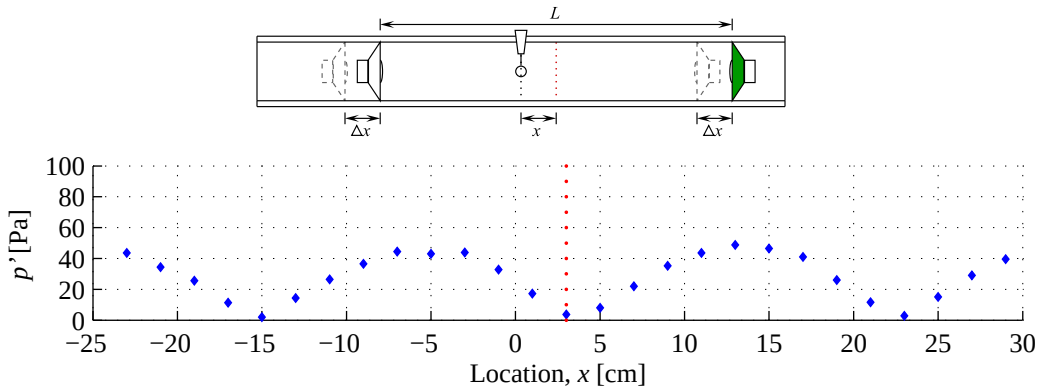


(a)

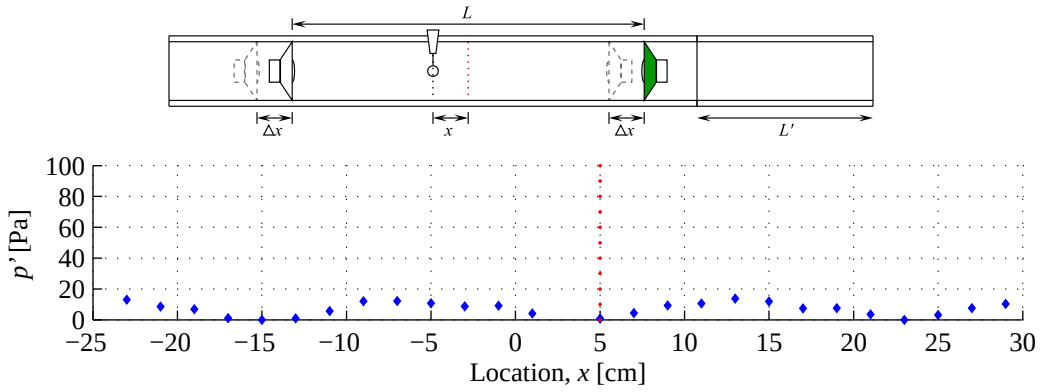


(b)

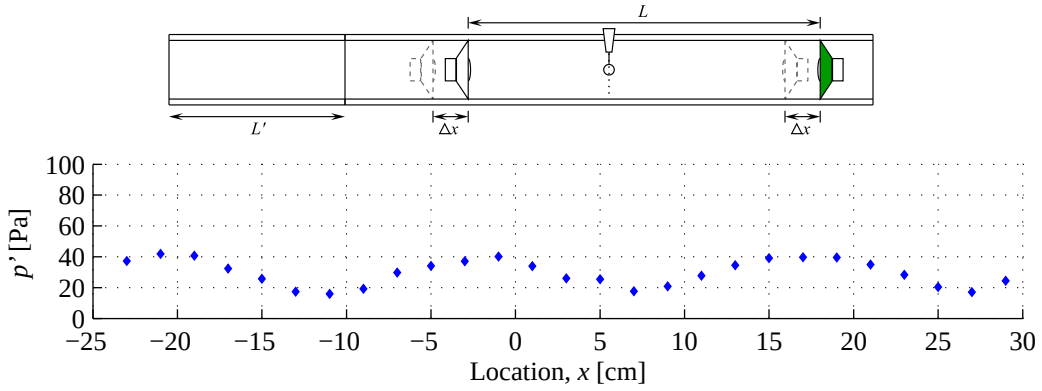


(c)

Figure 3.7: Influence of waveguide extension juxtaposition on translation of the PN location for a constant speaker assembly offset $\Delta x$ = -5 cm at $f_a$ = 898 Hz.

# CHAPTER 4

# Results – Acoustically Coupled Droplet Combustion

Results of this experimental study extend the findings of Wegener [37] pertaining to the coupling of droplet combustion with the imposed acoustic disturbances. These results substantiate the departure from quantitative predictions of the acoustic radiation force model for burning spheres within standing acoustic waves proposed by Tanabe *et al.* [41–43]. To compare spatial relationships across different $f_a$, experimentally derived values of the burning rate constant $K$, acoustic acceleration $g_a$, flame standoff distance $\delta_f$, and Rayleigh index $G$ collected in the presence of acoustic forcing are graphed with respect to $x$, the displacement between the central PN and the droplet, in fractions of the acoustic forcing wavelength $\lambda$.

## 4.1 Burning Rate Constant

Baseline burning rate constants ($K$) for quiescent, unforced burning fuel droplets were carried out prior to the evaluation of acoustically forced $K$. Chemiluminescence images corresponding to unforced combustion for the four fuels explored are presented in Figure 4.1. These UV filtered images masked the visible-spectrum luminosities inherent to each fuel. The combustion of alcohol fuels, characterized by oxygenated intermediaries, radiated chiefly blue and violet light of shorter optical wavelength. Conversely, prevalence of $C_2$ and CH radicals and soot in the burning of hydrocarbon fuels produced chemiluminescence in longer, yellow and orange wavelengths. Gravity-induced buoyancy and surface tension imparted oblong, elliptical geometries within the flame structure and the suspended droplet, respectively.

Baseline values of the burning rate constant $K$ of the unforced burning droplets in nor-

mal gravity for all four fuels investigated in this study are listed in Table 4.1 alongside reference burning rate constants available in the literature. The baseline $K$ were computed using footage gathered after allowing for the same luminous stabilization time offset from ignition imparted in the recording of forced droplet combustion. While this enables a proper comparison between parameters in quiescent and acoustically perturbed environments, these measured $K$ are susceptible to the effects of accumulating hot gases in the immediate vicinity of the reaction zone. Wegener [37] documented a decrease in measured burning rate constant over extended time intervals following ignition for unforced flames. Attenuated $K$ values were attributed to heightened product mass fractions confined to the droplet location. This aggregation was absent from acoustically resonant flow conditions due to imposed forced convection. In order to minimize the influence of product buildup on the calculation of burning rate for unforced burning droplets, baseline $K$ were evaluated using the first 15 images in each combustion footage set. Externalities impacting the burning rate, including the distance between the end of the capillary and the protective copper shroud, were maintained between trials. Moreover, the influence of water absorption on $K$ in the combustion of alcohol fuels was neglected due to continuous fuel replenishment via the borosilicate glass capillary during experimentation.

Burning rate constants were assessed for forced burning droplets placed at various locations with respect to the central PN of the applied standing acoustic waves. These waveforms, created through out-of-phase ($\Delta\phi = 180°$) speaker operation, were properly translated through movement of the speaker assembly after the installation of appropriate waveguide extensions tabulated in Tables 3.2, 3.3, and 3.4. Explorations of droplet combustion in acoustically perturbed environments have demonstrated elevated magnitudes of $K$ relative to baseline counterparts [36, 37, 40–42, 46, 48]. The forced $K$ shown here were calculated for $f_a = 332$ Hz, 898 Hz, and 1500 Hz at distinct locations $x$ within the waveguide. These burning rate constants, along with pressure perturbations, experimental and theoretical acoustic accelerations, and Rayleigh indices discussed in forthcoming sections, are presented as functions of wavelength-scaled location relative to the PN positions in Figures 4.2 through 4.13.

Forced $K$ values observed in flow conditions for the alcohol and hydrocarbon fuels were consistently greater than baseline quantities. This was particularly evident for burning droplets in the immediate vicinity of PN positions at all $f_a$. Experiments conducted in the vicinity of the PN produced forced $K$ values up to 25% higher than their unforced counterparts. In contrast, the difference between unforced and forced burning rate constants when the droplet was situated at PAN locations ($x = \pm\lambda/4$) was almost negligible, in agreement with the documented behavior in prior work [36, 37, 40–42, 46, 48]. Uniformly heightened magnitudes of forced $K$ appeared at $f_a$ with comparatively large $\lambda$, where modest waveform displacements hardly affected the relative positions of the PAN and PN with respect to the burning droplet. The highest forcing frequency, on the other hand, demonstrated significant variations in burning rate because results extended from the central PN into the negative and positive PAN locations. This perceived amplification in $K$ was ascribed to increased fuel mass transfer through evaporation fostered by the decreased flame standoff distances and steeper temperature gradients present in fuel droplets burning near the PN.

## 4.2 Acoustic Acceleration

The influence of acoustic forcing on the burning droplet system was prevalently distinguished by the resulting deflection of the flame front and plume. These flame deflections were independent of the lateral oscillations of the flame front occurring at microscale time periods directly associated with each applied $f_a$. In the presence of an acoustic standing wave, the magnitude and direction of flame deflection were functions of the spatial positioning of the droplet system relative to established PN and PAN locations, as illustrated in Figure 4.14. Experimental acoustic acceleration values estimated per the procedure validated by Teshome *et al.* [47–49] and employed by Wegener [37] were compared quantitatively to predicted $g_a$ formulated through the acoustic radiation force model posed by Tanabe *et al.* [41].

The theoretical acoustic acceleration engendered through application of standing acoustic

waveforms proposed by Tanabe *et al.* [43] is expressed as the following

$$F_a = (\rho_p - \rho_o)\mathcal{V}\left[\pm 4\alpha\left(\frac{\mathcal{I}}{z_a}\right)\left(\frac{2\pi f_a}{c}\right)\sin\left(\frac{2\pi x}{\lambda}\right)\cos\left(\frac{2\pi x}{\lambda}\right)\right]. \tag{4.1}$$

Here, $\mathcal{I}$ is the acoustic intensity of the established waveform, a function of the maximum sound pressure level taken at the PAN position, and $z_a = \rho c$, the acoustic impedance, is represented as the product of medium density and speed of sound. The bracketed term is an equivalent expanded form of the acoustic acceleration, $g_a = \alpha\frac{\partial\overline{u'^2}}{\partial x}$. The density correction factor $\alpha$ given in Eq. (1.3) is substituted as one in subsequent analyses. The sign of the bracketed portion of $g_a$ in Eq. (4.1) depends on the juxtaposition of the pressure node and antinode in a given configuration: a minus sign is used when a PN (or VAN) is installed at $x = 0$ cm, whereas a positive sign appears when a PAN (or VN) is situated here. Through examination of Eq. (4.1), displacement to the right ($x > 0$ cm) or left ($x < 0$ cm) relative to a PN structure generates a finite net force on the "sphere" of hot combustion byproducts, with density $\rho_p$ and volume $\mathcal{V}$ in an environment at ambient density $\rho_o$, representative of the droplet flame. This sign convention implies that deflected flames are oriented away from PN positions and toward PAN positions, opposite the direction of $F_a$. These phenomena are cited by Tanabe *et al.* [41–43] for *n*-decane droplets, by Dattarajan *et al.* [36, 44] for methanol droplets in microgravity, and by Rodriguez, Teshome, and Wegener [37, 45–49] for a host of fuels similar to those in this study in normal gravity.

Experimental acoustic accelerations related to the acoustic radiation force $F_a$ in Eq. (4.1) were determined for an array of acoustic forcing configurations. Teshome [47–49] and Wegener [37] exercised similar quantitative estimation of $g_a$ values through comparisons between acoustically excited flame geometries and ubiquitous flame behavior solely under the influence of standard gravitational acceleration $g_o$. In the absence of forcing, the flame plume surrounding the fuel droplet orients itself vertically in opposition to normal gravity through buoyancy. Imposition of acoustic disturbances in the form of standing waves generates an acoustic acceleration in the horizontal direction, parallel to the orientation of sound propagation. The resultant deflection of the flame plume, then, is interpreted as the combined effect of the acoustic radiation force $F_a$ and the buoyancy force $F_b$. This homologous formulation

of $F_a$ with respect to $F_b$ present in normal gravity permitted the extraction of experimental acoustic acceleration $g_{a,\text{exp}}$ through visual interrogation of $\phi_f$. The flame deflection angle $\phi_f$ measured between the vertical and the aligned flame axes, as portrayed in Figure 2.10, was utilized in calculating the experimental acoustic acceleration via $g_{a,\text{exp}} = g_o \tan(\phi_f)$. The acoustic accelerations for fuels and forcing conditions explored are given in conjunction with corresponding theoretical counterparts found through Eq. (4.1), pressure perturbations, forced burning rate constants, and Rayleigh indices in Figures 4.2 through 4.13.

While the calculated magnitudes of $g_{a,\text{exp}}$ and $g_{a,\text{th}}$ were quantitatively dissimilar, the qualitative implications of the Tanabe acoustic radiation force theory were verified experimentally. The theoretical expression of $F_a$ in Eq. (4.1) implies a sign change in $g_a$ for $x = \pm n\lambda/4$ given integer values of $n$, including $n = 0$. Hence, the model predicts a change in the flame orientation depending on the droplet location relative to the centrally situated PN. This flame "switch" behavior was confirmed for all flow conditions tested, as exemplified in the $g_a$ quantification in Figures 4.2 through 4.13 and in Figure 4.14 for burning ethanol droplets forced at $f_a = 1500$ Hz. Regarding the calculated acoustic acceleration magnitudes, however, a pronounced disagreement between $g_{a,\text{exp}}$ and $g_{a,\text{th}}$ was observed in the majority of conditions explored. Whereas the acoustic radiation force model gives maxima in $g_a$ at $x = \pm\lambda/8$, flame deflections utilized in evaluating $g_{a,\text{exp}}$ were consistently greatest in the immediate vicinity of the PN. In fact, even though the value of $F_a$, along with accompanying flame alterations, should be null precisely at the PN position according to Eq. (4.1), it is here that the most unstable flame behaviors were perceived. The degree of instability in the combustion processes at the PN, manifested through erratic vacillation of the flame plume and enhanced vapor bubble formation within fuel droplets causing dislodgement from the capillary, was such that reliable footage could not be gathered at $x = 0$ cm.

Forcing frequencies had a significant effect on the differences between experimental and theoretical $g_a$. The magnitude of the experimental acoustic accelerations and the discrepancy between the estimated $g_{a,\text{exp}}$ and $g_{a,\text{th}}$ for flow conditions of a given fuel was greatest at 332 Hz. Distributions of experimental acoustic acceleration displayed significant uniformity for $f_a$

with inherently large acoustic wavelengths as well, particularly for 332 Hz. This observation is supported by the fact that the largest $x$ established in the present studies, 5 cm, was much smaller than the span between the PN and PAN for 332 Hz, approximately 25.8 cm. These comparatively minuscule displacements with respect to the 332 Hz waveform effectually positioned the droplet in the same immediate proximity relative to the PN for all $x$. This is in stark contrast to profiles at 1500 Hz, where small translations in the acoustic assembly produce significant changes in position relative to PN and PAN locations and, thus, flame characteristics. Although the $g_{a,\text{exp}}$ and $g_{a,\text{th}}$ data for $f_a = 1500$ Hz typically differed substantially for $x$ near the PN as for all other $f_a$, it is noteworthy that, for $x > \lambda/8$ and $x < -\lambda/8$ approaching the PAN, both acoustic accelerations were quantitatively similar. This suggests that regions susceptible to high degrees of thermoacoustic coupling (near the PN) respond to forcing more vigorously than regions characterized by little to no interaction (near the PAN). These conclusions are investigated in the forthcoming discussion on quantification of thermoacoustic stability via $G$, the Rayleigh index, in Section 4.4.

Flame deflection behavior also hinged on air purging mechanics employed for the lower frequencies. Both Teshome [47] and Wegener [37] cited unexpected locations for the change in flame orientation at lower $f_a$ in all test fuels; that is, flame "switch" locations were not precisely coincident with the PN in all trials. Bias toward larger values of $\phi_f$ and $g_{a,\text{exp}}$ at negative $x$ were also reported. These effects were annulled by rectifying the traditional method for purging gaseous contents from the waveguide between experiments. Originally air was evacuated with compressed air provided by a single line mounted onto the wall of the waveguide apparatus while a portion of the speaker assembly lay within the waveguide. Purging with a line oriented parallel to the waveguide axis after complete removal of the speakers between trials corrected most erroneous cases of flame switching. When this was not effective, venting the waveguide naturally upon removal of the speakers for several minutes yielded the predicted flame behavior. The phenomenon interfering with proper deflection of the droplet flame was likely attributable to asymmetric temperature and species distributions that were not properly restored between experiments, though more detailed diagnostics are

required to assess this interpretation.

## 4.3 Flame Standoff Distance

Phase-locked image acquisition outlined in Section 2.3 enabled the inspection of acoustically coupled flame characteristics, including flame standoff distance $\delta_f$. Defined as the separation of the flame front demarcated by maxima in OH* chemiluminescence intensity from the droplet surface as pictured in Figure 2.10, $\delta_f$ was a function of the polar angle $\theta$. The flame position, however, was found to oscillate planarly with a frequency equal to that of the imposed waveform, $f_a$. That is, the sinusoidal fluctuation of the entire flame was horizontally confined for all applied forcing frequencies. This reaffirmed the planar nature of acoustic waves created within the waveguide. Additionally, it allowed the analysis of maxima and minima in $\delta_f$ at $\theta = 180^o$ for flames deflected to the right ($x > 0$ cm) or at $\theta = 0^o$ for flames deflected to the left ($x < 0$ cm) in the vicinity of the flame front.

This study predominantly scrutinized the hemisphere centered about the stagnation region of the flame front. This region is thought to coincide with elevated temperature and mass transfer rates for burning droplet geometries [23]. Chemiluminescence images that were phase-locked with respect to the acoustics and gathered during forced droplet combustion reveal dynamic standoff distance and integrated intensity oscillations near the flame stagnation point, as depicted in Figure 4.15. Measurements of $\delta_f$ at $\theta = 180^o$ for negatively oriented flames of all four fuels and a variety of $f_a$ and $x$ are also provided with accompanying temporally variable pressure perturbations in Figure 4.16. These convey the fundamental coupling between the fluctuating pressures and velocities and the flame response.

Measured standoff distance oscillations were sensitive to applied $f_a$ as well as $p'$ and $u'$ profiles at various waveguide locations for all fuels. Generally $\delta_f$ was found to fluctuate out-of-phase with pressure perturbations, meaning that at higher pressures the flame was closer to the droplet surface. Moreover, situating the burning droplet near the PN (or VAN) generally magnified the standoff distance amplitude $\delta_f'$. Droplet displacements in the

proximity of PAN (or VN), on the other hand, reduced $\delta'_f$ and virtually removed flame oscillations. These effects were attributed to the enhancement and attenuation of $u'$ at various waveguide positions which altered the relative oxidizer mass fractions and the resulting local fuel-air equivalence ratio in the reaction zone. The perceived motion of the flame simply corresponded to the translocation of the reaction zone to a region whose fuel and oxidizer mixture fractions more closely approaches stoichiometric conditions. The chemical kinetics associated with acoustically coupled droplet combustion displayed a salient dependence on the administered $f_a$. The frequency response in $\delta'_f$ demonstrated in Figure 4.17 stemmed from dissimilar acoustic time scales associated with the standing waves. Waveforms generated at lower frequencies, like 332 Hz, exhibited relatively large acoustic time periods ($T_a = \frac{1}{f_a}$) that fostered species diffusion as a result of longer intervals before the flow was reversed at maximum or minimum $u'$. Lower $f_a$ with $T_a$ much greater than kinetic time scales associated with diffusion-limited droplet combustion allowed for greater magnitudes of $\delta'_f$. Conversely, the flow fields with equivalent $u'$ but inherently small acoustic time scales comparable to the chemical times of the reaction, as with $f_a = 1500$ Hz, prohibited diffusion of species and diminished $\delta'_f$. In fact, droplet locations that overlapped with PAN regions denigrated all oscillatory flame behavior.

Mean flame position averaged temporally over several acoustic cycles, while distinct for each fuel, demonstrated remarkably consistent trends with respect to $f_a$ and $x$. Such time-averaged deformations of the flame front in the stagnation region were also evaluated for $\theta$ yielding the largest fluctuations in $\delta_f$ ($\theta = 180^o$ for $x > 0$ cm and $\theta = 0^o$ $x < 0$ cm). Mean standoff distance $\bar{\delta_f}$ resulted from acquisition of the mean in sinusoidal oscillations of $\delta_f$, which varied for distinct fuels on account of chemistry-specific flame topologies, as seen in Figure 4.1. The alcohol fuels investigated here, comprised of short carbon-hydrogens chains, generally produced flames that burned closer to the continuously replenished liquid droplets. Long-chain kerosene and aromatic compounds constituting the aviation-grade hydrocarbons studied featured greater overall $\delta_f$. While the absolute magnitudes of mean flame standoff distance were singular to each fuel, distributions of $\bar{\delta_f}$ relative to the droplet location with

respect to the cental PN for different forcing frequencies seen in Figure 4.18 were analogous. The lower $f_a$ (332 Hz, 898 Hz) generally minimized the mean standoff distances uniformly for all $x$. At 1500 Hz, where the displacements of the acoustic assembly approximated the separation between PN and PAN structures, $\bar{\delta_f}$ increased monotonically from positions close to the PN to those approaching PAN. Those $\delta_f$ achieved near the PAN mirrored values for unforced burning droplets.

Global flame phenomena with innate macroscale characteristic times for the burning droplet subject to acoustic excitation, like experimental acoustic accelerations and burning rate constants, correlated well with the microscale temporal fluctuations of standoff distance. The assortment of $K$ and $g_{a,\mathrm{exp}}$ recorded at different waveguide locations $x$ for the fuels and forcing frequencies implemented mimicked the measured $\delta_f'$. The homogeneity in dispositions of $K$ and $\delta_f'$ can be understood by recognizing that larger standoff distance oscillations in regions of pronounced $u'$ near the PN (or VAN) stimulated greater mass diffusion via fuel vaporization. Similarly, more prominent net temperature gradients promoted by the reduced mean separation of the flame front and the droplet surface near the PN over several acoustic cycles explained the inverse relationship between the burning rate constants and $\bar{\delta_f}$. The time-averaged nature of the mean standoff distances observed led Wegener [37] to surmise a possible correspondence between $\bar{\delta_f}$ and theoretical $g_a$. While the acoustic radiation force theory described time-averaged forces caused by acoustic fluctuations, Wegener discovered a contradictory interrelation between mean flame displacement and theoretical acoustic acceleration. This disparity, along with the physical and modeled inconsistencies resulting in the disagreement between $g_{a,\mathrm{exp}}$ and $g_{a,\mathrm{th}}$, was the primary stimulus for the assessment of thermoacoustic coupling absent in the formulation of the acoustic radiation force theory.

## 4.4 Rayleigh Index

Spatial analysis of the Rayleigh index in the context of droplet combustion within an acoustically resonant environment was enabled through synchronous acquisition of pressure and

OH* chemiluminescence intensity perturbations. The timing arrangement installed to allow communication between the pressure transducer circuitry, the data acquisition board, and the intensified camera system was discussed in Section 2.3.3. This arrangement relayed discrete pressure readings and integrated image luminosities corresponding to individual frames of the combustion footage. The discontinuous nature of measurement logging disallowed a direct calculation of $G$ performed through the traditionally defined integral in Eq. (2.6); instead, the Rayleigh index was computed as in Eq. (2.9) through summation of the products of $p'$ and $q'$ inferred from OH* chemiluminescence for each image. The phase-locked footage was taken over a range of evenly-spaced relative acoustic phase values separated by $24^o$ over one cycle. In this sense fifteen consecutive images formed the basis for the pressures and intensities employed in computing $G$ for a single acoustic period. Prior to their implementation in the derivation of the Rayleigh index, the luminosities associated with combustion images were refined to correct for the artificial intensities present outside the flame and the transient decay in OH* radiative deexcitation. OH* chemiluminescence deterioration innate to the consumption of oxidizer in the vicinity of the droplet over tens of seconds following ignition as exemplified in Figures 2.11 and 2.12 was adjusted so as to achieve oscillations in the integrated intensity $I$ about a consistent mean value. The quality of oscillatory integrated intensity perturbation $I'$ was ameliorated by only incorporating pixels whose luminosities lay above a preset intensity threshold found within the flame region.

These decay-corrected integrated threshold intensities were observed to fluctuate sinusoidally with pressure perturbations. As alluded to in the burning droplet images presented along with phase-dependent $p'$ in Figure 4.15, profiles of dynamic $I'$ and $p'$ recorded concurrently with droplet combustion for an array of locations and forcing frequencies evolved with little relative phase difference between them, as evidenced for ethanol in Figure 4.19. Coupling of the acoustic forcing with OH* luminosity fluctuations was physically consistent with the out-of-phase relationship between flame standoff distances and said pressure perturbations. Flame positions most proximate to the droplet heightened temperature gradients governing the reaction rates for hydroxyl production and deexcitation in Eq. (2.2) and Eq.

(2.3), respectively. This produced maxima in $I'$ for minima in $\delta'_f$. Contrarily, relatively large separation between the flame front and the droplet expressed as increased standoff distances lead to weakened chemiluminescence output. Lethargic intensity oscillations were also perceived while approaching PAN (VN) structures, a consequence of feeble $u'$ and $\delta'_f$.

The fundamental frequency dependence observed in the computed $G$ for the alcohol fuels at droplet locations relative to the central PN underlined the susceptibility of the chemical kinetics to imposed acoustic forcing. Rayleigh indices calculated for methanol and ethanol fuels for specific $f_a$ are plotted with experimental acoustic accelerations in Figures 4.2 through 4.7 and individually for each fuel across all forcing frequencies in Figures 4.20 and 4.21. The dimensionless $G$ were derived from normalized pressure and intensity perturbations. Pressure perturbations were scaled by $p'_{max} = 150$ Pa common to all flow conditions in this study. Oscillating integrated intensities, however, could not be scaled with a single $I$ common to all flow conditions on account of the disproportionate quantity of photon input within image exposures collected at distinct $f_a$ for the various fuels. Instead, the luminosities of each fuel were standardized with the integrated OH* chemiluminescence gathered in unforced flames at a given excitation frequency. Ultimately the positive nondimensional $G$ emphasize the occurrence of acoustically-coupled combustion throughout the waveguide. The degree of coupling is consistently greater for lower applied frequencies in the PN region; droplet positions yielding nearly imperceptible $G$ near the PAN at higher $f_a$ , in contrast, indicate almost no interaction between the acoustic field and the combustion processes. The sensitivity of the flame chemistry to forcing frequencies reinforced by these results affirms the documented tendencies of acoustically stimulated reactive systems found in previous work by Egolfopoulos *et al.* [75], Selerland *et al.* [76], and Kim *et al.* [77]. Evidence in this and prior investigations suggest the inability of flames to keep up with high frequency acoustic forcing with characteristic time scales comparable to that of the diffusion-limited chemical kinetics.

Coupling of acoustics with combustion processes elucidate the global flame behavior observed, specifically with regard to the disparity between quantitative acoustic acceleration

results from experimentation and from the acoustic radiation force theory. Save for locations closest to the central PN, Figures 4.2 through 4.7 accentuate the congruence in $G$ and $g_{a,\text{exp}}$. Furthermore, the conspicuous similarities in experimental acoustic acceleration and standoff distance oscillation amplitude engendered by the acoustic disturbances reinforce that combustion instability plays a role in bulk phenomena responsible for flame deflection. The absence of reactive modeling with inherent chemical-kinetic frequency responses to acoustically perturbed environments in the acoustic radiation force model is manifested in erroneous theoretical $g_a$. Such a model could only hold in regimes where the acoustics interact anemically with the reacting system so as to inconsequentially treat a flame as a benign volume of low density gases. This is exactly why acoustic accelerations at $x$ with minute $G$ present near PAN for $f_a = 1500$ Hz are predicted with such reliability using the bracketed term for $F_a$ in Eq. (4.1). Nevertheless, the characterization of experimental $g_a$ very close to the PN with the Rayleigh index is not attainable due to constraints in the definition of $G$.

Predictive limitations of the Rayleigh index lie within its inability to characterize thermoacoustic instability in the exact PN position and complications in the evaluation of $I'$ given imaging and post-processing restrictions. The distributions for $G$ outlined here exclude results for JP-8 and FT. Combustion of liquid JP-8 and FT droplets was distinguished by the extreme luminosities in the wake region of the flame structure, as imaged in Figure 4.1. The dominant integrated intensities in the flame plume overwhelmed any chemiluminescent oscillation within the flame front near the stagnation region of interest. The footage gathered could not be corrected for this severe luminous inequality posthumously. Hence the only temporal fluctuation in chemiluminescence recorded barring luminosity decay was that of the flame entering and exiting the field of view. Improvements in image filter conditioning and intensity segregating algorithms in future work may allow quantification of instability through the Rayleigh index for these fuels. The successful evaluation of $G$ in alcohol fuels was not without defect though. The Rayleigh indices conveyed in Figures 4.20 and 4.21 portrayed the immediate proximity to the PN as less prominently coupled with the acoustic environment as compared to more removed locations. This is not physically accurate, as

the perturbations in luminosity and flame standoff distance in Figures 4.16 and 4.19 both reflect the most pronounced flame response in the immediate vicinity of the PN. The deceptive nature of the Rayleigh index near $x = 0$ cm is credited to two factors. First, the inability to stabilize the flame and droplet at the exact PN position limits the quantification of instability in the location that, by extrapolation, should be stimulated most by the acoustic environment. Second, $G$ as formulated in Eq. (2.6) is reliant on amplitudes of $p'$ for diagnosing exacerbation in combustion instability. Yet, in this system, the most unstable region is inherently void of oscillations in pressure. These shortcomings motivate detailed modeling of the acoustically excited burning droplet to gauge dynamic stability properties not regarded in the current experiment.

Table 4.1: Experimental and Reference Burning Rate Constants for Various Fuel Droplets in the Absence of Acoustic Excitation.

| Fuel | $K$, present ($mm^2/s$) | $K$, established ($mm^2/s$) |
|---|---|---|
| Ethanol | 0.82-0.88 | 0.81-0.86 [24] |
| Methanol | 0.83-0.90 | 0.85-1.2 [78, 79] |
| Pure JP-8 | 0.95-1.04 | - |
| Pure FT | 0.94-1.02 | - |

(a) Ethanol

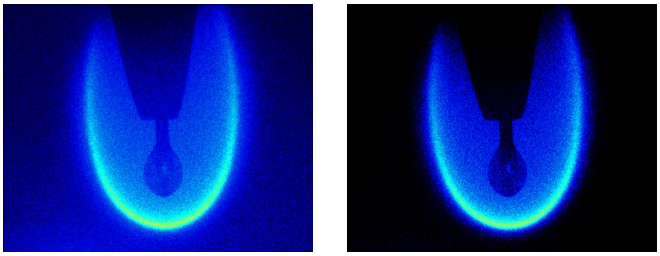

(b) Methanol

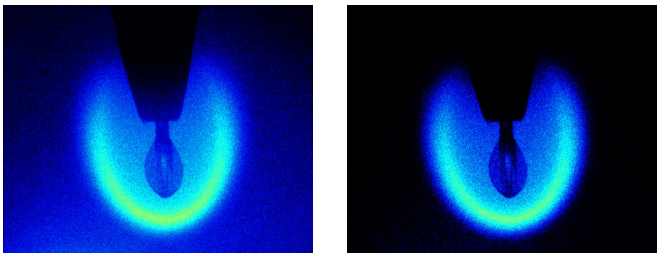

(c) Pure JP-8

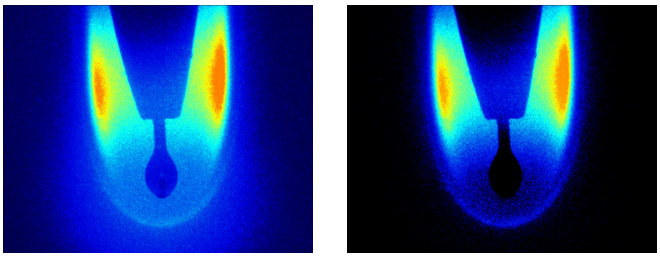

(d) Pure FT

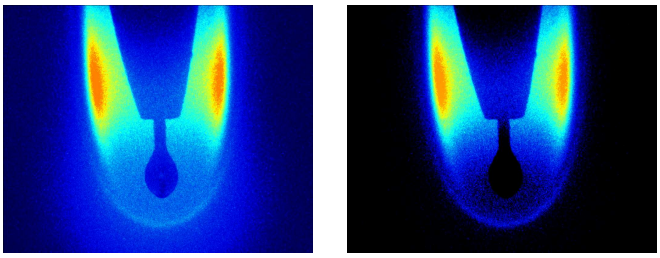

Figure 4.1: OH* chemiluminescence images of burning droplets in the absence of acoustic forcing. The left column shows an image as captured. The right column shows the same image after background light subtraction.

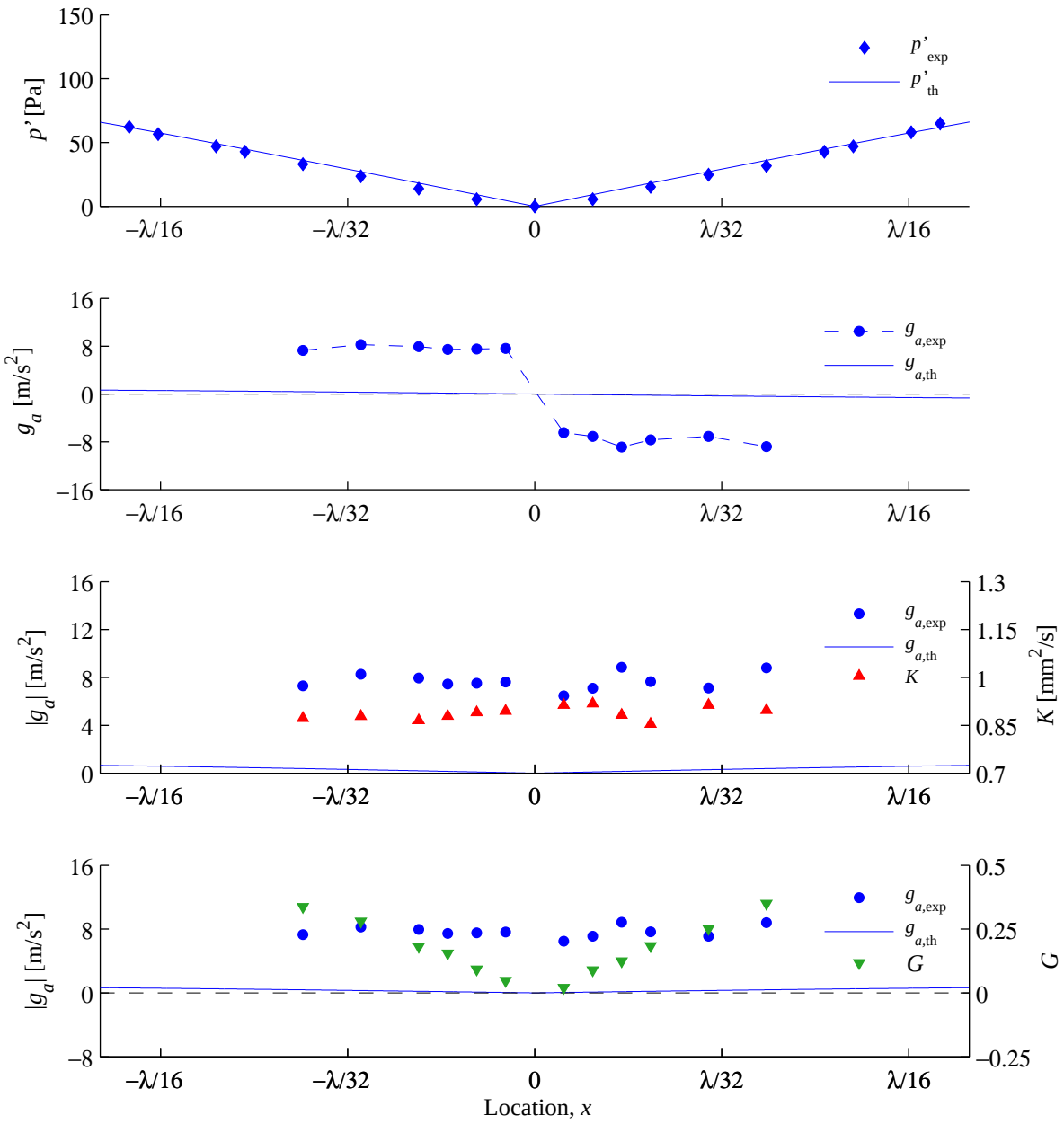


Figure 4.2: Pressure perturbation amplitude $p'$, estimated experimental and theoretical acoustic accelerations $g_a$, average burning rate constant $K$, and average Rayleigh index $G$ as a function of the displacement $x$ with respect to the central pressure node position for ethanol droplet burning in the vicinity of said pressure node at $f_a = 332$ Hz, $\lambda = 103.3$ cm, and $p'_{max} = 150$ Pa.

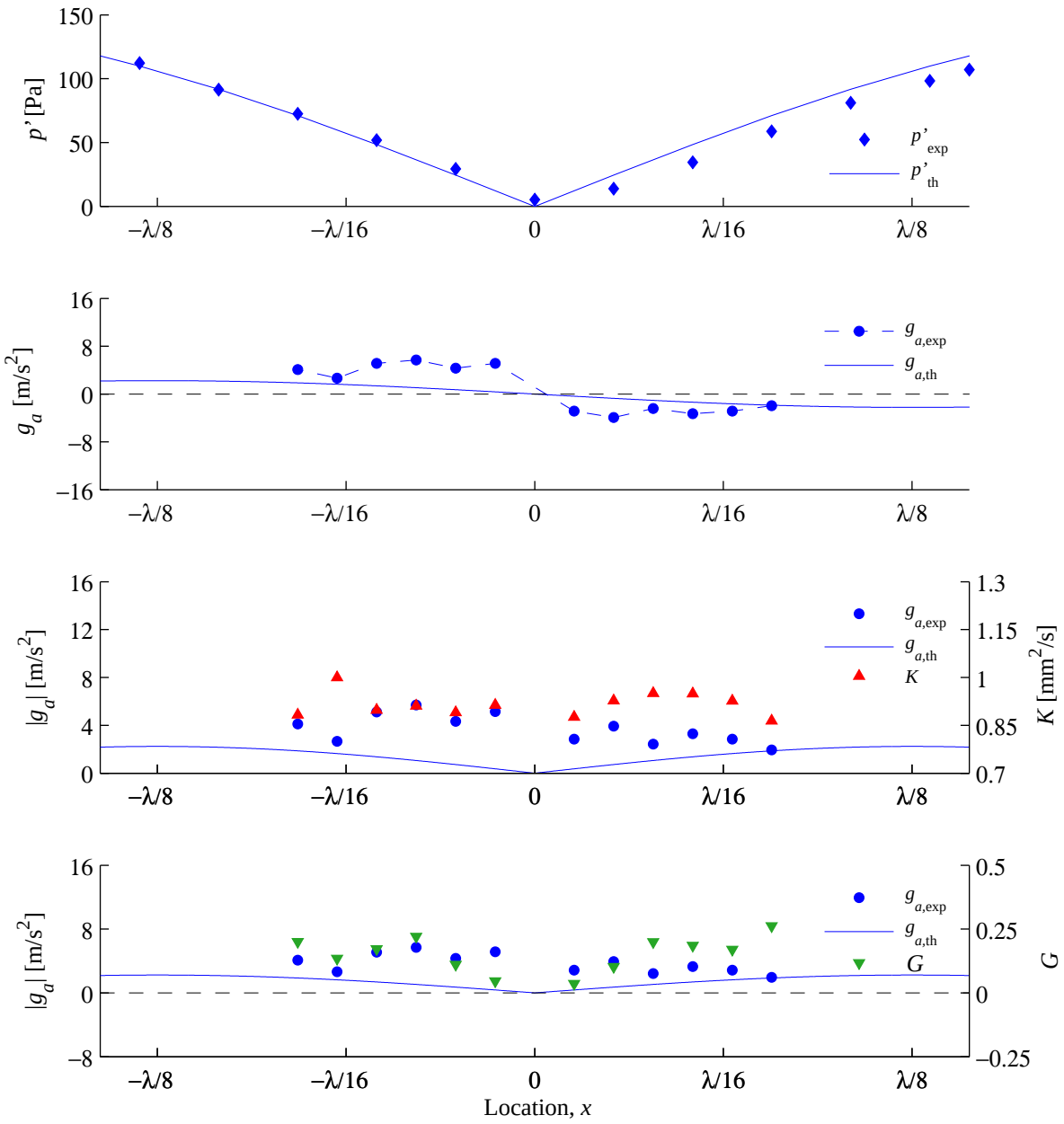


Figure 4.3: Pressure perturbation amplitude $p'$, estimated experimental and theoretical acoustic accelerations $g_a$, average burning rate constant $K$, and average Rayleigh index $G$ as a function of the displacement $x$ with respect to the central pressure node position for ethanol droplet burning in the vicinity of said pressure node at $f_a = 898$ Hz, $\lambda = 38.2$ cm, and $p'_{max} = 150$ Pa.

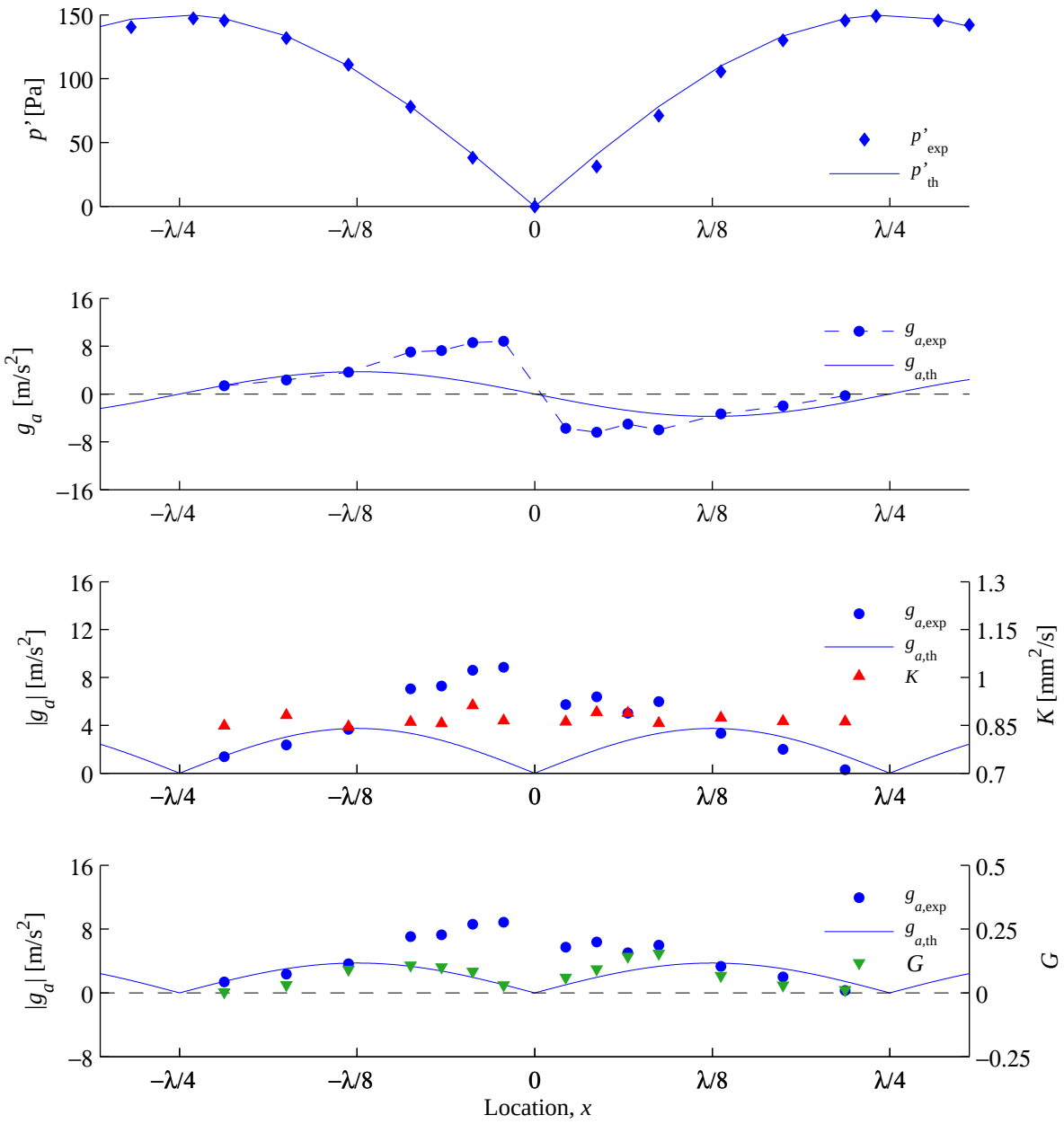


Figure 4.4: Pressure perturbation amplitude $p'$, estimated experimental and theoretical acoustic accelerations $g_a$, average burning rate constant $K$, and average Rayleigh index $G$ as a function of the displacement $x$ with respect to the central pressure node position for ethanol droplet burning in the vicinity of said pressure node at $f_a = 1500$ Hz, $\lambda = 22.9$ cm, and $p'_{max} = 150$ Pa.

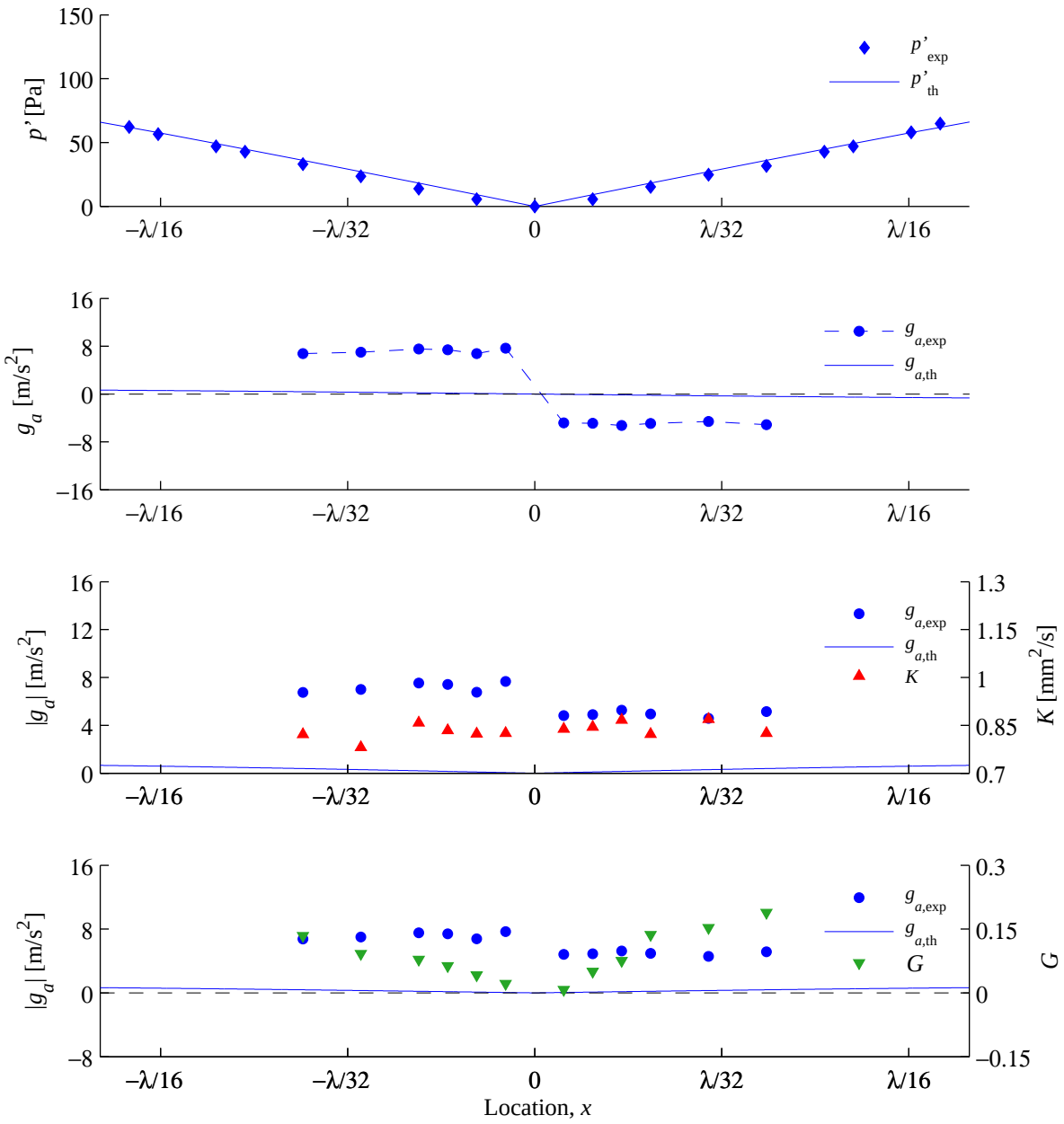


Figure 4.5: Pressure perturbation amplitude $p'$, estimated experimental and theoretical acoustic accelerations $g_a$, average burning rate constant $K$, and average Rayleigh index $G$ as a function of the displacement $x$ with respect to the central pressure node position for methanol droplet burning in the vicinity of said pressure node at $f_a = 332$ Hz, $\lambda = 103.3$ cm, and $p'_{max} = 150$ Pa.

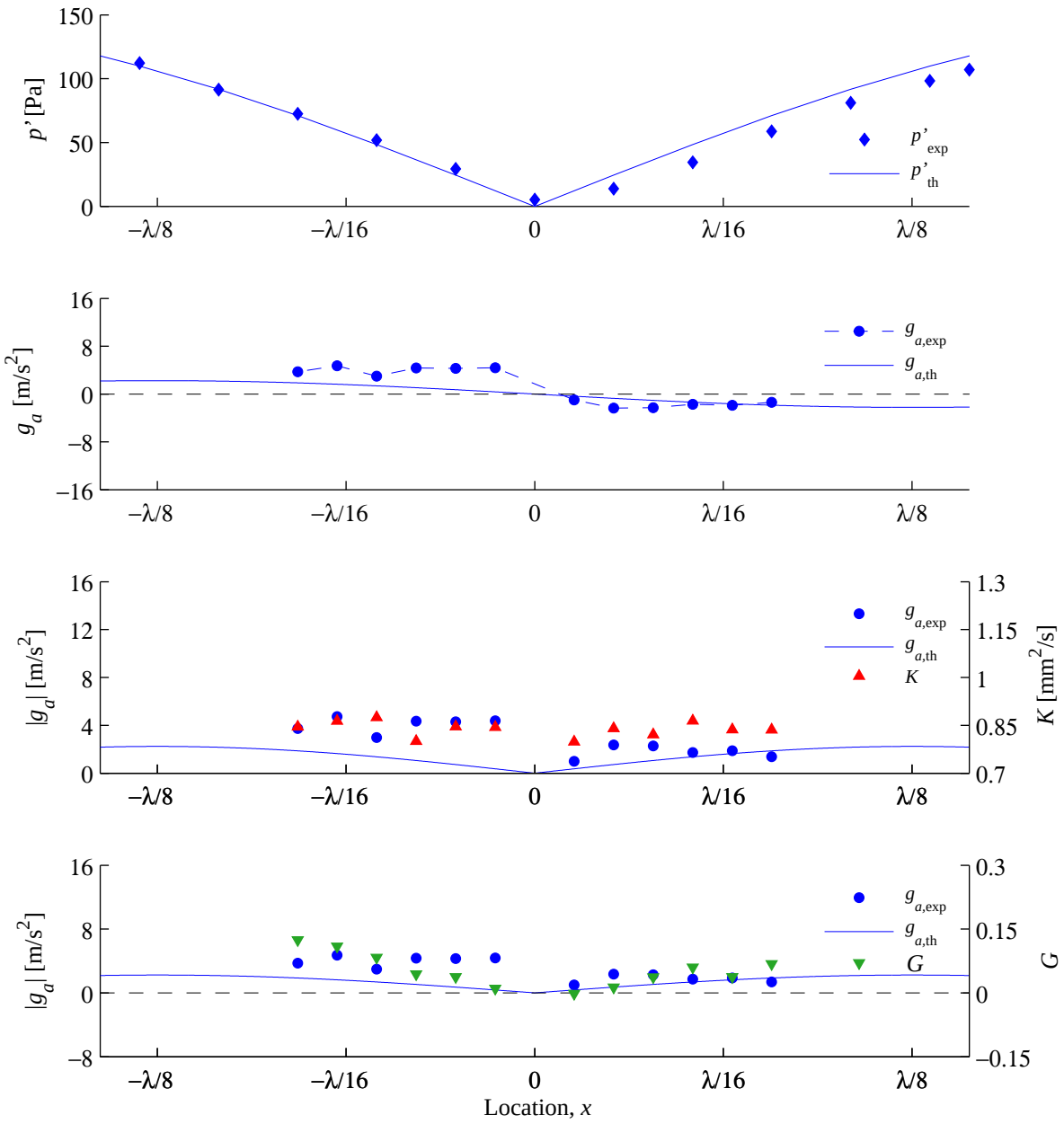


Figure 4.6: Pressure perturbation amplitude $p'$, estimated experimental and theoretical acoustic accelerations $g_a$, average burning rate constant $K$, and average Rayleigh index $G$ as a function of the displacement $x$ with respect to the central pressure node position for methanol droplet burning in the vicinity of said pressure node at $f_a = 898$ Hz, $\lambda = 38.2$ cm, and $p'_{max} = 150$ Pa.

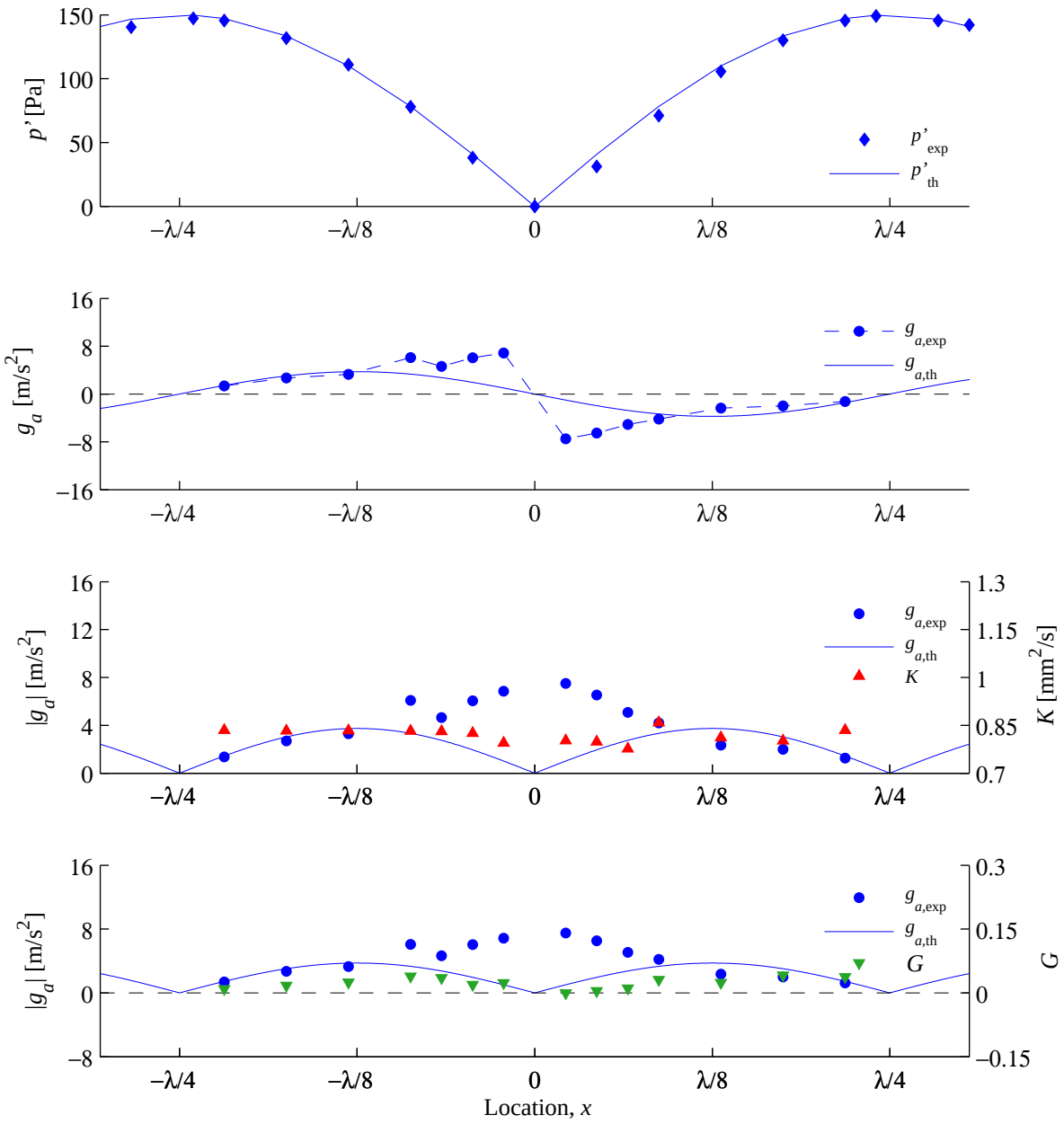


Figure 4.7: Pressure perturbation amplitude $p'$, estimated experimental and theoretical acoustic accelerations $g_a$, average burning rate constant $K$, and average Rayleigh index $G$ as a function of the displacement $x$ with respect to the central pressure node position for methanol droplet burning in the vicinity of said pressure node at $f_a = 1500$ Hz, $\lambda = 22.9$ cm, and $p'_{max} = 150$ Pa.

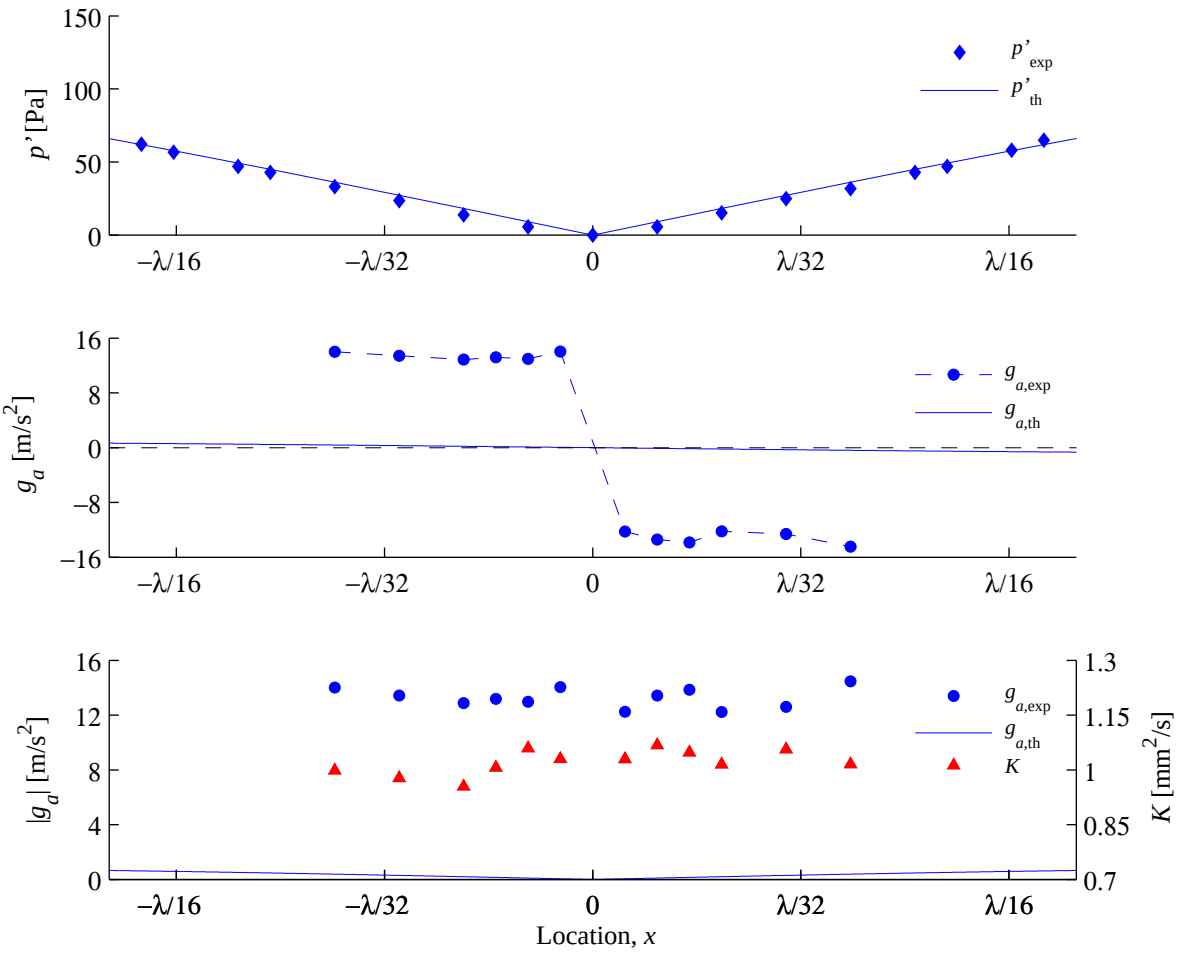


Figure 4.8: Pressure perturbation amplitude $p'$, estimated experimental and theoretical acoustic accelerations $g_a$, and average burning rate constant $K$ as a function of the displacement $x$ with respect to the central pressure node position for JP-8 droplet burning in the vicinity of said pressure node at $f_a = 332$ Hz, $\lambda = 103.3$ cm, and $p'_{max} = 150$ Pa.

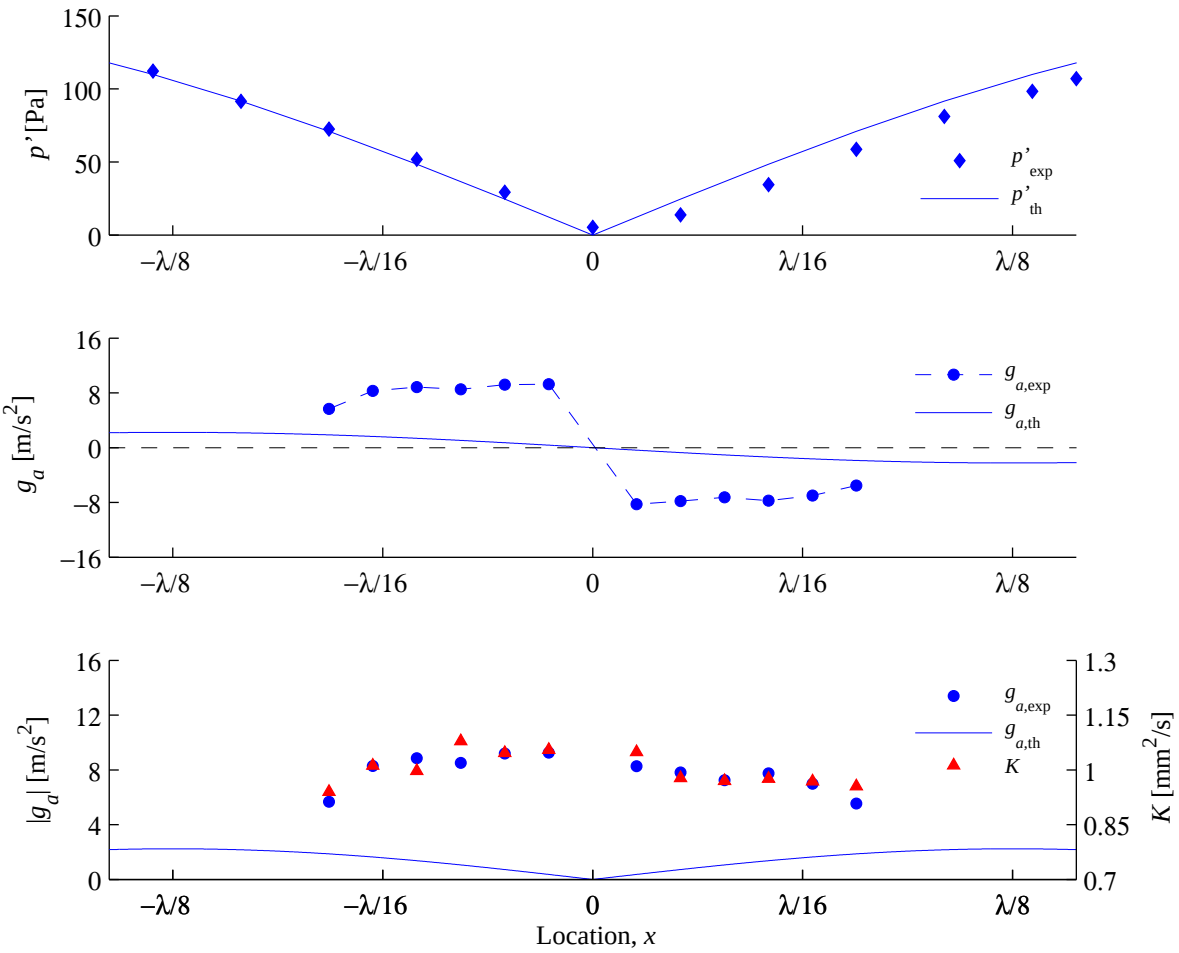


Figure 4.9: Pressure perturbation amplitude $p'$, estimated experimental and theoretical acoustic accelerations $g_a$, and average burning rate constant $K$ as a function of the displacement $x$ with respect to the central pressure node position for JP-8 droplet burning in the vicinity of said pressure node at $f_a = 898$ Hz, $\lambda = 38.2$ cm, and $p'_{max} = 150$ Pa.

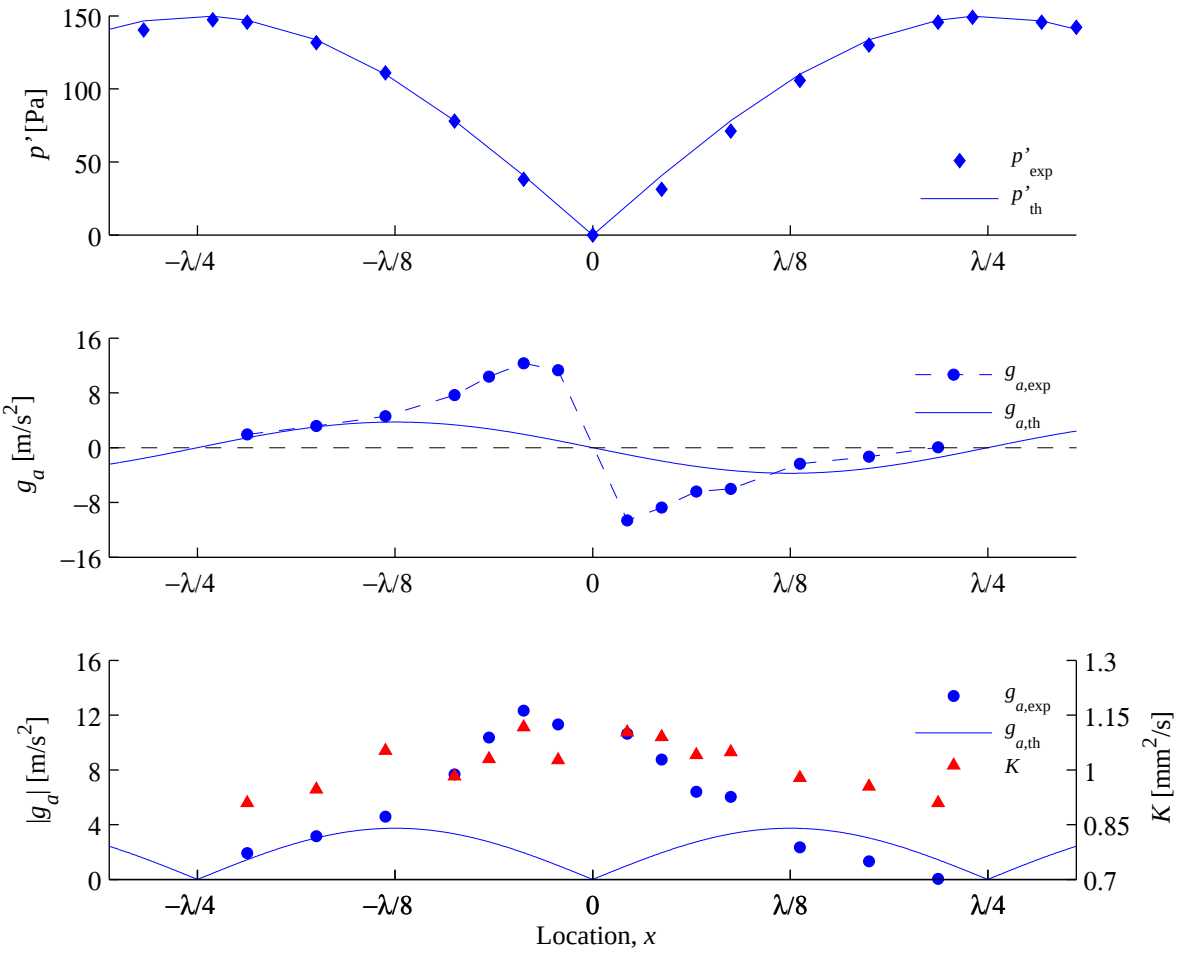


Figure 4.10: Pressure perturbation amplitude $p'$, estimated experimental and theoretical acoustic accelerations $g_a$, and average burning rate constant $K$ as a function of the displacement $x$ with respect to the central pressure node position for JP-8 droplet burning in the vicinity of said pressure node at $f_a = 1500$ Hz, $\lambda = 22.9$ cm, and $p'_{max} = 150$ Pa.

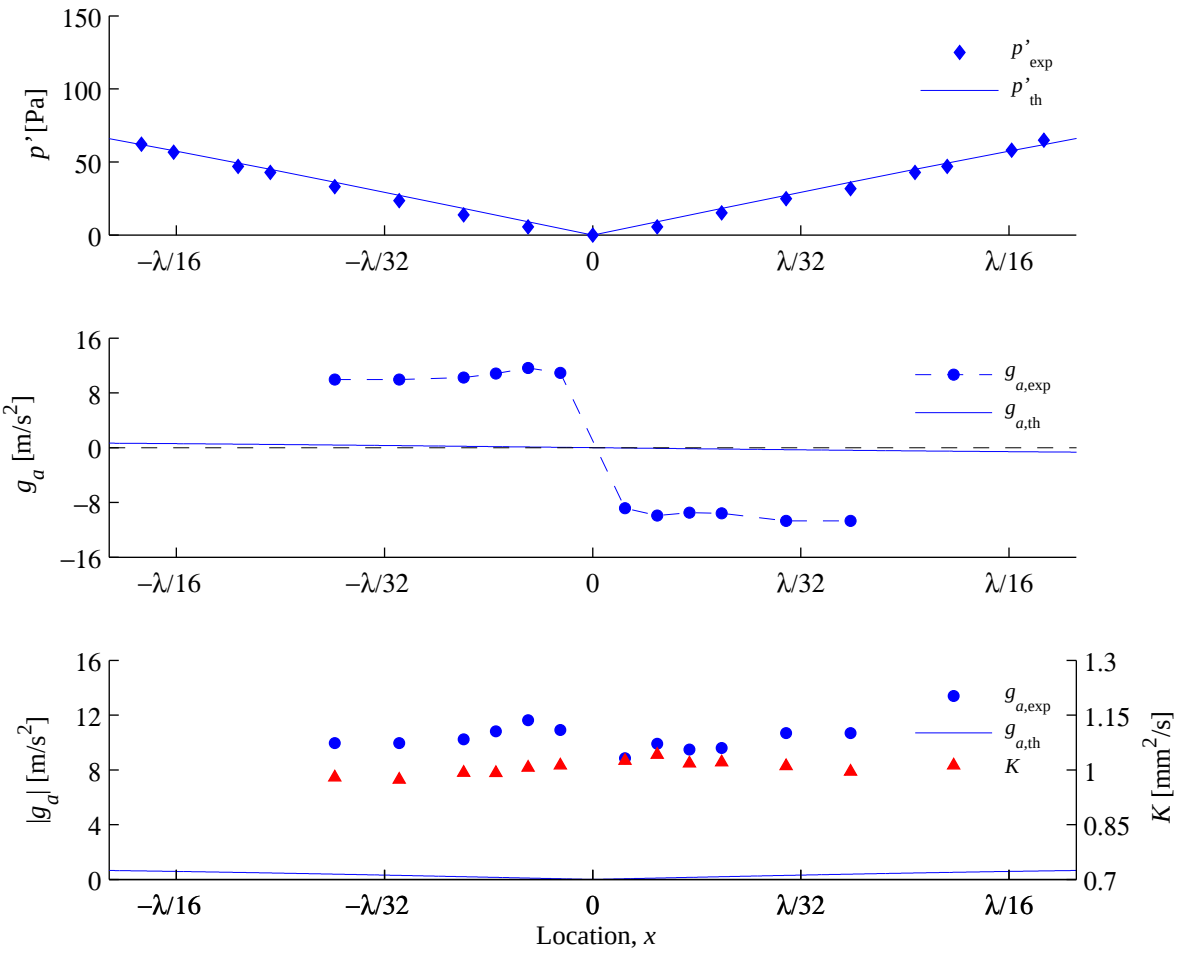


Figure 4.11: Pressure perturbation amplitude $p'$, estimated experimental and theoretical acoustic accelerations $g_a$, and average burning rate constant $K$ as a function of the displacement $x$ with respect to the central pressure node position for FT droplet burning in the vicinity of said pressure node at $f_a = 332$ Hz, $\lambda = 103.3$ cm, and $p'_{max} = 150$ Pa.

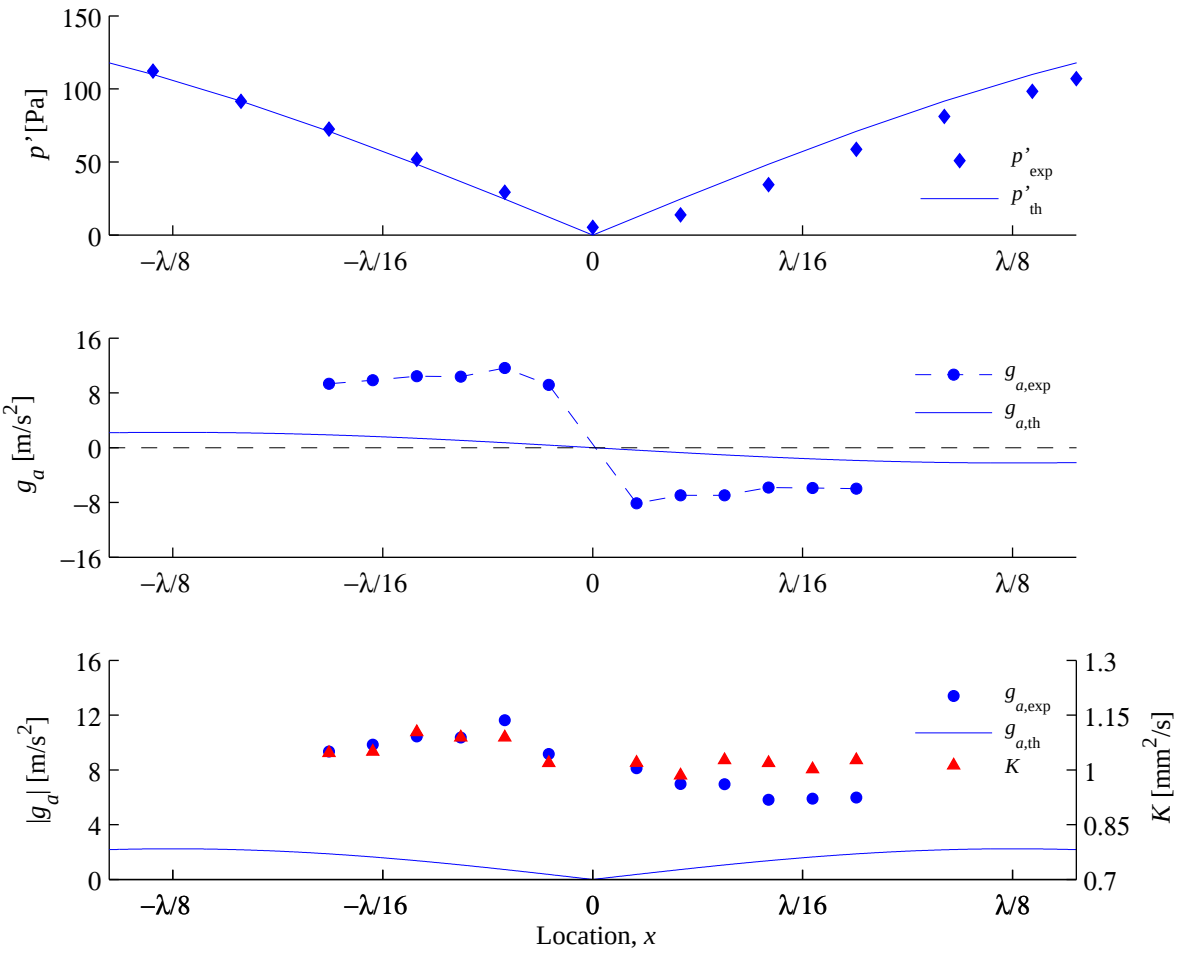


Figure 4.12: Pressure perturbation amplitude $p'$, estimated experimental and theoretical acoustic accelerations $g_a$, and average burning rate constant $K$ as a function of the displacement $x$ with respect to the central pressure node position for FT droplet burning in the vicinity of said pressure node at $f_a = 898$ Hz, $\lambda = 38.2$ cm, and $p'_{max} = 150$ Pa.

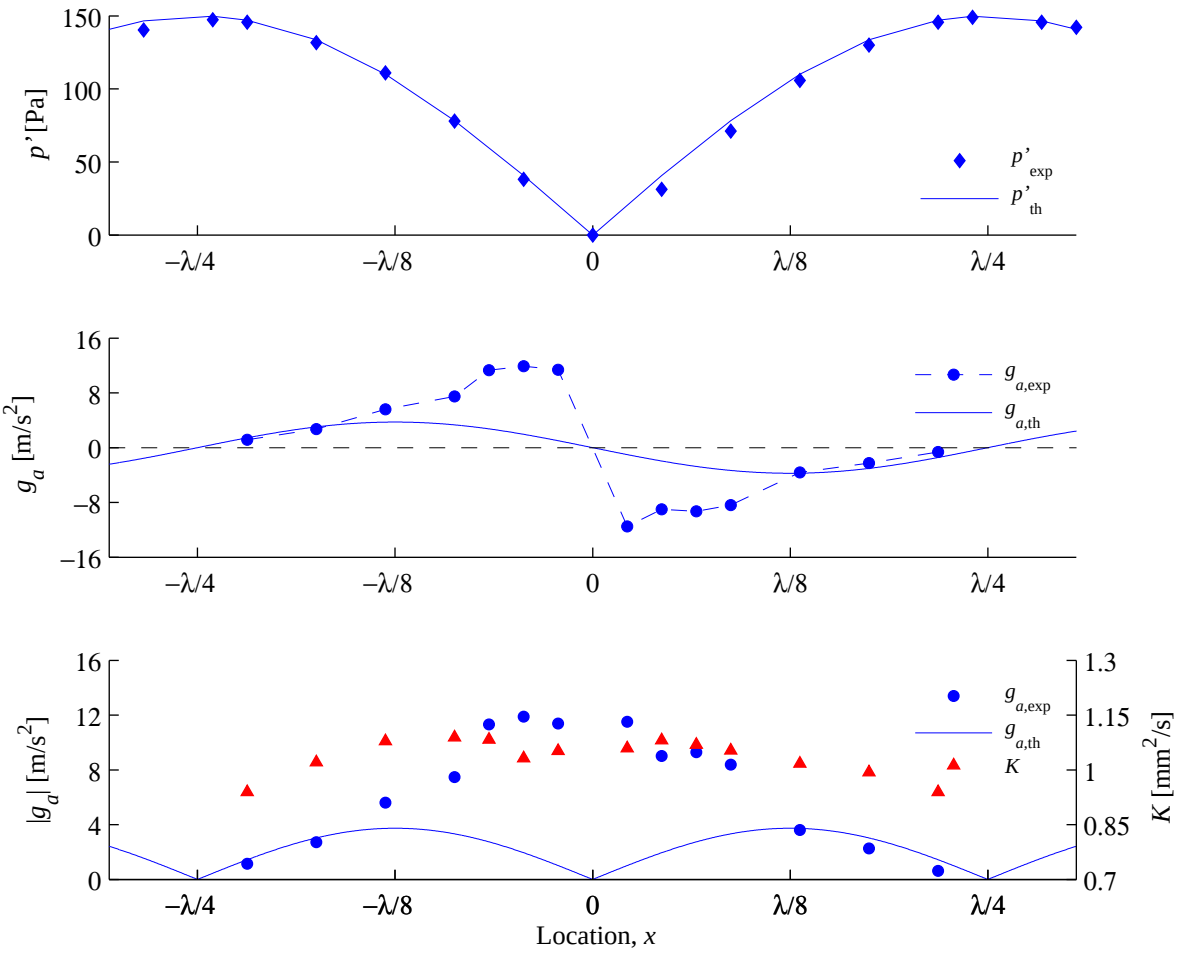


Figure 4.13: Pressure perturbation amplitude $p'$, estimated experimental and theoretical acoustic accelerations $g_a$, and average burning rate constant $K$ as a function of the displacement $x$ with respect to the central pressure node position for FT droplet burning in the vicinity of said pressure node at $f_a = 1500$ Hz, $\lambda = 22.9$ cm, and $p'_{max} = 150$ Pa.

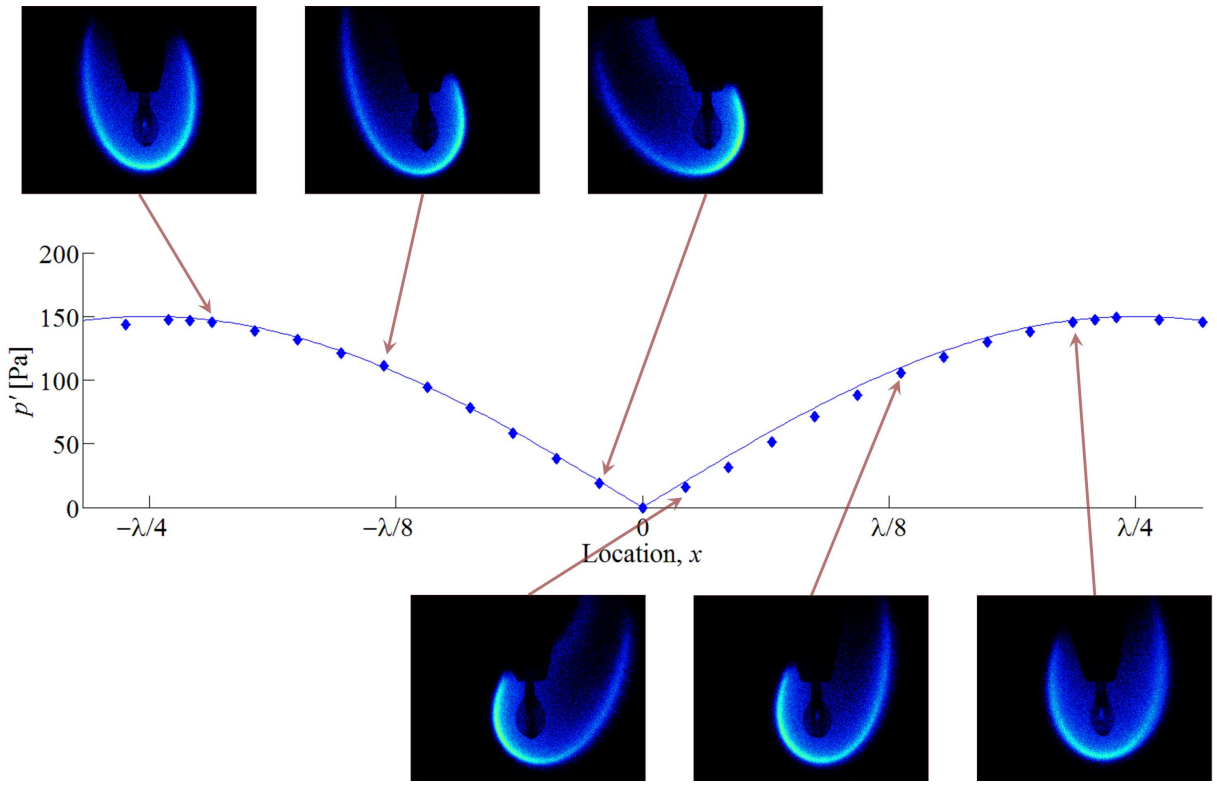


Figure 4.14: Ethanol flames under acoustic forcing at $f_a = 1500$ Hz with measurements of $p'$ for corresponding waveguide locations $x$. Flame plumes are consistently deflected away from the pressure node (PN), with a flame "switch" occurring at $x \approx 0$ cm.

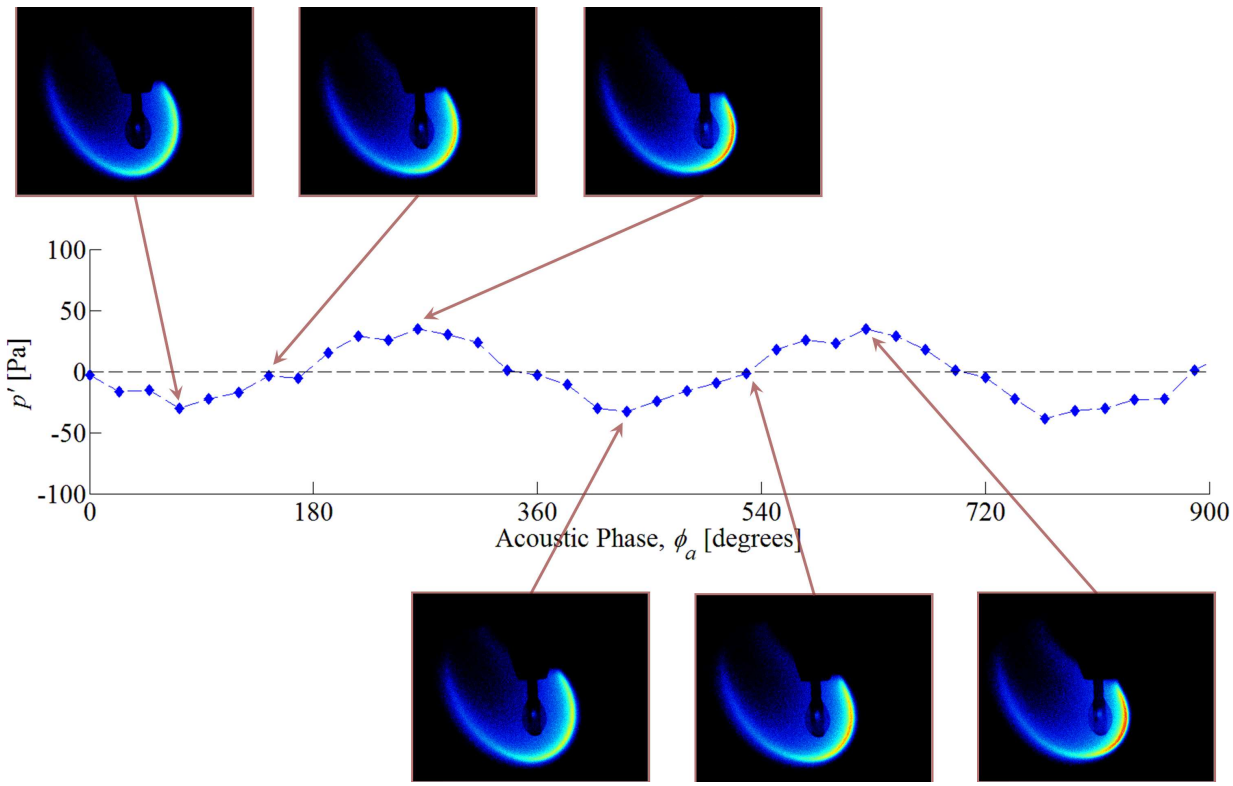


Figure 4.15: Ethanol flames under acoustic forcing at $f_a$ = 332 Hz and $x$ = -3 cm with measurements of $p'$ for corresponding acoustic phases $\phi_a$. Horizontal flame standoff distance $\delta_f$ and integrated chemiluminescence intensity $I$ both oscillate with $p'$ at the imposed $f_a$. Sinusoidal intensity fluctuations occur out-of-phase with respect to the standoff distance perturbations but are in-phase with $p'$.

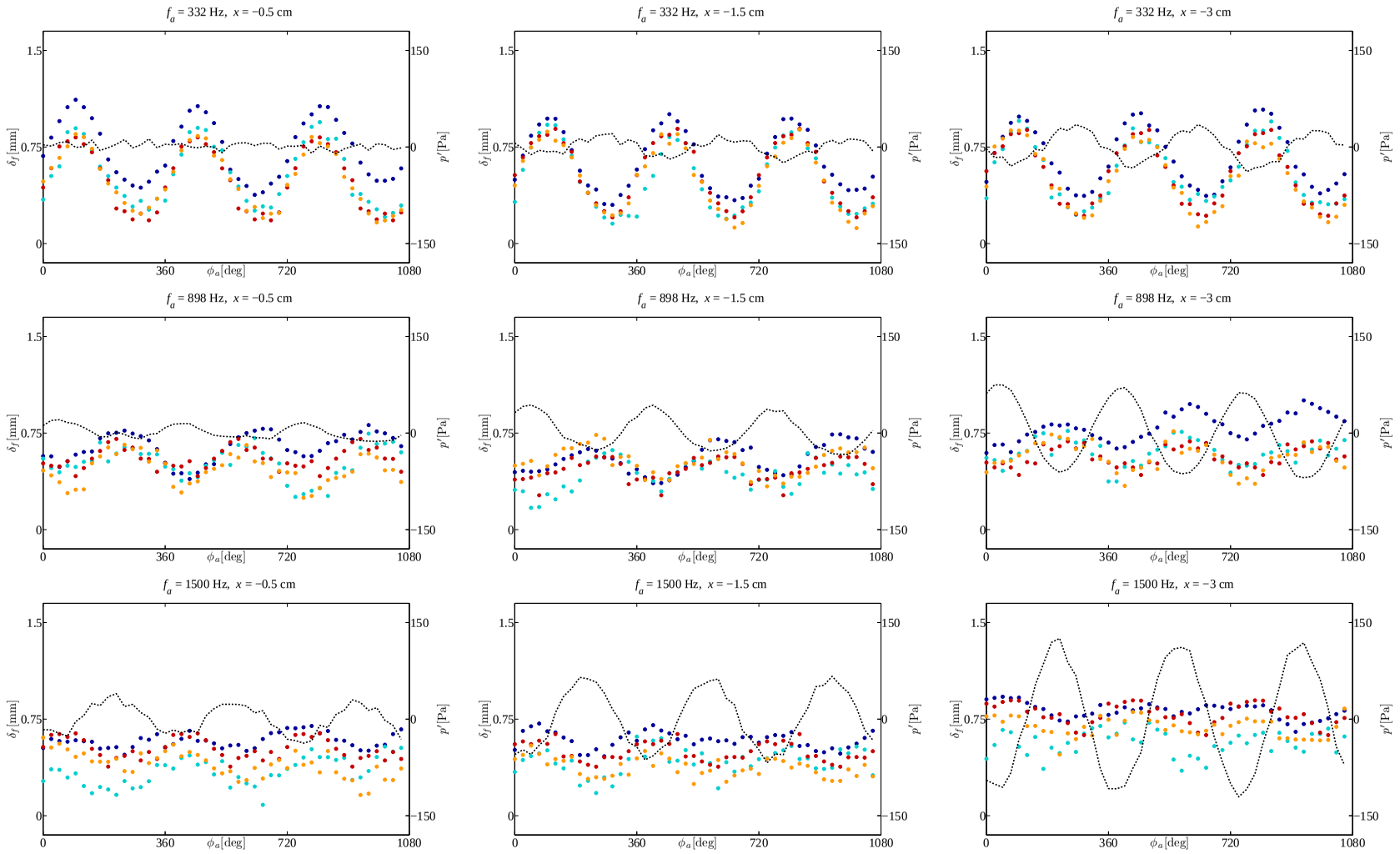


Figure 4.16: Horizontal flame standoff distance ( ● ) and pressure perturbation (---) plotted versus acoustic phase. All fuels and frequencies are shown for three select waveguide locations. (Rows: $f_a = 332$ Hz (top) $f_a = 898$ Hz (center) $f_a = 1500$ Hz (bottom); Columns: $x = -0.5$ cm (left) $x = -1.5$ cm (middle) $x = -3$ cm (right); Fuels: ethanol ( ● ), methanol ( ● ), JP-8 ( ● ), FT ( ● )).

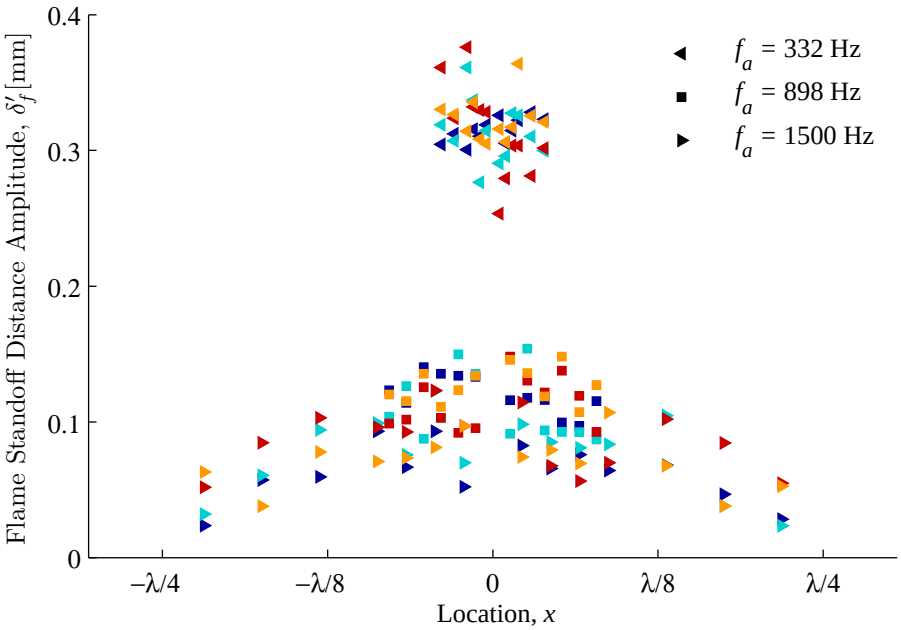


Figure 4.17: Horizontal flame standoff distance oscillation amplitudes $\delta'_f$ for all fuels and acoustic frequencies at various locations $x$. (Fuels: ethanol ( ● ), methanol ( ● ), JP-8 ( ● ), FT ( ● ) )

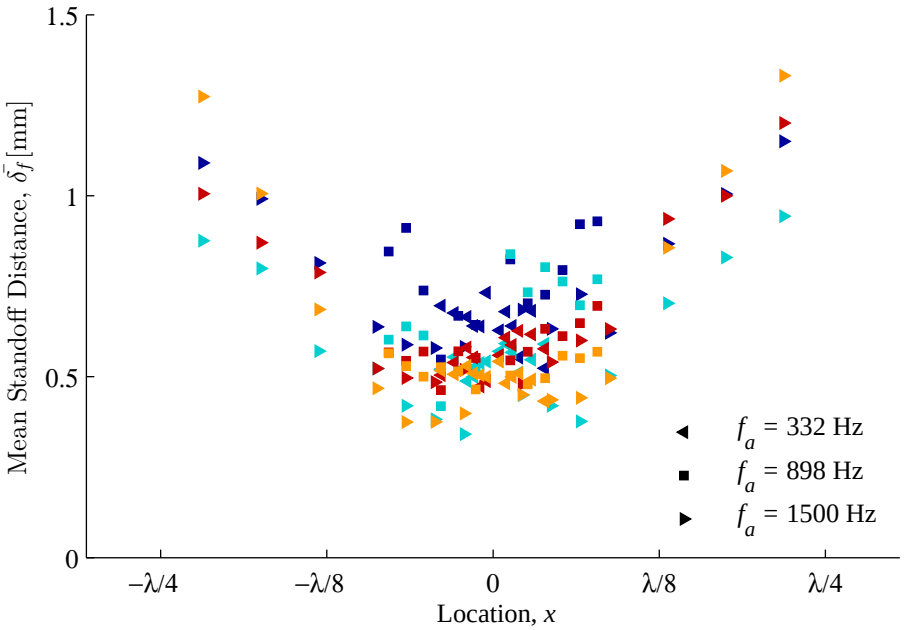


Figure 4.18: Time-averaged flame standoff distance $\bar{\delta_f}$ for all fuels and acoustic frequencies at various locations $x$. (Fuels: ethanol ( ● ), methanol ( ● ), JP-8 ( ● ), FT ( ● ) )

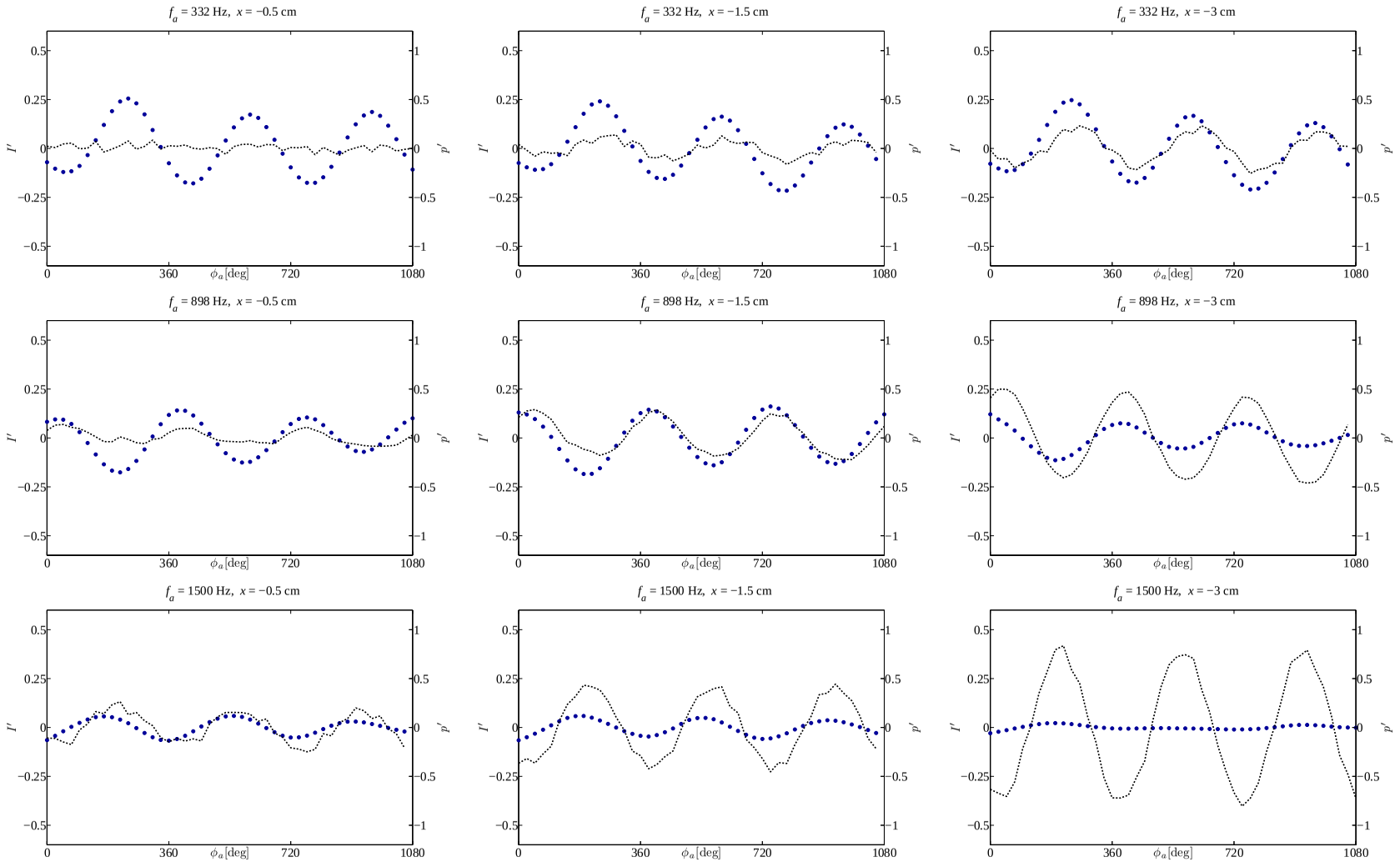


Figure 4.19: Normalized intensity perturbation ( ● ) and pressure perturbation (---) plotted versus the acoustic phase. Measurements correspond to burning droplets of ethanol for all acoustic frequencies and three select waveguide locations. (Rows: $f_a = 332$ Hz (top) $f_a = 898$ Hz (center) $f_a = 1500$ Hz (bottom); Columns: $x = -0.5$ cm (left) $x = -1.5$ cm (middle) $x = -3$ cm (right)).

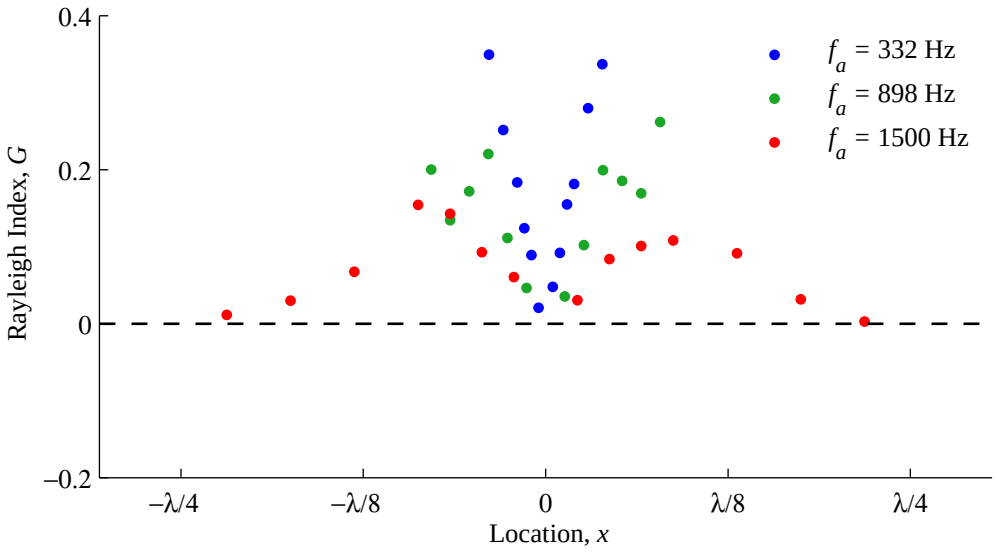


Figure 4.20: Distribution of Rayleigh indices for burning ethanol droplets across various locations $x$ and forcing frequencies $f_a$.

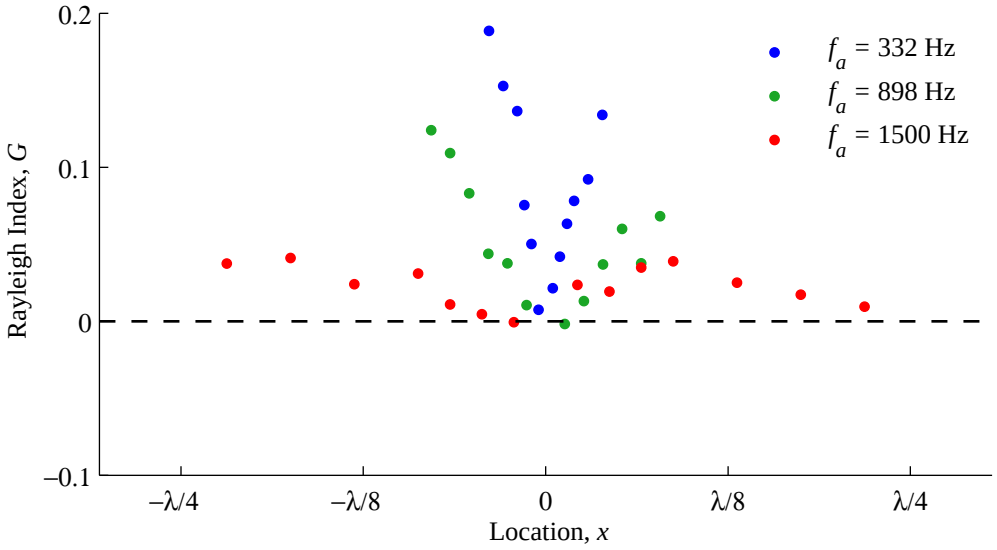


Figure 4.21: Distribution of Rayleigh indices for burning methanol droplets across various locations $x$ and forcing frequencies $f_a$.

# CHAPTER 5

# Conclusions and Recommendations

The outlined liquid fuel droplet experiments permitted the exploration of alternative fuel combustion behaviors in the presence of acoustic excitation. A host of metrics characterizing the nature of the droplet combustion in acoustically resonant environments were employed in this assessment. Mean burning rates associated with a single burning fuel droplet increased by as much as 25% in comparison to their baseline, unforced counterparts. Acoustic accelerations, constituents of the acoustic radiation force model of burning droplets in the vicinities of pressure nodes (PN) and pressure antinodes (PAN) within standing acoustic waves, were estimated theoretically and experimentally through visual measurement of flame deflection angles. The observed orientation of the flames, indicative of the sign in the acoustic acceleration term, was consistent with that predicted by theory. Flame plumes were uniformly deflected away from the central PN region for all forcing configurations and fuels. However, the magnitudes of experimental and theoretical acoustic acceleration were inconsistent in the proximity of the PN. The acoustic radiation force model yielded modest flame deflections whose maxima were coincident with $x = \pm\lambda/8$; experimentally, pronounced acoustic accelerations commonly found to exceed standard gravitation ($g_a > 9.81$ m/s$^2$) were largest immediately next to the PN. Furthermore, the burning droplets situated exactly at the PN exhibited unstable features disallowing experimentation at $x = 0$ cm.

Ultimately inadequacies in the modeling of interactions between dynamic combustion and acoustic perturbations inherent to the acoustic radiation force theory were reconciled through the evaluation of the Rayleigh index. A quantification of the Rayleigh criterion for combustion instability, the Rayleigh index represented the degree of thermoacoustic coupling

of pressure and heat release rate oscillations. These periodic fluctuations, collected via intensified imaging that was phase-locked to the acoustic forcing cycle, were discovered to be in-phase at all waveguide locations near the PN. Computed positive Rayleigh indices underlined the established combustion instability engendered through interaction of acoustic forcing and evolution of chemical kinetics. Conversely, comparatively tenuous thermoacoustic flame response was perceived near the PAN positions. This implied the locally independent frequency response of the combustion dynamics and explicated the agreement in measured and predicted acoustic accelerations near low $u'$ regions. Therefore, a revised model for the burning of liquid droplets in acoustically resonant environments demands the consideration of temporally sensitive flame kinetics to imposed frequencies of forcing in addition to mean, global characteristics.

Future amendments to this study should progress the understanding of mechanisms influencing acoustically coupled combustion reactions while simultaneously refining methodologies harnessed in diagnosing relevant physical parameters. In the context of improving the present apparatus, acoustic and chemiluminescence modeling would enhance the fidelity of recorded observations. The nature of the standing acoustic waves within the waveguide facility was scrutinized extensively prior to implementation of forcing in these experiments. Nevertheless, a more formal approach utilizing elements of acoustic impedance theory could enrich the overall understanding of the distribution and translocation of pressure and velocity distributions. Similarly, the assumption of proportionality between OH* chemiluminescence output and resulting heat release rate could be cemented with analytical calculation and experimental validation. The luminescent decay phenomenon may also be assessed through these calculations by comparing burning configurations with progressively distinct product mole fractions.

The results provided hold implications for the acoustically active burning droplet system that could motivate subsequent explorations. A dynamic stability analysis, for instance, could prove useful in generating a definitive model for combustion within standing waves. Such a formulation might reveal the presence of characteristically volatile features, like saddle

points or unstable equilibria, that may illuminate the inability to sustain a flame near PN locations and the disparity with regard to the acoustic radiation force model. Regarding flame orientation phenomena, the severe deflections of the flame plume imply that imposition of acoustic standing wave can produce acoustic accelerations exceeding standard gravitation. This assertion may be investigated in a vertical configuration to conceivably cancel out the influence of gravity and retain a spherically symmetric flame surrounding the fuel droplet. Vertical waveguide experiments may permit for simulation of combustion in microgravity environments within practical laboratory settings, granting a novel, relatively inexpensive alternative to conduction of such studies in prohibitive conditions inherent to drop towers, low-$g$ flight, or planetary orbit.

# APPENDIX A

# Acoustic Behavior in a Tube Forced by Vibrating Pistons at Both Ends

Prepared by Jeffrey D. Eldredge

University of California - Los Angeles

Department of Mechanical and Aerospace Engineering

Consider a tube (as shown below) in which pistons are situated at either end and vibrate with known harmonic motion, described with velocity $U(t) = U_0 \cos(\omega t)$ and $U(t) = U_0 \cos(\omega t + \phi)$, respectively.

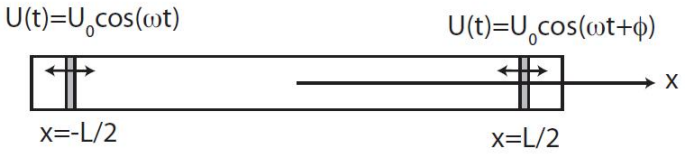


We assume that the frequency $\omega$ is sufficiently low that only plane waves can propagate in the tube. Furthermore, the length of the tube is sufficiently short that dissipative effects in the medium - assumed to be a perfect gas - are negligible. The mean speed of sound is denoted by $c$ and the mean density by $\rho$.

We assume that fluctuating pressure $|p'|$ is sufficiently small compared with the mean pressure to ensure that acoustic waves behave linearly. Thus, we adopt a complex notation, in which the quantities are all harmonic, e.g. fluctuating pressure and velocity are written as

$$p'(x,t) = Re(\hat{p}(x)e^{i\omega t}), \quad u'(x,t) = Re(\hat{u}(x)e^{i\omega t}) \tag{A.1}$$

where Re() denotes the real part of this expression.

The pressure fluctuations in the gas can be described as two traveling plane waves,

$$p'(x,t) = Re[(Ae^{-ikx} + Be^{ikx})e^{i\omega t}]$$

where k = $\omega$/c. The $A$ corresponds to the amplitude of the wave traveling in the +x direction, and $B$ the amplitude for the wave in the -x direction. The acoustic velocity that is consistent with this pressure (i.e. satisfies the linearized mass and momentum equations for the gas) is given by

$$u'(x,t) = \frac{1}{\rho c} Re[(Ae^{-ikx} - Be^{ikx})e^{i\omega t}]$$

The piston velocities can be written in this complex notation as $Re(U_0 e^{i\omega t})$ and $Re(U_0 e^{i\phi} e^{i\omega t})$, respectively. Henceforth, we can dispense with the factor of $e^{i\omega t}$ since it cancels out of every expression. We also consider only the full complex expressions, and remember to take the real part to recover the physical quantity.

The boundary conditions on the waves are provided by the no-flow-through condition at the piston surfaces (strictly speaking, the condition is applied to the positions of fluid particles, but this is equivalent in this case to a condition on their velocities). If we assume that the maximum excursion of the piston from its mean position is small compared to the wavelength (which is equivalent to assuming that $U_0 << c$), then we can apply this boundary condition at the mean position of each piston, viz.,

$$\hat{u}(-L/2) = U_0, \quad \hat{u}(L/2) = U_0 e^{i\phi} \tag{A.2}$$

Thus, we have two equations for the two unknowns $A$ and $B$:

$$Ae^{ikL/2} - Be^{-ikL/2} = \rho c U_0 \tag{A.3}$$

$$Ae^{-ikL/2} - Be^{ikL/2} = \rho c U_0 e^{i\phi} \tag{A.4}$$

From these, one can solve for $A$ and $B$:

$$A = \frac{\rho c U_0}{2i} \frac{e^{ikL/2} - e^{-ikL/2+i\phi}}{\sin kL} \tag{A.5}$$

$$B = \frac{\rho c U_0}{2i} \frac{e^{-ikL/2} - e^{ikL/2+i\phi}}{\sin kL} \tag{A.6}$$

From these, one can write the pressure and velocity amplitudes as

$$\hat{p}(x) = -\frac{i\rho c U_0 e^{i\phi/2}}{\sin kL}[e^{-i\phi/2}\cos(k(x - L/2)) - e^{i\phi/2}\cos(k(x + L/2))] \tag{A.7}$$

$$\hat{u}(x) = -\frac{U_0 e^{i\phi/2}}{\sin kL}[e^{-i\phi/2}\sin(k(x - L/2)) - e^{i\phi/2}\sin(k(x + L/2))] \tag{A.8}$$

respectively. Alternatively, they can be written as

$$\hat{p}(x) = -\frac{\rho c U_0 e^{i\phi/2}}{\sin kL}[e^{-ikL/2}\sin(kx - \phi/2) - e^{ikL/2}\sin(kx + \phi/2)] \tag{A.9}$$

and

$$\hat{u}(x) = -\frac{i U_0 e^{i\phi/2}}{\sin kL}[e^{-ikL/2}\cos(kx - \phi/2) - e^{ikL/2}\cos(kx + \phi/2)] \tag{A.10}$$

The rms magnitude of the pressure fluctuations is given by $p_{rms} = |\hat{p}(x)|/\sqrt{2}$. This results in

$$p_{rms}(x) = \frac{\rho c U_0}{\sqrt{2}|\sin kL|}[\sin^2(kx-\phi/2)+\sin^2(kx+\phi/2)-2\cos(kL)\sin(kx-\phi/2)\sin(kx+\phi/2)]^{1/2} \tag{A.11}$$

or, in somewhat simpler form,

$$p_{rms}(x) = \frac{\rho c U_0}{\sqrt{2}|\sin kL|}[1 - \cos kL\cos\phi + \cos(2kx)(\cos kL - \cos\phi)]^{1/2} \tag{A.12}$$

Consider the special case in which the length of the tube is an integer multiple of the wavelength. Then $kL = 2\pi n$, where n is an integer, and the rms pressure expression reduces to

$$p_{rms}(x) = \frac{\sqrt{2}\rho c U_0}{|\sin kL|}|\sin(\phi/2)||\sin(kx)| \tag{A.13}$$

Thus, there is no way to shift the node from the center of the tube, regardless of the phase $\phi$. (We have left $|\sin kL|$ unevaluated here. Theoretically, it goes to zero, making the rms pressure infinitely large, but in reality the system simply has a large response that is saturated by non-linearities or neglected physical phenomena.) A similar result holds if the length of the tube is a multiple of a half wavelength, whereupon we get

$$p_{rms}(x) = \frac{\sqrt{2}\rho c U_0}{|\sin kL|}|\cos(\phi/2)||\sin(kx)| \tag{A.14}$$

If the length of the tube does not fulfill these special cases, then the interference between the waves will no longer be perfectly destructive, so the pressure at the nodes will be non-zero. Furthermore, the minima in pressure can only occur at either $0, \pm\lambda/2, ...$, or at $\pm\lambda/4, \pm 3\lambda/4, ...$ In the special case that $\phi = kL$ the pressure is actually uniform throughout the tube. However, **it is not possible to use phase difference alone to shift the nodes to any desired location.**

Though it is not possible to shift the node arbitrarily through phase variations, one can consider how the phase effects the pressure at the center of the tube. Here, the expression reduces to

$$p_{rms}(0) = \sqrt{2}\rho c U_0 \frac{|\cos(kL/2)|}{|\sin(kL)|} |\sin(\phi/2)| \tag{A.15}$$

It vanishes when the length of the tube is a multiple of a half wavelength (as confirmed by Eq. (A.14)).

# APPENDIX B

## Waveguide Ends Acoustic Assessment

Prepared by Ann R. Karagozian

University of California - Los Angeles

Department of Mechanical and Aerospace Engineering

**Idealized tube with two closed ends:** Resonant Conditions

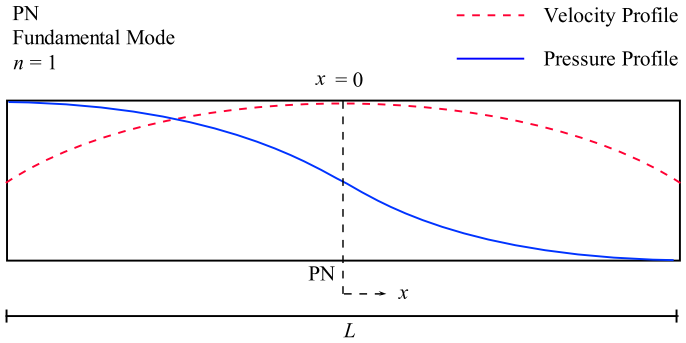


$$\text{Wavelength:} \qquad \lambda = \frac{2L}{n} \tag{B.1}$$

$$\text{or} \quad L = \frac{n}{2}\lambda = \frac{n}{2}\left(\frac{c}{f}\right) \tag{B.2}$$

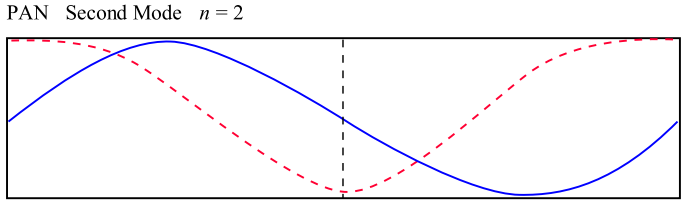


$$\lambda = \frac{2L}{n} = L$$

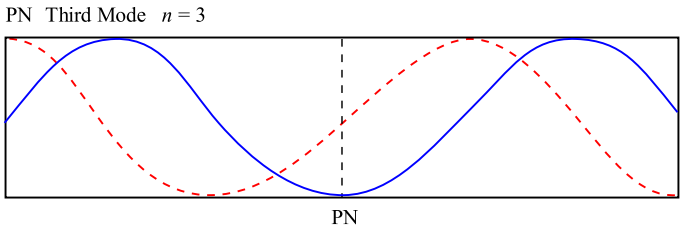


$$\lambda = \frac{2L}{n} = \frac{2}{3}L$$

**Idealized open tube at one end:**

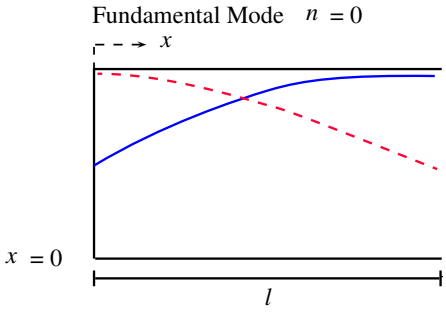


Open end ideally forces $p' = 0$
and $|u'|$ to be maximized

Resonant Condition

$$\lambda = \frac{4l}{2n+1} \tag{B.3}$$

If $n = 0 \rightarrow l = \frac{\lambda}{4}$, one achieves "quarter wave tube" that should attenuate disturbance generated at $x = 0$ by increasing $u'$ at $x = l$

Explanation: If the "closed" end consists of a vibrating membrane at $x$=0, with $u_{memb} = U_0 e^{i\omega t}$, then open-ended tube has velocity

$$u(x,t) = U_0 e^{i\omega t} \frac{\cos(k(l-x))}{\cos(kl)} \tag{B.4}$$

$$\text{with} \quad k = \frac{\omega}{c} = \frac{2\pi f}{c} = \frac{2\pi}{\lambda}$$

So at the open end of the tube,

$$u(l,t) = \frac{U_0}{cos(kl)} e^{i\omega t} = U_l, \text{ velocity at end can be amplified} \tag{B.5}$$

$$\rightarrow \frac{U_l}{U_0} = \frac{1}{cos(\frac{\omega l}{c})} \rightarrow \infty \quad \text{when} \quad \frac{\omega l}{c} = \frac{\pi}{2}(2n+1) \quad \text{or} \quad \lambda = \frac{4l}{2n+1} \text{ (B.3)}, \quad \text{as above.}$$

**Present configuration:**

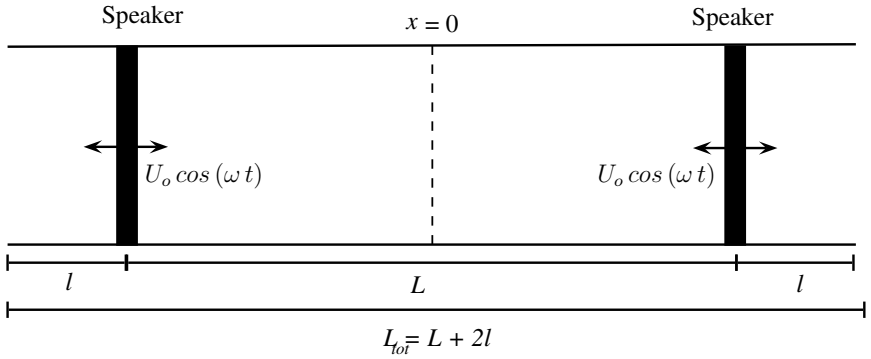


For most experiments, $L \cong 61\text{cm} = 0.61\text{m}$ ; in 2011 our group found:

Waveguide:

| Condition at Center | Speaker Phase Difference | $n$ | Theoretical $f$ | Experimental $f$ |
|---|---|---|---|---|
| PN | 180° | 1 | 281 Hz | 332 Hz |
| PAN | 0° | 2 | 562 Hz | 558 Hz |
| PN | 180° | 3 | 843 Hz | 898 Hz |
| PAN | 0° | 4 | 1125 Hz | 1132 Hz |
| PN | 180° | 5 | 1406 Hz | 1500 Hz |

where $f = \frac{nc}{2L}$ and $c \cong 343\, m/s$ speed of sound

Ends:

If $L_{total} \cong 1$ m, then $l \cong 0.2$ m approximately on each side; with the above forcing frequencies acting at the speakers, the "quarter wave" tube length $l$ would be, for the PN conditions,

| $f_{theoretical}$ | $\lambda = \frac{c}{f}$ | $l_{th,\ quart}$ | $f_{experimental}$ | $\lambda = \frac{c}{f}$ | $l_{exp,\ quart}$ |
|---|---|---|---|---|---|
| 281 Hz | 1.22 m | 0.3 m | 332 Hz | 1.03 m | 0.26 m |
| 843 Hz | 0.41 m | 0.1 m | 898 Hz | 0.38 m | 0.096 m |
| 1406 Hz | 0.24 m | 0.06 m | 1500 Hz | 0.22 m | 0.057 m |

Resonant: $\lambda = \frac{4l}{2n+1}$ ($n$=0 is quarter wave condition) or $n = \frac{1}{2}[\frac{4l}{\lambda} - 1]$

Hence, $f = 332$ Hz and (to a lesser extent) $f = 898$ Hz have $l_{quart}$ values that are probably achieved when the speakers are moved as presently done ($\Delta x = \pm 0.1m$), where $\Delta x$ translates to changes in $l$.

It would be better, possibly, to alter the actual $l$ for $f = 332$ Hz and $f = 898$ Hz to avoid hitting a resonant condition. Lengths for $l$ to avoid (for each end) are:

$$l = \frac{\lambda}{4}(2n+1) = \frac{c}{4f}(2n+1)$$

| 332 Hz | | 898 Hz | | 1500Hz | |
|---|---|---|---|---|---|
| $n$ | $l$ | $n$ | $l$ | $n$ | $l$ |
| 0 | 0.26 m | 0 | 0.096 m | 0 | 0.057 m |
| 1 | 0.77 m | 1 | 0.29 m | 1 | 0.17 m |
| 2 | - | 2 | 0.48 m | 2 | 0.28 m |

It's likely that the data at $n = 0$ for 332 Hz and $n = 1$ for 898 Hz are creating problems with respect to attenuation of energy in the waveguide.

Thus, our observations could possibly be explained as follows:

A) Moving both speakers to right or left by $\pm\Delta x$, preserving $L$ but making $l_1 \neq l_2$, does not move the PN precisely by $\pm\Delta x$ and reduces $|p'_{max}|$. This could be due to unequal attenuation of acoustic energy when $l_1 \neq l_2$

B) Extensions on ends allow PN to be moved appropriately. This could result from making $l_1 \cong l_2$ and each $\neq l_{quarter}$

**Check with most recent results (12/14/2012):**

For 898 Hz and speaker movement $\Delta x$ to right, with extensions on either side of tube:

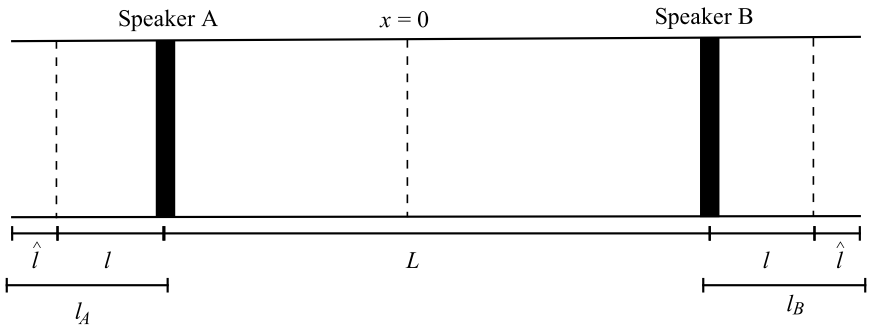


When speakers are each moved $\Delta x$ to right, then the length of open tube to the right of speaker $B$ is $l_B = l + \hat{l} - \Delta x$, and the length of tube to the left of speaker $A$ is $l_A = l + \hat{l} + \Delta x$, affecting proximity to quarter-wave condition (or multiple thereof) that would increase attenuation. Assume $L = 0.61m$, $l = 0.2m$

| $\hat{l}$ | $\Delta x$ | $l_A$ | $l_B$ | $l_{quarter}$ ($n$=1) |
|---|---|---|---|---|
| 0.1 | 0.05 | 0.35 | 0.25 | 0.29 |
| 0.15 | 0.05 | 0.4 | 0.3 | 0.29 |
| 0.1 | 0.03 | 0.33 | 0.27 | 0.29 |
| 0.15 | 0.03 | 0.38 | 0.32 | 0.29 |

We observe lesser attenuation of $p'_{max}$ for $\hat{l}$ of 0.1 m and 0.15 m; this could be because $l_A$ and $l_B$ are generally above $n = 1$ resonant length. For 1500 Hz, $l_A, l_B$ generally well above resonant condition for $n = 0$, 1, so we don't see much attenuation of $p'_{max}$, as expected.

# Bibliography


[1] T. C. Lieuwen and V. Yang. *Progress in Astronautics and Aeronautics: Combustion Instabilities in Gas Turbine Engines: Operational Experience, Fundamental Mechanisms, and Modeling*. AIAA, 2006.

[2] Lord Rayleigh. *The Theory of Sound*. Dover, 1945.

[3] S.M. Candel. Combustion instabilities coupled by pressure waves and their active control. *Twenty-Fourth Symposium (International) on Combustion*, 1992.

[4] T.J. Poinsot, A.C. Trouve, D.P. Veynante, S.M. Candel, and E.J. Esposito. Vortex-driven acoustically coupled combustion instabilities. *Journal of Fluid Mechanics*, 177, 1987.

[5] F. E. C. Culick. Unsteady motions in combustion chambers for propulsion systems. 2006. AGARDograph, NATO/RDO-AG-AVT-039.

[6] V. Yang and W. Anderson. *Liquid Rocket Engine Combustion*. AIAA, 1995.

[7] F. E. C. Culick. Combustion instabilities in liquid-fuelled propulsion systems. Number 450, 1988. AGARD, NATO.

[8] K. Schadow and V. Yang. Active combustion control for propulsion systems. 1996. AGARD, NATO.

[9] J.M. Cohen and T.J. Anderson. Experimental investigation of near blow-out instabilities in a lean, premixed step combustor. Number 96-0819, 1996.

[10] A.P. Dowling and A.S. Morgans. Feedback control of combustion oscillations. *Annual Review of Fluid Mechanics*, 37, 2005.

[11] Y. Huang and V. Yang. Dynamics and stability of lean-premixed swirl-stabilized combustion. *Progress in Energy and Combustion Science*, 35, 2009.

[12] C.H. Sohn and S.H. Chung. Structure and acoustic-pressure response of hydrogen-oxygen diffusion flames at high pressure. *Combustion and Flame*, 115, 1998.

[13] K.H. Yu. Active combustion control using multiple vortex shedding. *AIAA*, (96-2760), 1996.

[14] A. R. Karagozian, W. J. A. Dahm, E. Glasgow, R. Howe, I. Kroo, R. Murray, and H. Shyu. Technology options for improved air vehicle fuel efficiency. 2006. Air Force Scientific Advisory Board Report, Technical Report SAB-TR-06-04.

[15] D. Gray and H. Schobert. Production of alternative liquid hydrocarbon transportation fuels from natural gas, coal, and coal and biomass. 2012. Working Document of the NPC Future Transportation Fuels Study.

[16] W.E. Tyner. The US ethanol and biofuels boom: Its origins, current status, and future prospects. *BioScience*, 58, 2008.

[17] G. A. Mills and E. E. Ecklund. Alcohols as components of transportation fuels. *Annual Review of Energy*, 12, 1987.

[18] R. Bechtold. *Alternative Fuels Guidebook*. SAE, 1997.

[19] D. Daggett, O. Hallader, R. Hendricks, and R. Walther. Alternative fuels and their potential impact on aviation. Technical report, NASA, 2006. NASA/TM 2006-214326.

[20] F. Fischer. *The Conversion of Coal*. Ernst Benn, Ltd., 1925.

[21] SrA Jason Hernandez. SECAF certifies synthetic fuel blends for B-52H. *Edwards Air Force Base, CA*, 2007. Edwards Air Force Base, CA. http://www.safie.hq.af.mil/news/story.asp?id=123064095.

[22] P. M. Morse, R. H. Boden, and H. Schecter. Acoustic vibrations and internal combustion engine performance, i. standing waves in the intake pipe system. *Applied Physics*, 9, 1938.

[23] A. Williams. Combustion of droplets of liquid fuels - a review. *Combustion and Flame*, 21, 1973.

[24] G.A.E. Godsave. Burning of fuel droplets. Combustion and Flame, 1953. Baltimore, MD. Williams and Wilkins.

[25] C. K. Law. Recent advances in droplet vaporization and combustion. *Progress in Energy and Combustion Science*, 8(3), 1982.

[26] S. R. Turns. *An Introduction to Combustion*. McGraw Hill, 2000.

[27] C. K. Law and G. M. Faeth. Opportunities and challenges of combustion in microgravity. *Progress in Energy and Combustion Science*, 20, 1994.

[28] J. Blaszczyk. Acoustically disturbed fuel droplet combustion. *Fuel*, 70(3), 1973.

[29] S. Kumagai and H. Isoda. Combustion of fuel droplets in a vibrating air field. Fifth Symposium (International) on Combustion, 1955.

[30] P. M. Struk, M. Ackerman, V. Nayagam, and D.L. Dietrich. On calculating burning rates during fibre supported droplet combustion. *Microgravity Science and Technology*, 11, 1998.

[31] H.N. Najm, P.H. Paul, C.J. Mueller, and P.S. Wyckoff. On the adequacy of certain experimental observables as measurements of flame burning rate. *Combustion and Flame*, 113, 1998.

[32] S. Montenegro, B. Stelzner, R. Pirone, D. Fino, and D. Trimis. Experimental determination of heat release in an inverse diffusion flame using laser induced fluorescence spectroscopy. 2012.

[33] A.G. Gaydon. *The Spectroscopy of Flames*. Wiley and Sons, 1957.

[34] A.J. Marchese, R.O. Colantino, F.L. Dryer, and V. Nayagam. Hydroxyl radical chemiluminescence imaging and the structure of microgravity droplet flames. Twenty-Sixth Symposium (International) on Combustion, 1996.

[35] A.J. Marchese, R.O. Colantino, F.L. Dryer, and V. Nayagam. Microgravity combustion of methanol and methanol/water droplets: Drop tower experiments and model predictions. Twenty-Sixth Symposium (International) on Combustion, 1996.

[36] S. Dattarajan, A. Lutomirski, R. Lobbia, O.I. Smith, and A.R. Karagozian. Acoustic excitation of droplet combustion in microgravity and normal gravity. *Combustion and Flame*, 144, 2006.

[37] J.L. Wegener. *Multi-phase Combustion Under the Influence of Acoustic Excitation*, 2011. University of California, Los Angeles. Department of Mechanical and Aerospace Engineering. Doctorate Candidacy Prospectus.

[38] M. Saito, M. Sato, and I. Suzuki. Evaporation and combustion of a single fuel droplet in acoustic fields. *Fuel*, 73, 1994.

[39] M. Saito, M. Sato, and M. Hoshikawa. Enhacement of evaporation/combustion coefficient of a single fuel droplet by acoustic oscillation. *Fuel*, 75, 1996.

[40] K. Okai, O. Moriue, M. Araki, M. Tsue, M. Kono, J. Sato, and D. L. Dietrich. Combustion of single droplet and droplet pairs in a vibrating field under microgravity. *Proceedings of the Combustion Institute*, 28, 2000.

[41] M. Tanabe, T. Morita, K. Aoki, K. Satoh, T. Fujimori, and J. Sato. Influence of standing sound waves on droplet combustion. *Proceedings of the Combustion Institute*, 28, 2000.

[42] M. Tanabe, T. Kuwahara, S. Kimiyoshi, T. Fujimori, J. Sato, and M. Kono. Droplet combustion in standing sound waves. *Proceedings of the Combustion Institute*, 30, 2005.

[43] M. Tanabe. Drop tower experiments and numerical modeling on the combustion-induced secondary flow in standing acoustic fields. *Microgravity Science Technology*, 22, 2010.

[44] S. Dattarajan. *Acoustically Excited Droplet Combustion in Normal Gravity and Microgravity*. PhD thesis, University of California, Los Angeles, Department of Mechanical and Aerospace Engineering, 2004.

[45] J.I. Rodriguez. *Acoustic Excitation of Liquid Fuel Droplets and Coaxial Jets*. PhD thesis, University of California, Los Angeles, Department of Mechanical and Aerospace Engineering, 2009.

[46] J.I. Rodriguez, S. Teshome, H.S. Mao, A. A. Pezeshkian, O.I. Smith, and A.R. Karagozian. Acoustically driven droplet combustion with alternative liquid fuels. *46th AIAA Aerospace Sciences Meeting and Exhibit*, 2008.

[47] S. Thesome. *Droplet Combustion and Non-Reactive Shear-Coaxial Jets with Traverse Acoustic Excitation*. PhD thesis, University of California, Los Angeles, Department of Mechanical and Aerospace Engineering, 2012.

[48] S. Teshome, A. Pezeshkian, O.I. Smith, and A.R. Karagozian. Influence of standing acoustic waves on combustion of alternative fuels. *Proceedings of the American Physical Society*, 2008.

[49] S. Teshome, O.I. Smith, and A.R. Karagozian. Droplet combustion in the presence of altered acceleration fields via acoustic excitation. *Western States Sections of the Combustion Institute*, 2009.

[50] J. Eldredge. Private communications. *UCLA*, 2009.

[51] M. De Leo, A. Saveliev, L.A. Kennedy, and S.A. Zelepouga. OH* and CH* luminescence in opposed flow methane oxy-flames. *Combustion and Flame*, 149(4), 2007.

[52] J. Ballester and T. Garcia-Armingol. Diagnostic techniques for the monitoring and control of practical flames. *Progress in Energy and Combustion Science*, 36(4), 2010.

[53] J. Diederichsen and R.D. Gould. Combustion instability: Radiation from premixed flames of variable burning velocity. *Combustion and Flame*, 9(1), 1965.

[54] A. Hultqvist, M. Christensen, B. Johansson, A. Franke, M. Richter, and M. Alden. A study of the homogeneous charge compression ignition combustion process by chemiluminescence imaging. *SAE Journal of Engines*, 18(3).

[55] C.J. Lawn. Distributions of instantaneous heat release by the cross-correlation of chemiluminescent emissions. *Combustion and Flame*, 123(1), 2000.

[56] L.C. Haber, U. Vandsburger, W.R. Saunders, and V.K. Khanna. An experimental examination of the relationship between chemiluminescent light emissions and heat-release rate under non-adiabatic conditions. Technical report, DTIC Document, 2001.

[57] B.H. Timmerman and P.J. Bryanston-Cross. Optical investigation of heat release and nox production in combustion. volume 85, 2007.

[58] M Sliphorst, B Knapp, S Groening, and M Oschwald. Combustion instability-coupling mechanisms between liquid oxygen/methane spray flames and acoustics. *Journal of Propulsion and Power*, 28(6), 2012.

[59] P. Gopalakrishnan, M.K. Bobba, and J.M. Seitzman. Controlling mechanisms for low nox emissions in a non-premixed stagnation point reverse flow combustor. *Proceedings of the Combustion Institute*, 31(2), 2007.

[60] J. Kojima, Y. Ikeda, and T. Nakajima. Spatially resolved measurement of OH*, CH*, and $C_2$* chemiluminescence in the reactio zone of laminar methane/air premixed flames. *Proceedings of the Combustion Institute*, 28, 2000.

[61] LaVision GmbH, Anna-Vandenhoeck-Ring 19, D-37081 Gottingen. *Product-Manual: Nanostar*, October 2011.

[62] National Instruments, 11500 North Mopac Expressway Austin, Texas. *DAQ M Series User Manual*, July 2008.

[63] W.L. Nyborg. Radiation pressure on a small rigid sphere. *The Journal of the Acoustical Society of America*, 16(1), 1967.

[64] A. F. Mills and B. H. Chang. Error analysis of experiments. *UCLA, Los Angeles, CA*, 2004.

[65] C. J. Dasch. One-dimensional tomography: a comparison of Abel, onion-peeling, and filtered backprojection methods. *Journal of Applied Optics*, 31(8), 1992.

[66] P.A. Muzzell, E.R. Sattler, A. Terry, B.J. McKay, J. Brian, R.L. Freerks, L. Robert, and L.L. Stavinoha. Properties of Fischer-Tropsch (FT) blends for use in military equipment. Technical report, DTIC Document, 2006.

[67] J. Schmitigal and J. Tebbe. JP-8 and other military fuels. Technical report, DTIC Document, 2011.

[68] A. Violi, S. Yan, E.G. Eddings, A.F. Sarofim, S. Granata, T. Faravelli, and E. Ranzi. Experimental formulation and kinetic model for JP-8 surrogate mixtures. *Combustion Science and Technology*, 174(11-12), 2002.

[69] T.J. Bruno. Thermodynamic, transport and chemical properties of "reference" JP-8. Technical report, DTIC Document, 2006.

[70] J.S. Chickos and H. Zhao. Measurement of the vaporization enthalpy of complex mixtures by correlation-gas chromatography. the vaporization enthalpy of RP-1, JP-7, and JP-8 rocket and jet fuels at T= 298.15 K. *Energy & Fuels*, 19(5), 2005.

[71] Turbine fuel, aviation, kerosene type, JP-8 (NATO F-34), NATO F-35, and JP-8+100 (NATO F-37). Technical report, United States Department of Defense, 2011.

[72] E.G. Willett. Sound Attenuating Chamber, 1972. US Patent 3,655,011.

[73] A. D. Pierce. *Acoustics: An Introduction to its Physical Principles and Applications*. McGraw Hill, 1981.

[74] A.R. Karagozian. Private communications. *UCLA*, 2013.

[75] F.N. Egolfopoulos and C.S. Campbell. Unsteady counterflowing strained diffusion flames: diffusion-limited frequency response. *Journal of Fluid Mechanics*, 318(1), 1996.

[76] T. Selerland and A.R. Karagozian. Ignition, burning and extinction of a strained fuel strip with complex kinetics. *Combustion Science and Technology*, 131, 1998.

[77] H.C. Kim, A.R. Karagozian, and O.I. Smith. Numerical simulations of acoustically driven burning droplets. In *The Combustion Institute Fall Meeting, Los Angeles, California*, volume 26, 1999.

[78] A.L. Smith and C.C. Graves. Drop burning rates of hydrocarbon and nonhydrocarbon fuels. In *NACA RME 57*. F11, 1957.

[79] B. Vielle, C. Chauveau, X. Chesneau, A. Odeide, and I. Gokalp. High pressure droplet burning experiments in microgravity. *Proceedings of the Combustion Institute*, 26, 1996.